

MANY-BODY PHYSICS USING COLD ATOMS

A Dissertation

Presented to the Faculty of the Graduate School

of Cornell University

in Partial Fulfillment of the Requirements for the Degree of

Doctor of Philosophy

by

Bhuvanesh Sundar

December 2016

© 2016 Bhuvanesh Sundar
ALL RIGHTS RESERVED

MANY-BODY PHYSICS USING COLD ATOMS

Bhuvanesh Sundar, Ph.D.

Cornell University 2016

Advances in experiments on dilute ultracold atomic gases have given us access to highly tunable quantum systems. In particular, there have been substantial improvements in achieving different kinds of interaction between atoms. As a result, ultracold atomic gases offer an ideal platform to simulate many-body phenomena in condensed matter physics, and engineer other novel phenomena that are a result of the exotic interactions produced between atoms.

In this dissertation, I present a series of studies that explore the physics of dilute ultracold atomic gases in different settings. In each setting, I explore a different form of the inter-particle interaction. Motivated by experiments which induce artificial spin-orbit coupling for cold fermions, I explore this system in my first project. In this project, I propose a method to perform universal quantum computation using the excitations of interacting spin-orbit coupled fermions, in which effective p -wave interactions lead to the formation of a topological superfluid. Motivated by experiments which explore the physics of exotic interactions between atoms trapped inside optical cavities, I explore this system in a second project. I calculate the phase diagram of lattice bosons trapped in an optical cavity, where the cavity modes mediate effective global range checkerboard interactions between the atoms. I compare this phase diagram with one that was recently measured experimentally. In two other projects, I explore quantum simulation of condensed matter phenomena due to spin-dependent interactions between particles. I propose a method to produce tunable spin-dependent interactions between atoms, using an

optical Feshbach resonance. In one project, I use these spin-dependent interactions in an ultracold Bose-Fermi system, and propose a method to produce the Kondo model. I propose an experiment to directly observe the Kondo effect in this system. In another project, I propose using lattice bosons with a large hyperfine spin, which have Feshbach-induced spin-dependent interactions, to produce a quantum dimer model. I propose an experiment to detect the ground state in this system. In a final project, I develop tools to simulate the dynamics of fermionic superfluids in which fermions interact via a short-range interaction.

BIOGRAPHICAL SKETCH

Bhuvanesh Sundar grew up in Chennai, India, living there until 2005. He obtained a Bachelors of Technology in Engineering Physics at the Indian Institute of Technology, Delhi, India, in 2010, and a minor degree in Computer Science. He did research on metamaterials and METATOYS during a summer internship at the University of Glasgow in 2008. For his undergraduate thesis, he studied spin-imbalanced Fermi gases, and spin-orbit coupled Fermi gases. He moved to the USA in 2010 to pursue a Masters and a Ph.D in Physics at Cornell University. He obtained his Masters degree in Physics in 2013.

Bhuvanesh Sundar loves to teach, and is an avid puzzle solver. He can be found every afternoon with his officemates, staring at the daily crossword puzzle in the newspaper over lunch. He doesnt stare at the sudoku puzzle for long; instead he usually does it in his head while riding the elevator. In his spare time, Bhuvanesh also climbs cliffs, backpacks, bikes on rugged trails, skis, and plays squash.

ACKNOWLEDGEMENTS

The person who has been most important to the completion of my doctoral dissertation is my advisor, Erich Mueller. Therefore, I would like to thank him first. When I came to Cornell University in 2010 to pursue a doctoral degree in condensed matter physics, I had no clue what condensed matter physics was. When I did learn what condensed matter physics was, I had my doubts about my choice of my field of study. Erich kindly took me under his guidance, and has been a shining example of an ideal mentor. He devoted his valuable time to help me through each step of the way, from installing Python on my laptop, to debugging my long and disorganized Mathematica codes, and advising me on writing strategies on the micro and macro level. He spent countless hours with me to teach me basic concepts in physics, from ten different perspectives I did not know existed. He never once lost patience when I would not understand what he said. He has always paid attention to my ideas in tackling research problems. I suspect he knew the answer to every problem all along, and patiently waited at the end for me to catch up. Time and again, I look back through my notes taken during our first meetings on a project, and realize that Erich already had the solution to my research problem. In my final year, he set aside countless hours to coordinate my (and other students') preparation for the next stage in our careers. And finally, he has been the best teacher I have known. For all that, I cannot thank him enough. I hope I can one day thank him by being a good researcher, and show that I've indeed learned from him.

There are several other people I would like to thank. I would like to thank Prof. Johannes Courtial and the rest of his research group at the University of Glasgow, who showed me that research in physics can be fun, and something I want to do for the rest of my life. This came at a time when I was considering switching to

studying computer science. My most productive research period has been during my work with Johannes.

I owe my thanks to all my friends in my undergraduate institute who motivated me to study physics. These friends are Abha Rajan, Pragun Goyal, Shubham Kumar, Jwalit Patel, Sujeet Shukla, Swati Gupta, Abhiti Tewari, and Ekta Jindal. I owe special thanks to Abha Rajan and Shubham Kumar.

I owe my thanks to all the Professors who have ever taught me so far. Prof. T R Subramanian, who taught me that I like math. Prof. Ananthan and Prof. Ravishankar for teaching me what physics is. Prof. Santhanam and Prof. Govindarajan for their endless energy and passion for teaching. Prof. K Thyagarajan and Prof. D Ranganathan, who inspired me to remain in the physics program during my undergraduate study. The only classes I took were taught by these two Professors. And I would like to thank Prof. Sankalpa Ghosh and Prof. Amruta Misra for introducing me to the field of ultracold atomic gases during my undergraduate study.

I owe Prof. Michael Lawler and Todd Rutkowski a big thank you for teaching me about quantum spin liquids, and patiently waiting for me when they were far ahead in understanding path integral techniques. I thank Todd for the numerous hours he spent driving back and forth between Ithaca and Binghamton to meet me, just because I preferred face-to-face communication.

I enjoyed a stimulating atmosphere of physics in my office and the physics department. I would like to thank all of my group members and officemates, Matthew Reichl, Shovan Dutta, Sayan Choudhury, Nur Unal, Yariv Yanay, Yi Ting Hsu, Kyungmin Lee, Junjun Xu, and Ran Wei for illuminating and insightful discussions. I owe special thanks to Matthew Reichl and Ran Wei for patiently answering all my questions, and often solving my problems for me. I would also

like to thank Zhen Wah Tan and Yi Ting Hsu for helping me through my first year of Ph.D.

Prof. Mukund Vengalattore and his research group taught me a huge amount about real physical systems, and an entirely new perspective to think about them. My mind was blown away when I first visited their labs. And the second time, and the third time as well. I also thank Prof. Vengalattore for carefully scrutinizing my dissertation during the final stages of writing it, and for suggesting several experimentally relevant questions that I had omitted to address in this dissertation.

I owe thanks to all the Professors at Cornell University, whose passion for research and teaching I strive to achieve. I thank Prof. Andre Leclair for giving me freedom in teaching my recitations, and the opportunity to substitute for him in lectures when he traveled. I thank all the students I have ever taught, for all the lessons I learned from teaching them, and for putting up with me when I was clueless about their questions.

Many people are responsible for my good times in Ithaca during my Ph.D. The Cornell Outing Club and all its members have provided me means to de-stress, relax, and reflect by introducing me to the outdoors and several new outdoor sports. Alex Chertok, Shai Davidai, Frederika Loew, Yardenne Greenspan, Todd Dickey, and Amit Kumar took me as their friend. Matthew Reichl and Kyungmin Lee tolerated me poring over the crossword puzzle everyday during lunch. The Millers' was a second home in Ithaca for me; Deborah and Jay Miller always give me a warm welcome whenever I visit.

Finally, I would like to thank everyone in the physics department at Cornell University, for giving me the opportunity to come to a far away land to study a subject as immensely exciting as ultracold atoms. I would like to thank them for taking care of numerous administrative details so that I can focus only on

my research, so that my graduate study would be smooth. And for giving me numerous teaching opportunities, which I immensely love! And I would like to say this about all the people of Ithaca - they are awesome!

TABLE OF CONTENTS

Biographical Sketch	iii
Acknowledgements	iv
Table of Contents	viii
List of Tables	xi
List of Figures	xii
1 INTRODUCTION	1
2 Universal Quantum Computation With Majorana Fermion Edge Modes Through Microwave Spectroscopy Of Quasi-1D Cold Gases In Optical Lattices	7
2.1 Experimental setup	10
2.1.1 Coupled Wires	11
2.1.2 Proximity-Induced Superfluid	12
2.1.3 Trap and Probe	13
2.2 Theoretical model	14
2.2.1 Coupled Wires	14
2.2.2 Proximity-Induced Superfluid	16
2.2.3 Other Considerations	17
2.3 Bogoliubov excitations	17
2.4 Majorana modes	20
2.5 Absorption spectrum	22
2.5.1 Periodic Boundary Conditions	24
2.5.2 Infinite Square Well	26
2.5.3 Harmonic Traps	27
2.6 Dynamics	28
2.7 Numerical Methods	29
2.8 Quantum Gates	30
2.8.1 Intermediate Regime: Projective Initialization	30
2.8.2 Fast and Slow Regimes: Coherent Gate Operations	34
2.8.3 Z Gate	39
2.9 Two Logical Qubits Composed Of Three Physical Qubits	39
2.9.1 Construction of Logical Qubits	40
2.9.2 Measurement and Initialization	41
2.9.3 Coherent Single Qubit Operations	42
2.9.4 Two-Qubit Operations	43
2.10 Summary	46
3 Lattice bosons with infinite range interactions	48
3.1 Introduction	49
3.2 Homogeneous gas	50
3.2.1 Model	50

3.2.2	Gutzwiller ansatz	52
3.2.3	Phase diagram	53
3.3	Inhomogeneous gas	57
3.3.1	J=0	58
3.3.2	Phase diagram	60
3.3.3	Comparison to experiment	61
3.4	Summary	62
4	Proposal to directly observe the Kondo effect through enhanced photoinduced scattering of cold fermionic and bosonic atoms	65
4.1	Model	68
4.2	An experimental setup	71
4.3	Kondo-enhanced scattering between ^{87}Rb and ^6Li	75
4.3.1	Alternative methods to measure enhanced Kondo scattering	78
4.4	Experimental considerations for an optical Feshbach resonance . . .	79
4.5	Summary	82
5	Engineering quantum dimer models via large-spin Mott-insulating ultracold bosons	86
6	Semiclassical tools to study the dynamics of a Fermi gas during a time-of-flight expansion	99
6.1	Introduction	100
6.2	Formalism	101
6.3	Homogeneous gas	105
6.3.1	Weakly interacting limit	105
6.3.2	Strongly interacting limit	106
6.4	Gross Pitaevskii equation	107
6.5	Example: Time-of-flight expansion	108
6.6	Conclusions	112
7	Conclusions	114
A	Majorana fermions	123
A.1	Superfluid gap from nearest-neighbor interactions	123
A.1.1	Dipolar molecules	123
A.1.2	Artificial spin-orbit coupling	124
A.1.3	Spin-dependent lattices	125
A.2	Edge modes	126
B	Atomic interactions mediated by an ideal confocal cavity	128

C	The Kondo effect: Momentum exchanged in a scattering experiment	132
C.1	Calculation of the momentum transferred	132
C.1.1	Feynman rules	132
C.1.2	Calculation of $n_{k\alpha m}(t)$	134
C.1.3	Final momentum of the Fermi gas	140
D	Deriving a quantum dimer model for Mott insulating bosonic atoms with a large hyperfine spin	142
D.1	Construction of an orthogonal basis	142
D.2	Deriving an effective dimer model	143

LIST OF TABLES

5.1	List of ring exchange amplitudes and bond interactions obtained from Eq. (5.3), in different lattice geometries.	93
-----	--	----

LIST OF FIGURES

2.1	Local single-particle density of states for the mean-field model in Eq. (2.10) with parameters $\Delta_j = \mu = 0.25J, N = 50$. The local density of states is a sum of Dirac δ functions. Darker shades represent higher amplitudes of the Dirac δ functions. We can observe bulk quasiparticles with $E_\nu > 0$ and zero-energy ($E_\nu = 0$) excitations at the edges. These zero-energy modes are Majorana modes.	19
2.2	The electromagnetic absorption spectrum when atoms are excited from the “a” state to the “c” state with periodic boundary conditions. The solid curve is the absorption spectrum of $ g_+\rangle$ and the dashed curve of $ g_-\rangle$. Parameters chosen in (a) are $\Delta_j = J, \mu = 0, N = 30$, and in (b) are $\Delta_j = J/2, \mu = J/4, N = 30$. The parameters used in (b) are not a self-consistent solution of the mean-field approximation [Eq. (2.19)]. If instead we find Δ_j self-consistently, the spectra do not change significantly.	25
2.3	The electromagnetic absorption spectrum when atoms are excited from the “a” state to the “c” state with open boundary conditions. (a) The atoms are trapped in a lattice with 10 sites and hard walls at its ends. (b) The atoms are trapped in a harmonic trap so that the distance between the Majorana modes is 10 sites. In (b), μ_c refers to the chemical potential of the “c” atoms at the center of the trap. The solid curve is the absorption spectrum of $ g_+\rangle$, and the dashed curve of $ g_-\rangle$. Insets show the confining potential minus the optical lattice.	26
2.4	Dynamics of $\langle \hat{\gamma}_{\text{edge}}^\dagger \hat{\gamma}_{\text{edge}} \rangle$ during the initialization gate in a geometry where the system consists of a single wire immersed in a superfluid cloud. The wire is in the form of a ring, as explained in Sec. 2.5.1. Electromagnetic waves are shined upon the system, with frequencies (a) $\omega = -\mu_c - 2J_c$ and (b) $\omega = -\mu_c + 2J_c$. The solid curve corresponds to the system’s initial state being $ \psi\rangle = g_+\rangle$, and the dashed curve to $ \psi\rangle = g_-\rangle$. The fidelities of the initialization gate in the two cases are nearly 100%.	31

2.5	<p>Dynamics of $\langle \hat{\gamma}_{\text{edge}} \hat{\gamma}_{\text{edge}}^\dagger \rangle$ during the initialization gate in a geometry of coupled wires or rings. (a) The atoms are trapped in an array of linear wires. Parameters: $\Delta_j = J = 40\Omega$, $J_c = 5\Omega$, $N = 25$, $\omega_0 = -\mu_c$. (b) The atoms are trapped in an array of rings. Parameters: $\Delta_j = J = 20\Omega$, $J_c = 7.5\Omega$, $N = 50$, $\omega_0 = -\mu_c - 2J_c$. Insets show the geometry of trapping. The solid line represents the case where the system is initially in the state $g_+\rangle$, and the dashed line represents where it is initially in $g_-\rangle$. A frequency ω_0 where $\Gamma(g_-\rangle, \omega_0) = 0$ is shined upon the system, with the intention of setting the qubit to $g_-\rangle$. The square of the fidelity of the final state is roughly 50% in (a) and 90% in (b). In both cases, there is some absorption when the initial state is $g_-\rangle$ due to finite bandwidth of the “c” atoms. In both cases, this shifts ω to a new frequency where $g_-\rangle$ is not dark. In case (a) the absorption at this new frequency is significant, while in case (b) the absorption is still small.</p>	32
2.6	<p>Fidelity of the initialization gate for different lengths of superfluid rings. The “a” and “c” atoms are confined in a ring geometry. We used parameters: $\Delta_j = J = 20\Omega$, $J_c = 7.5\Omega$, and $\omega_0 = \mu_c \pm 2J_c$ for desired final states $\phi\rangle = g_\pm\rangle$. $\psi_f\rangle$ denotes the actual final state produced. The initialization gate has higher fidelity for larger lengths N.</p>	33
2.7	<p>Dynamics of $\langle \hat{\gamma}_{\text{edge}}^\dagger \hat{\gamma}_{\text{edge}} \rangle$ and $\langle \hat{\gamma}_{\text{edge}} \rangle$ during the X and Y gates. The parameters used are $\Delta = J = 80\Omega$, $\mu = 0$, $J_c = 0$, $\omega = -\mu_c$, and the system is initialized to $\frac{1}{\sqrt{2}}(g_+\rangle + g_-\rangle)$. Panels (a) and (b) illustrate the dynamics in the case of an X gate operation and show that the final state is $\frac{1}{\sqrt{2}}(g_+\rangle + g_-\rangle)$. Panels (c) and (d) illustrate the dynamics in the case of a Y gate operation and show that the final state is $\frac{i}{\sqrt{2}}(g_+\rangle - g_-\rangle)$.</p>	38
2.8	<p>Absorption spectrum of physical qubit p_1 trapped in a linear geometry, where barriers create three physical qubits from one wire. Parameters used: $\Delta_j = J$, $\mu = 0$, $N = 7$. The solid curve corresponds to the spectrum of $g_+\rangle$, and the dashed curve to the spectrum of $g_-\rangle$.</p>	41
3.1	<p>Schematic of the experimental setup. A trapped cloud of bosonic ^{87}Rb atoms sits in an off-resonant optical cavity. The atoms are pumped from the side, and scatter light into the cavity. A second laser enters the cavity along its axis, producing an optical lattice.</p>	51

3.2	Phase diagram of a homogeneous Bose gas in the absence of tunneling between lattice sites. The label MI_n denotes a Mott insulating phase with n atoms on each lattice site, and CDW_{nm} denotes a charge-density wave phase with n and m atoms on even and odd sites, or vice versa. The parameters U and U' are the strengths of the short- and long-range interactions, while μ is the chemical potential.	54
3.3	Phase diagram of a homogeneous Bose gas for four different values of the long-range interaction strength U' . SS denotes super-solid, and SF denotes superfluid. Dashed lines indicate second-order phase transitions, and solid lines indicate first order. The parameter J is the tunneling strength between lattice sites.	55
3.4	(a) A $n = 1$ Mott insulating core of radius r_A , surrounded by a CDW_{10} ring from radius r_A to r_B . (b) Scaled energy E_{var} as a function of scaled radius r_A for two cases: $V = 0$ (solid) and $V = \frac{Nm\omega^2 a^2}{2\pi}$ (dotted).	58
3.5	Comparison of LDA and full theory. Vertical axis shows the particle imbalance I between even and odd sites. Horizontal axis shows the strength of the long-range interaction. LDA (dashed line) shows a continuous growth of the imbalance, while the full theory (solid line) shows a discontinuity.	59
3.6	Phase diagram for an inhomogeneous Bose gas in a harmonic trap and an optical lattice, plotted against (a) model parameters, and (b) experimentally relevant parameters. Region I denotes MI_1 -SF phase, II is CDW_{10} -SS, III is SS- CDW_{10} -SS, and IV is CDW_{20} -SS- CDW_{10} -SS. Thick lines denote phase boundaries measured in experiments [86]. The chemical potential is chosen to be $\mu = 0.5U$, and the trap frequency is such that $m\omega^2 a^2 = 0.01U$. In (b), V_0 is the lattice depth, and Δ_c is the detuning of the pump laser from the fundamental cavity mode. The Rabi frequency is chosen to be $\eta = \sqrt{\frac{2\pi}{N} \frac{E_R}{\hbar}}$, the scattering length is $100 a_0$, and the lattice constant and lattice depth in the z direction are 670 nm and $25E_R$, as consistent with experiments [86].	64

4.1	Temperature dependence of the momentum \vec{P} transferred from bosons to fermions in a scattering experiment with photoinduced interactions. Both \vec{P} and temperature have been rescaled to dimensionless quantities. P_0 denotes the momentum transferred to the Fermi gas at zero temperature when the interactions are spin independent ($g_s = 0$). (Solid line) Spin-dependent interactions between spin-1/2 fermions and spin-1 bosons with $g_s = \frac{-1}{3}g_n = \frac{0.1\epsilon_F}{N/v}$; (Dashed line) Spin-independent interactions ($g_s = 0$ and $g_n = -3 \times \frac{0.1\epsilon_F}{N/v}$). The minimum in \vec{P} is a signature of the Kondo effect, and may be detected experimentally. In Sec. 4.4 we estimate experimental parameters to achieve the interaction strength used here. Inset shows a cartoon of the collision.	69
4.2	(Color online) Setup to produce an optical Feshbach resonance between ${}^6\text{Li}$ and ${}^{87}\text{Rb}$ atoms. We couple ${}^6\text{Li}$ and ${}^{87}\text{Rb}$ atoms in their ground states to a ${}^6\text{Li}{}^{87}\text{Rb}$ molecule with angular momenta $L = 1, S = 0$ by shining a laser whose detuning Δ from the molecule is such that $\hbar\Gamma, \Delta E_{\text{hf}} < \hbar\Delta \ll \Delta E_{\text{fs}}$. Here, Γ is the molecular linewidth, and ΔE_{hf} and ΔE_{fs} are the hyperfine and fine structure splitting in the molecule. Typical values of Γ , ΔE_{hf} , and ΔE_{fs} for molecules are provided in the figure (for example, see [38]). In this limit, we obtain an effective Kondo-type spin-dependent interaction between ${}^6\text{Li}$ and ${}^{87}\text{Rb}$ atoms.	72
4.3	(Color online) A density plot of (a) $\frac{ Re(g) n_f\delta t}{\hbar}$ and (b) $\Gamma_{\text{coll}}\delta t$ as a function of laser intensity and detuning. Here $Re(g)$ is the coherent spin-dependent interaction strength, Γ_{coll} is the collision rate between fermions and bosons, and δt is the allowed experimental duration before the gas significantly heats up. The black lines mark the boundary where $ Re(g) n_f\delta t$ and $\Gamma_{\text{coll}}\delta t$ are larger than 1.	85
5.1	(Color online) Examples of singlet cover states. The numbers label the lattice sites, while connected sites represent a spin singlet between the atoms on those sites. In this example, $ a\rangle = \hat{A}_{1,2}^\dagger \hat{A}_{4,5}^\dagger \hat{A}_{3,6}^\dagger 0\rangle$. The notation $ (i, j) : a\rangle$ denotes a state where sites i and j are paired in a singlet, the original partners of i and j in $ a\rangle$ are paired in another singlet, and all the other bonds in $ a\rangle$ are left unchanged. This notation is used in Appendix D to derive an effective dimer model [Eq. (5.6)].	91
5.2	Dimer-dimer correlations on a square lattice with periodic boundary conditions, for (a) $f = 100$ and (b) $f = 3$. The reference dimer is marked grey in the lower left corner. The thickness of the lines is proportional to the strength of correlation. (Color online)	96
5.3	Dimer-dimer correlations on a triangular lattice for (a) $f = 100$ and (b) $f = 3$. The reference dimer is marked in grey. The thickness of the lines is proportional to the strength of correlation.	97

- 6.1 Dynamics of a strongly interacting Fermi gas during a time-of-flight expansion in the x direction. The gas is initialized in a weak harmonic trap of frequency ω in the x direction, and tight traps in the y and z directions. During the expansion, only the trap in the x direction is switched off. (a,b) Density and order parameter of the Fermi gas versus x at $y = z = 0$, computed by numerically integrating the equations of motion for W_σ and F [Eq. (6.14)]. The density is normalized by the density at the centre of the trap at $t = 0$. (c) Order parameter computed by numerically integrating the Gross Pitaevskii equation [Eq. (6.26)]. In the figures, $x_0 = \sqrt{\hbar/m\omega}$ is the harmonic oscillator length. The blue, pink, and yellow curves correspond to $t = 0, 10\hbar/\mu$, and $20\hbar/\mu$, where the expansion began at $t = 0$. For typical trap frequencies $\omega \sim 30$ Hz, and system sizes ~ 1 mm for ultracold gases, $20\hbar/\mu$ corresponds to about 12 ms of expansion. 109
- 6.2 Dynamics of a strongly interacting Fermi gas during a time-of-flight expansion in the x direction. The gas is initialized in a weak harmonic trap of frequency ω in the x direction, and tight traps in the y and z directions. The gas is also initialized to have a soliton. During the expansion, only the trap in the x direction is switched off. (a,b) Density and order parameter of the Fermi gas versus x at $y = z = 0$, computed by numerically integrating the equations of motion for W_σ and F [Eq. (6.14)]. The density is normalized by the maximum density in the trap at $t = 0$. (c) Order parameter computed by numerically integrating the Gross Pitaevskii equation [Eq. (6.26)]. In the figures, $x_0 = \sqrt{\hbar/m\omega}$ is the harmonic oscillator length. The blue, pink, and yellow curves correspond to $t = 0, 10\hbar/\mu$, and $20\hbar/\mu$, where the expansion began at $t = 0$. For typical trap frequencies $\omega \sim 30$ Hz, and system sizes ~ 1 mm for ultracold gases, $20\hbar/\mu$ corresponds to about 12 ms of expansion. 110

6.3	Dynamics of a weakly interacting Fermi gas during a time-of-flight expansion in the x direction. The gas is initialized in a weak harmonic trap of frequency ω in the x direction, and tight traps in the y and z directions. During the expansion, only the trap in the x direction is switched off. (a,b): Density and order parameter of the Fermi gas versus x at $y = z = 0$, computed by numerically integrating the equations of motion for W_σ and F [Eq. (6.14)]. (c,d): Density and order parameter of the Fermi gas versus x at $y = z = 0$, computed by numerically integrating the time-dependent Bogoliubov-de-Gennes equations [Eq. (6.6)]. The density in (a) and (c) is normalized by the density at the centre of the trap at $t = 0$. The blue and pink curves correspond to $t = 0$ and $5\hbar/\mu$, where the expansion began at $t = 0$. At $t = 5\hbar/\mu$, the numerical integration in (a) and (b) develops errors due to the truncation of Eq. (6.14) at second derivatives. For typical trap frequencies $\omega \sim 30$ Hz, and system sizes ~ 1 mm for ultracold gases, $5\hbar/\mu$ corresponds to about 3 ms of expansion.	111
A.1	(Color online) Schematic of a deep spin-dependent lattice and a transverse magnetic field.	125
C.1	In our integrals, time begins at 0, passes through t , then returns to 0. Our perturbation theory requires ordering operators along this path.	133
C.2	Diagrammatic representation of vertex and propagators. (a) Solid line denotes a fermion propagator which propagates a fermion with momentum k and spin projection α from time t_2 to t_1 . (b) Dashed line denotes a boson propagator which propagates a boson with momentum k and spin projection μ from time t_2 to t_1 . (c) A vertex denotes the matrix element for a Bose-Fermi scattering event. Mathematical expressions are given in Eqs.(C.3) and (C.4).	134
C.3	Zeroth-order diagram in the expansion for $n_{k\alpha m}(t)$	135
C.4	First order diagrams in the expansion of $n_{k\alpha m}(t)$	136
C.5	Two of the diagrams that are zero at second order.	136
C.6	Nonzero diagrams at $O(g^2)$ in the expansion for $n_{k\alpha m}(t)$	137
C.7	Non-zero diagrams at $O(g^3)$ in the expansion for $n_{k\alpha m}(t)$	139
D.1	(Color online) Examples of transition graphs between non-orthogonal singlet coverings. The magnitude of the overlap is given by Eq. (D.1). The overlap S_{ab} comes from 1 loop of length 4 (since it involves 4 sites), and represents the largest possible overlap. The overlap S_{ac} comes from 1 loop of length 6 (since it involves 6 sites). In the large- f limit all singlet coverings become orthogonal.	143

D.2 (Color online) Pictorial representation of an orthogonal dimer state constructed from non-orthogonal singlet coverings, expressed in Eq. (5.5). A dimer state $|\bar{a}\rangle$ and its associated singlet covering $|a\rangle$ differ by $\mathcal{O}(f^{-1})$ contribution from all coverings $|b\rangle$ which differ from $|a\rangle$ by two bonds in a flippable plaquette. 143

CHAPTER 1

INTRODUCTION

I like solving puzzles, and I like to believe all physicists do. My approach to solving puzzles is to break it down to its simplest form, and address the essential elements of the puzzle. I have learned to use the same approach to tackle physics problems during my doctoral research. Researchers in physics are experts in formulating simple effective models to describe physical systems. In the 1990s, atomic physicists went to extraordinary lengths to create the simplest form of quantum degenerate matter, a Bose Einstein condensate. In a Bose Einstein condensate (BEC), all its components want to do the same thing. The BEC is like a simple toy which we completely understand, or at least we think we do. In the field of ultracold atoms, we build more components to the toy, and understand how the toy works at each step. Our goal is to keep building the toy until it mimics a giant skyscraper, and understand the structure of the skyscraper. In this analogy, the skyscraper is often a condensed matter system or phenomenon. Condensed matter physicists have been chipping away at these skyscrapers for decades to bare its interior, and formulate the simplest model to describe these systems or phenomena. The crucial advantage with cold atoms is that we added each component of the toy skyscraper, and we know exactly what went in. In this dissertation, I will describe my efforts at designing a few of these skyscrapers, and my efforts at understanding skyscrapers that sometimes were built by others.

The toys in my analogy are Bose gases, Bose Einstein condensates, degenerate Fermi gases, and fermionic superfluids. The additional layers we add to the toys are Raman lasers, Feshbach resonances, optical cavities, and optical lattices. The skyscrapers I refer to are topological superfluids with exotic Majorana excita-

tions, the Kondo effect, fermionic superfluids, driven quantum systems with novel supersolid and charge density wave phases of matter, and magnetically ordered quantum dimer phases. All of these studies have been possible due to significant experimental advances in cooling dilute quantum gases, and developing tools to manipulate and measure their properties with high accuracy.

In my analogy, I have likened condensed matter phenomena to skyscrapers because they are difficult to understand. The difficulty arises from the fact that these phenomena are a consequence of many particles interacting with each other in a complicated way. Cold neutral atoms, however, have weak van der Waals interactions, which are short ranged. The typical range of the van der Waals interaction is a few Angstrom, while the typical inter-particle spacing in a dilute ultracold gas is a few microns. The strength of the short range interaction is parameterized by the s -wave scattering length. A typical s -wave scattering length is a few hundred Bohr, which is also small compared to the inter-particle spacing in dilute gases. However, researchers on ultracold gases can tune the strength, range, and nature of interactions between neutral atoms using several different techniques. Below, we mention some common techniques used to tune atomic interactions.

In one technique, researchers tune their ultracold gas near a Feshbach resonance to make the atomic interactions stronger. In such an experiment, the researchers tune the relative energies of the open channel scattering state and a closed channel molecular bound state via a magnetic field or other control parameters. A Feshbach resonance still produces short range interactions between atoms in the s -wave channel. In a second technique, researchers tune the nature of the interactions by tuning the single particle physics. For example, by loading fermions into a state which is dressed by Raman lasers, the fermions can be made to interact

via long-range interactions in the p -wave channel. One could also use different species of particles, such as molecules with large dipole moments, to obtain long range interactions between the particles. Another method is to induce interactions between atoms, mediated via other particles, such as photons. For example, atoms trapped inside a transversely pumped superradiant optical cavity experience effective interactions that is mediated by the light in the cavity. Finally, virtual hopping of atoms between adjacent sites on a deep lattice is also used to produce novel forms of effective nearest-neighbor interactions between atoms, which drives the formation of exotic phases of matter.

In my dissertation, I have explored several topically relevant questions regarding ultracold atoms. In each case, we find novel physics arising out of the novel nature of the atom-atom interactions produced by using one of the above techniques. Some of my studies have the goal of modeling a certain experiment that was recently performed, and some of my studies propose novel experiments to observe exotic phenomena that occur in condensed matter systems. This dissertation is presented as a collection of these studies. This collection is not presented in chronological order.

In Chapter 2, we explore the physics of exotic Majorana excitations at the edges of one dimensional topological fermionic superfluids. Researchers induce artificial spin-orbit coupling in quasi- one dimensional Fermi gases by dressing them with Raman lasers. Researchers tune the short-range interactions between the fermions in hyperfine states by trapping them in a lattice. In the basis of dressed states created by the Raman lasers, this short-range interaction gets projected into a long-range interaction in the p -wave channel. In this way, researchers can create topological p -wave superfluids. These topological superfluids will have a

doubly degenerate ground state, which contains exotic Majorana modes at their edges. The long range entanglement between the Majorana modes encodes one qubit of information, which is believed to be topologically protected against errors. We describe how microwave spectroscopy can be used to detect, manipulate, and entangle these Majorana excitations. Moreover, the microwaves rotate the system in its degenerate ground state manifold. We use these rotations to implement a set of universal quantum gates, allowing the system to be used as a universal quantum computer. This chapter is adapted from a peer-reviewed article, *Physical Review A* **88**, 063632 (2013), which was co-authored with Prof. Erich Mueller.

In Chapter 3, we explore the physics of lattice bosons with infinite range interactions. This study is motivated by, and models, experiments performed by Landig et al. at ETH Zurich [86]. In this experiment, the researchers have innovated a novel way to produce infinite range interactions between atoms. The researchers loaded a two-dimensional Bose gas in an optical lattice, trapped inside a single mode superradiant Fabry-Perot cavity. The atoms experience an effective infinite-range checkerboard interaction mediated by the light in the cavity. The infinite-range interaction, short-range interaction, and quantum tunneling produce competition between Mott insulator, charge-density wave, superfluid, and supersolid phases. We calculate the phase diagram of this Bose gas in a homogeneous system and in the presence of a harmonic trap. We compare our results with the experimentally measured phase diagram [86]. This chapter is adapted from a peer-reviewed article, *Physical Review A* **94**, 033631 (2016), which was co-authored with Prof. Erich Mueller.

In Chapter 4, we propose a method to realize the Kondo effect using ultracold atoms. The Kondo effect is a transport anomaly that arises when itinerant

fermions have spin-dependent interactions with magnetic impurities. It was first observed in alloys which have magnetic impurities. The anomaly is that the electrical resistance of these alloys has a minimum at a characteristic temperature, and a logarithmic temperature dependence at low temperatures. We propose using an optical Feshbach resonance to engineer Kondo-type spin-dependent interactions in a system with ultracold fermionic ${}^6\text{Li}$ and dilute bosonic ${}^{87}\text{Rb}$ gases. We also propose a scattering experiment to directly observe the Kondo effect in this system. This chapter is adapted from a peer-reviewed article, *Physical Review A* **93**, 023635 (2016), which was co-authored with Prof. Erich Mueller.

In Chapter 5, we propose a method to produce an archetypical quantum dimer model using ultracold atoms. Quantum dimer models have a rich variety of novel phases, including spin liquids, and valence bond solids with large unit cells. The spin liquid phases are said to be precursors to high-temperature superconductors, but have not been conclusively observed in condensed matter systems. In our proposal, we consider a gas of bosons with a large hyperfine spin, loaded in a deep optical lattice. Candidate bosonic species could be ${}^{87}\text{Rb}$ or ${}^{52}\text{Cr}$. We use an optical Feshbach resonance to engineer short range spin-dependent interactions between the atoms. We show that by adjusting the parameters of the Feshbach resonance, we can produce a system whose effective low energy theory is a quantum dimer model. We discuss the ground state for experimentally accessible parameters relevant to our proposal. We also propose an experiment to infer the ground state. The work in the chapter was done in collaboration with Prof. Erich Mueller, Prof. Michael Lawler, and Todd Rutkowski. At the time of writing this dissertation, this chapter is being written up for publication in a peer-reviewed journal, in co-authorship with the collaborators.

Finally, in Chapter 6, we explore a semiclassical approach to quantum mechanics in a study of the dynamics of a fermionic superfluid. Dynamics of fermionic superfluids are often computed by numerically integrating time-dependent Bogoliubov-de-Gennes equations. This integration is often difficult. We develop alternative, complementary tools to compute this dynamics. These tools are based on Wigner functions, whose equations of motion resemble semiclassical Boltzman equations. We show that in the limit of strongly interacting fermions, the semiclassical equations of motion lead to the Gross Pitaevskii equation. We verify the efficiency of the tools we developed by comparing numerical results obtained from numerically integrating time-dependent Bogoliubov-de-Gennes, Gross-Pitaevskii, and semiclassical Boltzman equations. For the numerics, we focused on time-of-flight expansions of fermionic superfluids. Our work has potential applications in all calculations of dynamics of Fermi gases. This work was motivated by several experiments in the the groups of Martin Zwierlein and Randy Hulet, who study solitons in images taken after a time-of-flight expansion. The work in this chapter was done in collaboration with Prof. Erich Mueller.

We summarize in Chapter 7. We also review the experimental progress made in all of the topics of my study, in the years intervening between the completion of our projects and the writing of this dissertation.

CHAPTER 2
UNIVERSAL QUANTUM COMPUTATION WITH MAJORANA
FERMION EDGE MODES THROUGH MICROWAVE
SPECTROSCOPY OF QUASI-1D COLD GASES IN OPTICAL
LATTICES

MANY-BODY PHYSICS USING COLD ATOMS

Bhuvanesh Sundar, Ph.D.

Cornell University 2016

We describe how microwave spectroscopy of cold fermions in quasi-1D traps can be used to detect, manipulate, and entangle exotic nonlocal qubits associated with “Majorana” edge modes. We present different approaches to generate the p -wave superfluidity which is responsible for these topological zero-energy edge modes. We find that the edge modes have clear signatures in the microwave spectrum, and that the line shape distinguishes between the degenerate states of a qubit encoded in these edge modes. Moreover, the microwaves rotate the system in its degenerate ground-state manifold. We use these rotations to implement a set of universal quantum gates, allowing the system to be used as a universal quantum computer. The work in this chapter was done in collaboration with Prof. Erich Mueller. This chapter is adapted from a peer-reviewed article, *Physical Review A* **88**, 063632 (2013), which was co-authored with Prof. Erich Mueller.

In condensed-matter physics, Majorana fermions are exotic collective excitations that possess non-Abelian braiding statistics and are “topologically protected” [119]. They can be used to realize fault-tolerant quantum bits (qubits), an essential ingredient for quantum computing. In this study, we propose a scheme in which microwaves are used to detect Majorana modes in a cold Fermi gas, read out the state of the system, and perform quantum gates.

In a seminal paper, Kitaev showed that one-dimensional (1D) p -wave superfluids support zero-energy Majorana fermion excitations at their edges [78]. Motivated in part by these arguments, researchers have searched for (and found) evidence of Majorana modes in spin-orbit coupled nanowires with proximity-induced superconductivity [114, 136]. In ultracold atomic systems, researchers are attempting to produce Majorana modes using Raman-induced spin-orbit coupling [24, 158]. They have created spin-orbit coupled systems with strongly interacting fermions and measured their radio-frequency spectra [52]. Our proposal builds on these developments. We explain how p -wave superfluidity can be induced in quasi-1D cold gases, and study the interactions of these systems with microwaves. In particular, we describe protocols to produce a set of universal quantum gates.

The ground state of a 1D p -wave superfluid is doubly degenerate. These two ground states can be used as a qubit. The information encoded in this qubit is nonlocal: These states can be distinguished by simultaneously probing the two boundaries of the system or by measuring particle number parity. Mathematically one describes the system as having a Majorana mode at each edge and attributes the degeneracy to these Majorana degrees of freedom.

Detecting Majorana modes is a major challenge and has attracted wide theoretical and experimental interest [114, 136, 159, 145, 173, 72, 152, 84, 102]. In

order to use Majorana edge states as qubits, one must also have the capability to perform projective measurements and quantum gate operations in the degenerate ground-state manifold. Here we note that optical, microwave, or radio probes coherently interact with well-separated regions of a cold-gas system and can be used for detecting and manipulating the delocalized quantum information. We show that the system's microwave-absorption spectrum measures the qubit and show that microwaves also rotate the qubit.

We emphasize that while other spectroscopic techniques can detect the existence of Majorana modes, the microwave absorption spectroscopy studied here can do more: It allows us to measure and manipulate the stored quantum information. Further, while other theoretical studies have explored manipulation of this stored information by interactions of Majorana fermions with microwave cavities [140, 141], we do more: We describe methods to produce all the necessary single- and two-qubit quantum gates for universal quantum computation including initialization and measurement and describe a general framework for producing arbitrary rotations of the qubits.

We envision two possible experimental geometries of superfluids that support Majorana fermions. One geometry consists of a 2D array of 1D superfluid wires with weak interwire tunneling. We believe this is the most experimentally accessible geometry for creating Majorana fermions in cold gases. Multiple wires are advantageous because they enhance the measured signal. Moreover, the interwire tunneling stabilizes long-range superfluid order and allows a mean-field treatment of each wire. The other geometry consists of a single wire embedded in a 3D superfluid bath. While the linear response to microwaves in this geometry is the same as that for an array of wires, the dynamics beyond linear response are different

in these two cases. The protocols necessary for quantum computations work better in this latter geometry. Further the latter geometry connects more closely to experiments with evidence of Majorana fermions in solid state systems.

This chapter is organized as follows. In Sec. 2.1 we briefly review experimental scenarios to realize p -wave superfluidity in arrays of coupled wires and in wires in proximity to a superfluid cloud. In Sec. 2.2 we present our theoretical model for these systems. In Sec. 2.3 we explore the single-particle excitations in this model. In Sec. 2.4 we specialize to the Majorana modes. In Sec. 2.5 we calculate the response of the system to a microwave probe. In Secs. 2.6–2.8 we explain how to implement various quantum gates on single qubits. In Sec. 2.6 we explore the relative time scales required for performing different gate operations. In Sec. 2.7 we discuss our numerical methods for studying the dynamics of the system during gate operations. In Sec. 2.8 we discuss quantum gates through microwave illumination of qubits. In Sec. 2.9 we describe an architecture and algorithms to implement all the quantum gates necessary for universal quantum computation in this system. We summarize in Sec. 2.10.

2.1 Experimental setup

We consider two possible geometries of cold neutral fermionic atoms or molecules that will have Majorana fermion excitations at their edges, a 2D array of 1D wires created by a highly anisotropic optical lattice and a 1D potential valley on the surface of an atom chip embedded in a large 3D superfluid cloud. In the first geometry a weak interwire tunneling stabilizes superfluidity in the wires. In the second geometry superfluidity is induced in the wire due to the proximity effect.

Below we propose experimental implementations of these two geometries. We discuss methods to create p -wave superfluids in these geometries. We supplement these discussions with calculations of experimental parameters in the coupled-wire geometry.

2.1.1 Coupled Wires

First we study a fermionic gas trapped in a 2D array of 1D wires created by a highly anisotropic optical lattice: hopping in the y and z directions is strongly suppressed compared to that in the x direction. Such an array is readily produced by interfering several lasers [95]. p -wave superfluidity will be favored if there are strong nearest-neighbor interactions in each wire. Below we review a few methods to generate such interactions. In Appendix A.1 we calculate the superfluid gap (Δ) created by these interactions. For our proposals to work, we would like the gap Δ to be such that Δ/k_B is on the order of or larger than a few nanokelvins, which is the typical temperature of these gases. For reference, $\hbar \cdot 1 \text{ kHz} = k_B \cdot 7.64 \text{ nK}$.

The conceptually simplest way to generate nearest-neighbor (or longer-ranged) interactions involves using neutral molecules such as KRb or LiCs that have large dipole moments [11]. Interactions between the molecules can be controlled by applying an electric field, which adjusts the alignment of their dipole moments. The dipole moments of these molecules are typically of the order of 10 D, which creates interactions of strengths in the kHz range between nearest neighbors on a lattice with lattice spacing of a few μm . As shown in Appendix A.1, the superfluid gap will then be in the kHz range.

A second method to create nearest-neighbor interactions uses spin-orbit coupled

atoms in the lower helicity state. Here one shines two counter propagating lasers on two spin species of fermionic atoms such as ^{40}K or ^6Li . The resulting dressed atomic levels are described by a Hamiltonian analogous to spin-orbit coupled electrons in a semiconducting wire. When projected into the lower dressed band, effective separable long-range atomic interactions emerge [158]. Current experiments using ^{40}K [158] achieve spin-orbit coupling strengths and Zeeman splitting between the dressed states in the kHz range. In Appendix A.1 we show that the resulting superfluid gap will be of order kHz.

A third method to create nearest-neighbor interactions is to engineer significant overlap of Wannier functions at adjacent lattice sites. One such example is to use spin-dependent lattices, outlined in [145]. We show in Appendix A.1 that the resulting superfluid gap would be of order MHz.

All of the methods outlined above create effectively spinless fermions in one band “a” which have interactions that extend beyond a single site. While these techniques generate interactions of various ranges, the essential physics is captured by a model with only nearest-neighbor interactions. We work with this simplified model.

2.1.2 Proximity-Induced Superfluid

We also consider a geometry where a single wire is immersed in a superfluid cloud. Superfluidity is induced in the wire due to the proximity effect. This is the geometry realized in solid-state experiments, where semiconductor wires are in contact with a superconductor [114]. One way to realize this geometry in a gas of cold atoms is to put an *s*-wave superfluid of ^6Li or ^{40}K near an atom chip [123]. Current-

carrying wires on the atom chip create a 1D potential valley for the atoms. We envision a bimodal population, with a large 3D cloud surrounding a tightly confined 1D gas. We artificially induce spin-orbit coupling in the 1D gas by shining Raman lasers along the potential valley. By keeping the beam waist small, the Raman lasers have minimal effect on the 3D cloud. If desired, an optical lattice can be added to the potential valley. The superfluid cloud acts as a bath of Cooper pairs which tunnel into the 1D wire; hence, a superfluid order parameter is induced in the chain of atoms. The artificially induced spin-orbit coupling projects these pairs onto dressed bands. In the lower dressed band the induced order parameter has p -wave character.

2.1.3 Trap and Probe

Most experiments in both geometries are performed in the presence of harmonic potentials. As explicitly shown by Wei and Mueller [159] for the case of spin-orbit coupled atoms, the physics of Majorana fermions in a harmonic trap is identical to that in an infinite square well. Experimentally infinite square wells can be engineered with “tube beams” and “sheet beams” [55]. For simplicity, we predominantly model the confinement as an infinite square well. In Sec. 2.5.3 we also include calculations in a harmonic trap.

To probe the Majorana modes in the 1D superfluid, we propose driving a transition to another atomic state “c” by shining electromagnetic waves on the system. We consider the case of microwaves or radiowaves, where the wavelength is larger than the system size (0.1 – 1mm). If the bandwidth of the Bloch waves in the “c” states is small compared to Δ , we find that the spectral signature of the Majorana modes is well separated from the bulk modes, and the spectral line shape can dis-

tinguish which of the two degenerate ground states is present. Researchers have been able to create spin-dependent lattices with different bandwidths for different hyperfine states of bosonic atoms [101]. We anticipate that similar techniques can be used to independently control the bandwidths of the fermionic “a” and “c” states in our system as well.

2.2 Theoretical model

The two geometries discussed in the previous section are modeled by slightly different effective Hamiltonians. The cause of the difference is the mechanism inducing superfluidity in the wires. In the coupled-wire geometry, the superfluid order parameter Δ is determined self-consistently from the properties of the wires, while in the case of a proximity-induced superfluid, Δ is imposed by the surrounding bath. Below we present the Hamiltonian governing our system in these two cases.

2.2.1 Coupled Wires

The ensemble of wires described in Sec. 2.1.1 is modeled by the effective Hamiltonian

$$\hat{H} = \hat{H}_a + \hat{H}_c + \hat{H}_{\text{MW}} + \hat{H}_{\text{iw}}. \quad (2.1)$$

The atoms in the “a” states are described by a tight-binding model,

$$\hat{H}_a = \sum_i \sum_{j=1}^{N-1} -J \left(\hat{a}_j^{(i)\dagger} \hat{a}_{j+1}^{(i)} + \hat{a}_{j+1}^{(i)\dagger} \hat{a}_j^{(i)} \right) + V \hat{a}_j^{(i)\dagger} \hat{a}_{j+1}^{(i)\dagger} \hat{a}_{j+1}^{(i)} \hat{a}_j^{(i)} - \sum_i \sum_{j=1}^N \mu \hat{a}_j^{(i)\dagger} \hat{a}_j^{(i)}, \quad (2.2)$$

where J is the hopping amplitude, V is the nearest-neighbor interaction strength, μ is the chemical potential, and $\hat{a}_j^{(i)\dagger}$ and $\hat{a}_j^{(i)}$ create and annihilate spinless fermions

in the “a” state at site j in the i^{th} wire. We model the interwire coupling via

$$\hat{H}_{\text{iw}} = \sum_{\langle ii' \rangle} \sum_{j=1}^N -J' \left(\hat{a}_j^{(i)\dagger} \hat{a}_j^{(i')} + \hat{a}_j^{(i')\dagger} \hat{a}_j^{(i)} \right) + V' \hat{a}_j^{(i)\dagger} \hat{a}_j^{(i')\dagger} \hat{a}_j^{(i')} \hat{a}_j^{(i)} \quad (2.3)$$

where J' and V' parametrize the interwire hopping and interactions, respectively. All adjacent pairs of wires $\langle ii' \rangle$ are summed over. In the limit of $J' \ll J$ and $V' \ll V$, \hat{H}_{iw} has only a perturbative role in this mean-field theory and can be neglected. Under a mean-field approximation, each wire is then equivalent, and we can drop the index labeling the wires from our operators. We emphasize, however, that the presence of this interwire hopping is important as it stabilizes long-range order and justifies our mean-field approximation. The mean-field Hamiltonian describing the “a” atoms or molecules is then

$$\hat{H}_{\text{MF}} = E_0 + \sum_{j=1}^{N-1} \left[-J \left(\hat{a}_j^\dagger \hat{a}_{j+1} + \hat{a}_{j+1}^\dagger \hat{a}_j \right) - \left(\Delta_j \hat{a}_j^\dagger \hat{a}_{j+1}^\dagger + \Delta_j^* \hat{a}_{j+1} \hat{a}_j \right) \right] - \sum_{j=1}^N \mu \hat{a}_j^\dagger \hat{a}_j, \quad (2.4)$$

where the local order parameter Δ_j is defined self-consistently as

$$\Delta_j = -V \langle \hat{a}_{j+1} \hat{a}_j \rangle, \quad (2.5)$$

and E_0 is an irrelevant energy shift. Δ_j can always be chosen to be real and positive by a local gauge transformation of the creation and annihilation operators of the “a” atoms or molecules. Moreover, one can also take Δ_j to be symmetric under reflection, $\Delta_j = \Delta_{N-j}$.

Microwaves can change the internal state of the atoms or molecules, introducing a term in the Hamiltonian of the form

$$\hat{H}_{\text{MW}} = \Omega \sum_{j=1}^N \left(\hat{c}_j^\dagger \hat{a}_j e^{-i\omega t} + \hat{a}_j^\dagger \hat{c}_j e^{i\omega t} \right). \quad (2.6)$$

The operators \hat{c}_j and \hat{c}_j^\dagger correspond to excited atoms or molecules. These excited particles generally feel a different lattice, and are described by a tight-binding

model

$$\hat{H}_c = \sum_j -J_c \left(\hat{c}_j^\dagger \hat{c}_{j+1} + \hat{c}_{j+1}^\dagger \hat{c}_j \right) - \mu_c \hat{c}_j^\dagger \hat{c}_j, \quad (2.7)$$

where J_c is the hopping amplitude and μ_c is the chemical potential. The frequency ω in Eq. (2.6) is related to the real frequency of electromagnetic waves via

$$\omega = \omega_{\text{physical}} - \delta\epsilon + \mu - \mu_c, \quad (2.8)$$

where ω_{physical} is the real electromagnetic frequency and $\delta\epsilon$ is the absorption frequency in free space.

2.2.2 Proximity-Induced Superfluid

A proximity-induced superfluid will be governed by the effective Hamiltonian

$$\hat{H} = \hat{H}_a + \hat{H}_c + \hat{H}_{\text{MW}}. \quad (2.9)$$

The “a” states are described by a tight-binding model

$$\hat{H}_a = \sum_{j=1}^{N-1} \left[-J \left(\hat{a}_j^\dagger \hat{a}_{j+1} + \hat{a}_{j+1}^\dagger \hat{a}_j \right) - \left(\Delta_j \hat{a}_j^\dagger \hat{a}_{j+1}^\dagger + \Delta_j^* \hat{a}_{j+1} \hat{a}_j \right) \right] - \sum_{j=1}^N \mu \hat{a}_j^\dagger \hat{a}_j, \quad (2.10)$$

where J is the hopping amplitude, Δ_j is the order parameter induced at site j from the bath, μ is the chemical potential, and \hat{a}_j^\dagger and \hat{a}_j create and annihilate spinless fermions in the “a” state at site j in the wire. \hat{H}_{MW} and \hat{H}_c are given by Eqs. (2.6) and (2.7). The model for proximity-induced superfluids is simpler because as long as the bath is large enough, Δ_j are constant parameters and need not be self-consistently determined from the properties of the wire.

2.2.3 Other Considerations

In this study we analyze the case where interactions between “a” and “c” atoms or molecules can be neglected. For example, this would be the case for spin-orbit coupled ^{40}K near a Feshbach resonance. Such final-state interactions can be modeled by using the techniques from [13].

2.3 Bogoliubov excitations

In this section, we analyze the quasiparticles of the mean-field theory. We give particular emphasis to their properties under reflection and derive relations that will be useful in the next section. We explore the local density of states associated with our mean-field model in Eqs. (2.4) and (2.10) and verify that a zero-energy mode appears at the boundaries. We include a brief qualitative discussion of the full coupled-wire model with the interwire coupling at the end of this section.

Equations (2.4) and (2.10) can be rewritten as

$$\hat{H}_{\text{MF}} = E'_0 + \sum_{\nu} E_{\nu} \hat{\gamma}_{\nu}^{\dagger} \hat{\gamma}_{\nu}, \quad (2.11)$$

where E'_0 is an irrelevant energy shift. The creation operator for the quasiparticles, which are superpositions of particles and holes, are of the form

$$\hat{\gamma}_{\nu}^{\dagger} = \sum_{j=1}^N u_{\nu}(j) \hat{a}_j^{\dagger} + v_{\nu}(j) \hat{a}_j, \quad (2.12)$$

where N is the number of sites. Since all the parameters in our mean-field model are real, we can always choose $u_{\nu}(j)$ and $v_{\nu}(j)$ to be real.

The coherence factors $u_{\nu}(j)$ and $v_{\nu}(j)$ at different sites are not completely independent of each other. We consider an operator that performs a simultaneous

reflection and a global gauge transformation,

$$\hat{Q}\hat{a}_j\hat{Q}^\dagger = i\hat{a}_{N+1-j}. \quad (2.13)$$

Under the assumption that $\Delta_j = \Delta_{N-j}$, this operator represents a symmetry of the mean-field Hamiltonian, $[\hat{Q}, \hat{H}_{\text{MF}}] = 0$. Barring any degeneracies, this symmetry implies that $[\hat{Q}, \hat{\gamma}_\nu^\dagger \hat{\gamma}_\nu] = 0 \forall \nu$. Consequently, \hat{Q} acts a gauge transformation on the quasiparticle operators, $\hat{Q}\hat{\gamma}_\nu^\dagger\hat{Q}^\dagger = \lambda_\nu\hat{\gamma}_\nu^\dagger$. Direct computation starting from Eq. (2.13) yields $\hat{Q}^2\hat{\gamma}_\nu^\dagger\hat{Q}^{\dagger 2} = -\hat{\gamma}_\nu^\dagger$. Hence, $\lambda_\nu = \pm i$. When $\lambda_\nu = -i$, $u_\nu(j)$ is symmetric under reflection and $v_\nu(j)$ is antisymmetric under reflection: $u_\nu(N+1-j) = u_\nu(j)$, $v_\nu(N+1-j) = -v_\nu(j)$. In this case the quasiparticle creation operators have the form

$$\hat{\gamma}_\nu^{(s)\dagger} = \sum_j f_\nu^{(s)}(j) \frac{\hat{a}_j^\dagger + \hat{a}_j + \hat{a}_{N+1-j}^\dagger - \hat{a}_{N+1-j}}{2}, \quad (2.14)$$

where $f_\nu^{(s)}(j) = u_\nu(j) + v_\nu(j)$. When $\lambda_\nu = i$, $u_\nu(j)$ is antisymmetric under reflection and $v_\nu(j)$ is symmetric under reflection: $u_\nu(N+1-j) = -u_\nu(j)$, $v_\nu(N+1-j) = v_\nu(j)$. In this case the quasiparticle creation operators have the form

$$\hat{\gamma}_\nu^{(a)\dagger} = \sum_j f_\nu^{(a)}(j) \frac{\hat{a}_j + \hat{a}_j^\dagger + \hat{a}_{N+1-j}^\dagger - \hat{a}_{N+1-j}}{2}, \quad (2.15)$$

where again $f_\nu^{(a)}(j) = u_\nu(j) + v_\nu(j)$. These modified forms will be helpful in our analysis of Majorana modes in Sec. 2.4.

The local density of states in the superfluid at energy E and position j is given by

$$\begin{aligned} A(j, E) &= 2\text{Im} \left(\langle \hat{a}_j \frac{1}{E - \hat{H}} \hat{a}_j^\dagger \rangle + \langle \hat{a}_j^\dagger \frac{1}{E + \hat{H}} \hat{a}_j \rangle \right) \\ &= 2\pi \sum_\nu [|u_\nu(j)|^2 \delta(E - E_\nu) + |v_\nu(j)|^2 \delta(E + E_\nu)], \end{aligned} \quad (2.16)$$

where δ is the Dirac δ function, and all quasiparticle indices ν have been summed over. We illustrate this density of states in Fig. 2.1, marking a point in the

position-energy plane at the locations of the Dirac δ functions, with darker points representing higher amplitudes of the δ functions. The pair of zero-energy peaks visible in Fig. 2.1 are Majorana modes. These Majorana modes are zero-energy solutions to the Bogoliubov-deGennes equations, that are exponentially localized at the two ends [78]. They always occur in pairs at opposite ends of the 1D superfluid and are always found if $|\mu| < 2J$, where the superfluid is in a topologically non-trivial phase.

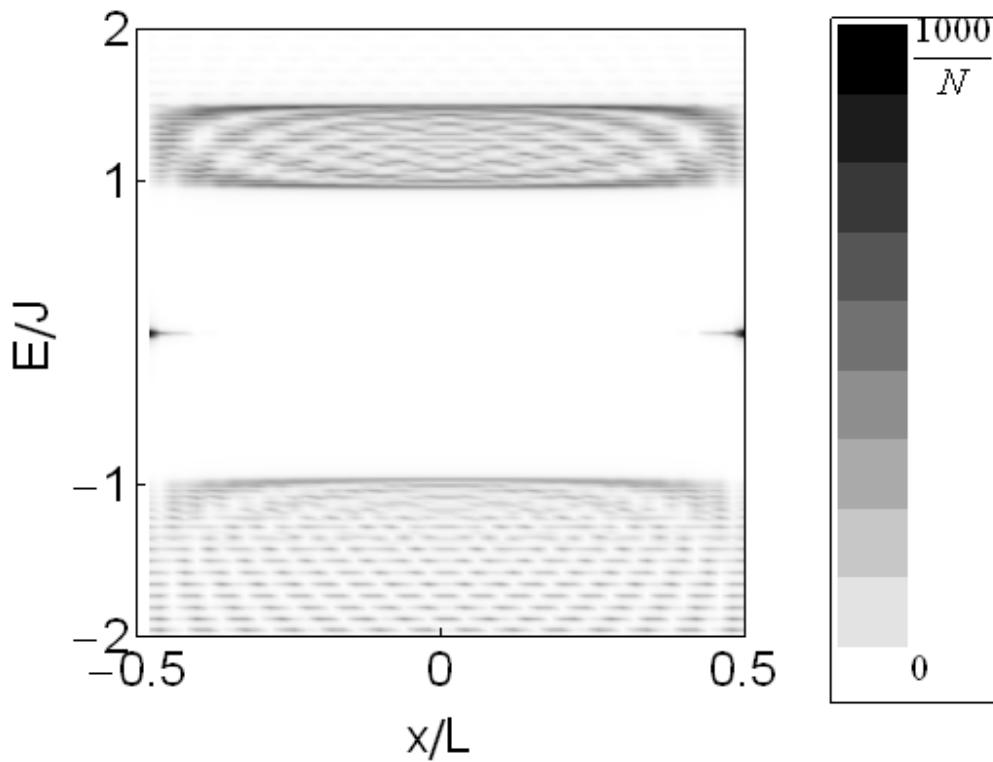


Figure 2.1: Local single-particle density of states for the mean-field model in Eq. (2.10) with parameters $\Delta_j = \mu = 0.25J, N = 50$. The local density of states is a sum of Dirac δ functions. Darker shades represent higher amplitudes of the Dirac δ functions. We can observe bulk quasiparticles with $E_\nu > 0$ and zero-energy ($E_\nu = 0$) excitations at the edges. These zero-energy modes are Majorana modes.

To explore the robustness of these spectra, we also carried out the analogous

calculation using a multi-wire mean field theory,

$$\begin{aligned} \hat{H}_{\text{MWMF}} = & \sum_i \sum_{j=1}^N [-J (\hat{a}_j^{(i)\dagger} \hat{a}_{j+1}^{(i)} + \hat{a}_{j+1}^{(i)\dagger} \hat{a}_j^{(i)}) - (\Delta_j \hat{a}_j^{(i)\dagger} \hat{a}_{j+1}^{(i)\dagger} + \Delta_j^* \hat{a}_{j+1}^{(i)} \hat{a}_j^{(i)}) - \mu \hat{a}_j^{(i)\dagger} \hat{a}_j^{(i)}] \\ & - J' \sum_{\langle ii' \rangle} \sum_{j=1}^N (\hat{a}_j^{(i)\dagger} \hat{a}_j^{(i+1)} + \hat{a}_j^{(i+1)\dagger} \hat{a}_j^{(i)}) \end{aligned} \quad (2.17)$$

with J and Δ_j comparable in magnitude and $\mu = 0$. The interwire coupling J' has very little effect on the spectrum, even when it is a sizable fraction of J . In particular, the edge modes stay at zero energy. Hence, our assumption that \hat{H}_{iw} only plays a perturbative role is valid, and it is sufficient to work with our mean-field model in Eqs. (2.4) and (2.10) hereafter.

2.4 Majorana modes

The $E_\nu = 0$ quasiparticle in Eq. (2.11) is composed of two Majorana modes. Since this excitation is localized at the edges, we denote its creation operator by $\hat{\gamma}_{\text{edge}}^\dagger$. There is an ambiguity in the definition of $\hat{\gamma}_{\text{edge}}^\dagger$, as the canonical transformation $\hat{\gamma}_{\text{edge}} \rightarrow \hat{\gamma}_{\text{edge}}^\dagger, \hat{\gamma}_{\text{edge}}^\dagger \rightarrow \hat{\gamma}_{\text{edge}}$ is a symmetry of the system. Somewhat arbitrarily, we define $\hat{\gamma}_{\text{edge}}^\dagger$ by its properties under \hat{Q} , $\hat{Q} \hat{\gamma}_{\text{edge}}^\dagger \hat{Q}^\dagger = -i \hat{\gamma}_{\text{edge}}^\dagger$. With this choice,

$$\hat{\gamma}_{\text{edge}}^\dagger = \sum_j f_0(j) \left(\frac{\hat{a}_j^\dagger + \hat{a}_j}{2} + i \frac{\hat{a}_{N+1-j}^\dagger - \hat{a}_{N+1-j}}{2i} \right). \quad (2.18)$$

The coherence factors $f_0(j)$ are real and satisfy

$$(J - \Delta_{j-1})f_0(j-1) + (J + \Delta_j)f_0(j+1) + \mu f_0(j) = 0, 1 < j < N. \quad (2.19)$$

For the proximity-induced case with uniform $\Delta_j = \Delta$, the above equation can be

solved explicitly [78]. The resulting solution has the form

$$\begin{aligned}
f_0(j) &= \alpha(x_+^j - x_-^j), & \text{if } x_+, x_- \neq 0 \text{ and } \frac{1}{x_+}, \frac{1}{x_-} \neq 0, \\
f_0(j) &= \delta_{j1}, & \text{if } x_+ = x_- = 0, \\
f_0(j) &= \delta_{jN}, & \text{if } \frac{1}{x_+} = \frac{1}{x_-} = 0,
\end{aligned} \tag{2.20}$$

where

$$x_{\pm} = \frac{\mu}{2(J + \Delta)} \pm \sqrt{\left(\frac{\mu}{2(J + \Delta)}\right)^2 + \frac{\Delta - J}{\Delta + J}}, \tag{2.21}$$

α is a normalization constant, and δ is the Kronecker δ . A derivation of Eq. (2.20) is provided in Appendix A.2. The coherence factors $f_0(j)$ exponentially decay away from the boundaries. They are sharply peaked at $j = 1$ if $\Delta > 0$, and peaked at $j = N$ if $\Delta < 0$. Numerical solutions for the coupled-wire case where Δ_j are determined self-consistently usually result in nearly uniform $\Delta_j = \Delta$. Therefore the expressions in Eq. (2.20) are qualitatively applicable to the coupled-wire case as well.

As explained by Kitaev [78], the physics is particularly simple if

$$\mu = 0, V = -4J, \tag{2.22}$$

parameters which yield uniform $\Delta_j = J$. For these parameters, the energy gap for bulk Bogoliubov excitations is $2J$ and their bandwidth is zero. The coherence factors are $f_0(j) = \delta_{j1}$. While the bulk of our calculations are performed for generic parameters, this simple limit in Eq. (2.22) is useful for qualitatively understanding the results.

Since $\hat{\gamma}_{\text{edge}}^\dagger$ creates an excitation of zero energy, the mean-field models in Eqs.(2.4) and (2.10) have two degenerate ground states, $|g_-\rangle$ and $|g_+\rangle$. We identify $|g_-\rangle$ with the quasiparticle vacuum, characterized by

$$\hat{\gamma}_\nu |g_-\rangle = 0 \quad \forall \nu, \tag{2.23}$$

and then define

$$|g_+\rangle = \hat{\gamma}_{\text{edge}}^\dagger |g_-\rangle. \quad (2.24)$$

$|g_+\rangle$ and $|g_-\rangle$ are eigenstates of the particle number parity operator $\hat{P} = (-1)^{\sum_j \hat{a}_j^\dagger \hat{a}_j}$. For the choice of $\hat{\gamma}_{\text{edge}}^\dagger$ we made in Eq. (2.18), $\hat{P}|g_+\rangle = -|g_+\rangle$ and $\hat{P}|g_-\rangle = |g_-\rangle$. We use the states $|g_+\rangle$ and $|g_-\rangle$ to encode physical qubits.

In the case of multiple wires, we assume that all the wires are in the same state. The statement that “the” qubit is in the state $|g_+\rangle$ denotes that all the wires are in $|g_+\rangle$.

In the next section we show how to projectively measure physical qubits in the basis of $|g_+\rangle$ and $|g_-\rangle$. We find in Sec. 2.8 that to perform universal quantum computation, we need a more sophisticated architecture in which logical qubits are constructed from more than one physical qubit. Manipulations of the logical qubits consist of manipulations of the component physical qubits. In Secs. 2.6–2.8, we describe algorithms for implementing quantum gates on physical qubits and the logic behind them. Finally, in Sec. 2.9 we show how to perform universal quantum computation using logical qubits constructed from physical qubits.

2.5 Absorption spectrum

The superfluid’s electromagnetic absorption spectrum is given by

$$\Gamma(|i\rangle, \omega) = \sum_f \frac{2\pi}{\hbar} |\langle f | \hat{H}_{\text{MW}} | i \rangle|^2 \delta(\omega - (E_f - E_i)), \quad (2.25)$$

where $|i\rangle$ is the initial state and $|f\rangle$ are the final states, and E_i and E_f are their respective energies. The final states $|f\rangle$ have one quasiparticle of energy E_ν and

one atom in the excited state, created by

$$\hat{c}_k^\dagger = \sum_j \psi_k(j) \hat{c}_j^\dagger, \quad (2.26)$$

where \hat{c}_k^\dagger diagonalize the tight-binding Hamiltonian in Eq. (2.7) for the excited atoms:

$$\hat{H}_c = \sum_k \epsilon_k \hat{c}_k^\dagger \hat{c}_k. \quad (2.27)$$

In the case of a translationally invariant system, k would label momentum. We consider more generic cases here, and let k simply be a label of the excited states. We denote the energies of the lowest and highest energy “c” states as $\min(\epsilon_k)$ and $\max(\epsilon_k)$ and the bottom and top of the bulk “a” Bogoliubov spectrum as $\min(E_\nu)$ and $\max(E_\nu)$, where we take $E_\nu > 0$; i.e, we exclude the zero-energy edge state in defining these ranges. The bulk excitations contribute to the absorption spectrum in Eq. (2.25) for $\min(\epsilon_k) + \min(E_\nu) < \omega < \max(\epsilon_k) + \max(E_\nu)$. The edge modes contribute to the spectral weight in the range $\min(\epsilon_k) < \omega < \max(\epsilon_k)$. We consider the case where these spectral features are well separated and restrict ourselves to the edge spectrum.

In terms of the wave functions $\psi_k(j)$, Eq. (2.25) simplifies to

$$\Gamma(|g_\pm\rangle, \omega) = \frac{2\pi|\Omega|^2}{\hbar} \sum_k \delta(\omega - \epsilon_k) \times \left| \sum_j f_0(j) (\psi_k(j) \pm \psi_k(N+1-j)) \right|^2, \quad (2.28)$$

where $f_0(j)$ are the coherence factors for the edge state in Eq. (2.18), δ is the Dirac δ function, and all excitation indices k and sites j have been summed over.

In the simple case where $\mu = 0$, $\Delta_j = J$, Eq. (2.28) further simplifies to

$$\Gamma(|g_\pm\rangle, \omega) = \frac{2\pi|\Omega|^2}{\hbar} \sum_k |\psi_k(1) \pm \psi_k(N)|^2 \delta(\omega - \epsilon_k). \quad (2.29)$$

Equation (2.28) tell us that the amplitudes of electromagnetic absorption at the two ends of the wire interfere with each other, and the phase associated with

absorption at the ends of the wire is different in the states $|g_+\rangle$ and $|g_-\rangle$. This generically leads to different spectral weights $\Gamma(|g_+\rangle, \omega)$ and $\Gamma(|g_-\rangle, \omega)$, and enables us to measure the state of the qubit. For an arbitrary superposition of the two states, the spectral weight is given by

$$\Gamma(\alpha|g_+\rangle + \beta|g_-\rangle, \omega) = |\alpha|^2\Gamma(|g_+\rangle, \omega) + |\beta|^2\Gamma(|g_-\rangle, \omega). \quad (2.30)$$

The wave functions $\psi_k(j)$ depend on how the “c” atoms are confined. In the following, we discuss a range of boundary conditions on the “c” atoms.

2.5.1 Periodic Boundary Conditions

While difficult to implement experimentally, the simplest boundary conditions for theoretical study are periodic. Specifically, we consider a case where the “a” atoms are trapped by an optical lattice in a ring geometry consisting of N sites with lattice spacing a . A potential barrier (for example, generated by a blue-detuned laser) prevents hopping along one bond, providing edges to the system. We imagine that the “c” atoms are also confined to a ring, but do not see the barrier.

In this geometry, the analysis is simple as the eigenstates in Eq. (2.26) are plane waves with wave functions

$$\psi_k(j) = \frac{e^{ikr_j}}{\sqrt{N}}, \quad (2.31)$$

where r_j is the position of the site labeled by j , and the quantized momenta k obey $e^{iNka} = 1$. The spectral weights are then given by

$$\Gamma(|g_\pm\rangle, \omega) = \frac{2\pi|\Omega|^2}{N\hbar} \sum_k \delta(\omega - \epsilon_k) \times \left| \sum_j f_0(j) (e^{ikr_j} \pm e^{ika}e^{-ikr_j}) \right|^2, \quad (2.32)$$

where $\epsilon_k = -2J_c \cos ka - \mu_c$, J_c is the hopping amplitude of the excited atoms, and μ_c is the chemical potential. In this case $|g_+\rangle$ and $|g_-\rangle$ have clearly distinguishable spectra. For example, at microwave frequency $\omega = -2J_c - \mu_c$, only the uniform wave function ($k = 0$) contributes to the spectral weight, and $\Gamma_-(-2J_c - \mu_c) = 0$. Similarly, $\Gamma_+(2J_c - \mu_c) = 0$.

In the special case of Eq. (2.22), where we took $\mu = 0$ and $\Delta_j = J$,

$$\Gamma(|g_{\pm}\rangle, \omega) = \frac{-2|\Omega|^2}{J_c \hbar} \frac{-2J_c \pm (\omega + \mu_c)}{\sqrt{(2J_c)^2 - (\omega + \mu_c)^2}}. \quad (2.33)$$

This spectrum is plotted in Fig. 2.2(a). For this special case, one sees that $\Gamma_+(\omega)$ is monotonically decreasing while $\Gamma_-(\omega)$ is monotonically increasing. This behavior is special to these parameters, and, as shown in Fig. 2.2(b), the spectra could, in general, have a richer structure.

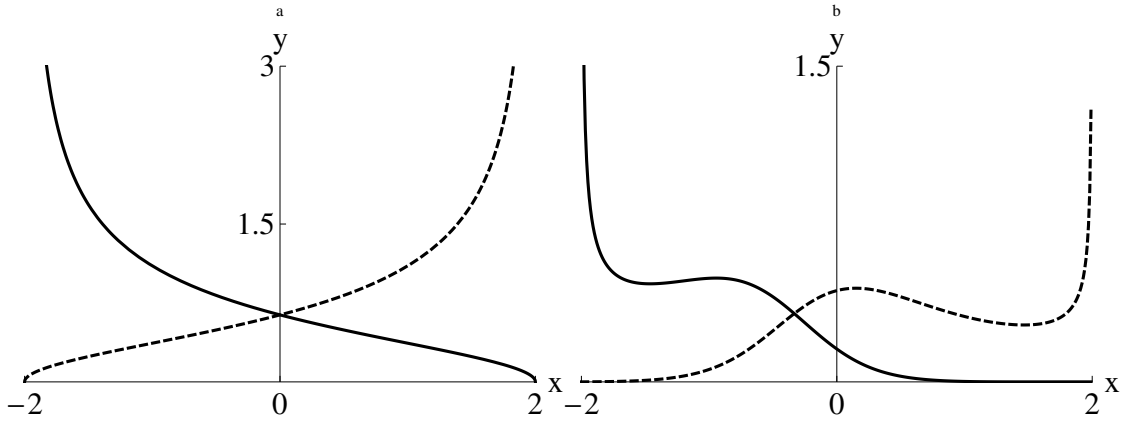


Figure 2.2: The electromagnetic absorption spectrum when atoms are excited from the “a” state to the “c” state with periodic boundary conditions. The solid curve is the absorption spectrum of $|g_+\rangle$ and the dashed curve of $|g_-\rangle$. Parameters chosen in (a) are $\Delta_j = J, \mu = 0, N = 30$, and in (b) are $\Delta_j = J/2, \mu = J/4, N = 30$. The parameters used in (b) are not a self-consistent solution of the mean-field approximation [Eq. (2.19)]. If instead we find Δ_j self-consistently, the spectra do not change significantly.

2.5.2 Infinite Square Well

Here we consider an experimentally simpler case where both the “a” and the “c” atoms are trapped in a linear geometry by an optical lattice of length L and lattice spacing a and with hard-wall boundary conditions. The wave functions of the “c” atoms are

$$\psi_k(j) = \frac{\sqrt{2} \sin kr_j}{\sqrt{N}}, \quad (2.34)$$

where the allowed values of k are $n\pi/(N+1)$ for integer values of n . The spectra, given by

$$\Gamma(|g_{\pm}\rangle, \omega) = \frac{4\pi|\Omega|^2}{N\hbar} \sum_k \delta(\omega - \epsilon_k) \times \left| \sum_j f_0(j) (\sin kr_j \pm \sin k((N+1)a - r_j)) \right|^2, \quad (2.35)$$

now have a richer, inter-digitated structure. They are plotted in Fig. 2.3(a) for a small lattice in the special case of Eq. (2.22), where $f_0(j) = \delta_{j1}$.

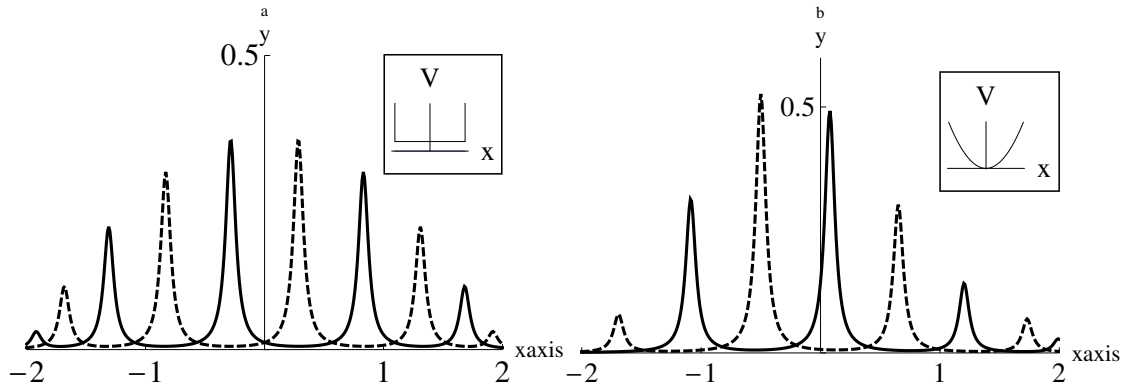


Figure 2.3: The electromagnetic absorption spectrum when atoms are excited from the “a” state to the “c” state with open boundary conditions. (a) The atoms are trapped in a lattice with 10 sites and hard walls at its ends. (b) The atoms are trapped in a harmonic trap so that the distance between the Majorana modes is 10 sites. In (b), μ_c refers to the chemical potential of the “c” atoms at the center of the trap. The solid curve is the absorption spectrum of $|g_+\rangle$, and the dashed curve of $|g_-\rangle$. Insets show the confining potential minus the optical lattice.

Figure 2.3 illustrates that the spectra exhibit $N/2$ oscillations within a fre-

quency range equal to the bandwidth of the “c” atoms. As the system becomes longer, the spectra develop more closely spaced oscillations. In the thermodynamic limit, high-frequency resolution is needed to differentiate $|g_+\rangle$ and $|g_-\rangle$. Depending on the bandwidth of the “c” atoms and the experimentally achievable frequency resolution, this places an upper limit on the length of the superfluid. A lower limit is placed by the hybridization of the edge modes. In experiments involving 1D optical lattices [95], N is typically of the order of 100. As explained at the beginning of this section, the bandwidth of the “c” atoms must be less than the superfluid gap in order to separate the spectral features of the bulk and edge modes. As explained in Sec. 2.1, the superfluid gap produced by different techniques is in the kHz–MHz range. Therefore, the frequency resolution needed to resolve the interdigitated absorption spectra is on the order of kHz.

2.5.3 Harmonic Traps

Finally we consider the most experimentally realistic case where both the “a” atoms and “c” atoms are trapped by a harmonic potential. The effect of introducing a harmonic trap is twofold: The individual peaks shift to higher frequencies while the envelope shifts to lower frequencies [see Fig. 2.3(b)]. Qualitatively, however, the spectrum is nearly indistinguishable from a hard-wall trap. We numerically calculate and plot the result for a small lattice in a harmonic trap in Fig. 2.3(b).

2.6 Dynamics

To use our system to process quantum information we need algorithms to implement quantum gates. Here we construct gates based on microwave illumination. Each photon absorbed or emitted flips an atom between the “a” state and the “c” state, creating a quasiparticle and changing the particle number parity of the “a” atoms. In the appropriate frequency range, this parity change corresponds to flipping between $|g_+\rangle$ and $|g_-\rangle$. We envision that we can utilize this feature to perform gate operations. For example, if a microwave pulse is applied to a qubit in a state $|\psi_i\rangle = \alpha|g_-\rangle \otimes |0\rangle + \beta|g_+\rangle \otimes |0\rangle$, the qubit will evolve to $|\psi_f\rangle = \alpha(\cos \phi_-|g_-\rangle \otimes |0\rangle + \sin \phi_-|g_+\rangle \otimes |c_1\rangle) + \beta(\cos \phi_+|g_+\rangle \otimes |0\rangle + \sin \phi_+|g_-\rangle \otimes |c_2\rangle)$ after a time t , where $|0\rangle$ is the vacuum of “c” atoms, $|c_1\rangle$ and $|c_2\rangle$ are single-particle “c” states, and \otimes is the Cartesian product.

In the strongly coupled regime $\Omega > J_c$ and the weakly coupled regime $\Omega < J_c/N$, we show in Sec. 2.8.2 that we can arrange $\phi_- = \pm\pi/2, \phi_+ = \pm\pi/2$ and $|c_1\rangle = |c_2\rangle$. Under these circumstances, the “c” atoms are disentangled from the qubit, and we have produced an X or a Y gate (so named because they act as Pauli operators σ_x or σ_y). The implementation of the X and Y gates will be explicitly demonstrated in Sec. 2.8.2. Composing these operations yields a Z gate. We show in Sec. 2.9 that more complicated (universal) gates can be implemented by using composite logical qubits.

In the intermediate regime $J_c > \Omega > J_c/N$, we show in Sec. 2.8.1 that we can arrange $\phi_- = \pi/2, \phi_+ = 0$. Here the final state will be $|\psi_f\rangle = |g_+\rangle \otimes (\alpha|c_1\rangle + \beta|0\rangle)$. The “c” atoms are in a superposition of number eigenstates, but because of the product structure, they have no impact on future gate operations. Thus, this acts as a SET gate which projectively initializes the qubit in $|g_+\rangle$. To set the qubit in

$|g_-\rangle$, we arrange $\phi_+ = \pi/2, \phi_- = 0$.

Since the gates substantially change the state, they cannot be described by linear response. This motivates us to study the full quantum dynamics in Sec. 2.7. In Sec. 2.8 we propose algorithms to implement various gates, and use the numerical methods described in Sec. 2.7 to observe the dynamics during the gate operations.

2.7 Numerical Methods

To study the dynamics of the system we work in the Heisenberg picture. Within a mean-field approximation, the Heisenberg equations of motion,

$$\begin{aligned} i\partial_t \hat{a}_j(t) &= [\hat{a}_j(t), \hat{H}], \\ i\partial_t \hat{c}_j(t) &= [\hat{c}_j(t), \hat{H}], \end{aligned} \tag{2.36}$$

reduce to a matrix equation $i\partial_t X(t) = H(t)X(t)$, where $H(t)$ is a $4N \times 4N$ matrix, and $X(t)$ is a $4N \times 1$ vector that maps fermionic operators at time t to those at $t = 0$,

$$\begin{aligned} &\left(\hat{a}_1(t) \quad \hat{a}_2(t) \quad \dots \quad \hat{a}_N(t) \quad \hat{a}_1^\dagger(t) \quad \dots \quad \hat{a}_N^\dagger(t) \quad \hat{c}_1(t) \quad \dots \quad \hat{c}_N(t) \right)^T \\ &= X(t) \left(\hat{a}_1(0) \quad \dots \quad \hat{a}_N(0) \quad \hat{c}_1(0) \quad \dots \quad \hat{c}_N(0) \right)^T. \end{aligned} \tag{2.37}$$

In a typical numerical experiment we take $N \simeq 50$. The matrix $H(t)$ can be computed from Eq. (2.36). We update X via $X(t + \delta t) = e^{-i\bar{H}\delta t}X(t)$, where \bar{H} is an approximant to the average $H(t)$ in the interval between t and $t + \delta t$. In the coupled-wire case, $H(t)$ depends on $X(t)$ through the self-consistency condition in Eq. (2.5). This self-consistent approach conserves total mean particle number of “a” and “c” atoms, and is a more sophisticated generalization of the random

phase approximation. In the proximity-induced superfluid case, contact with a bath implies $H(t)$ is a constant and the total mean number of “a” and “c” atoms are not conserved.

From $X(t)$, we calculate $\langle \hat{\gamma}_{\text{edge}}^\dagger \hat{\gamma}_{\text{edge}} \rangle$, the probability of the qubit being in the state $|g_+\rangle$. We also calculate coherences between $|g_+\rangle$ and $|g_-\rangle$ through $\langle \hat{\gamma}_{\text{edge}} \rangle$. We quantify the success of our protocols through the fidelity of the final state produced by the gates, defined as the norm of the overlap of the final state $|\psi_f\rangle$ with the intended target state $|\phi\rangle$, $f(|\phi\rangle, |\psi_f\rangle) = |\langle \phi | \psi_f \rangle|$. We express the fidelity in terms of expectation values of edge-state creation and annihilation operators. For example if the intended target state is $|g_+\rangle$, the fidelity is $\sqrt{\langle \psi_f | \hat{\gamma}_{\text{edge}}^\dagger \hat{\gamma}_{\text{edge}} | \psi_f \rangle}$. With these tools we explore algorithms to implement various gates on qubits.

2.8 Quantum Gates

2.8.1 Intermediate Regime: Projective Initialization

We begin by discussing the physics of the intermediate regime $J_c > \Omega > J_c/N$ as this is the most familiar. Here the photon absorption rate is given by Fermi’s golden rule, and Figs. 2.2 and 2.3 can be directly interpreted as the rates of producing “c” atoms. To perform a projective initialization, we use the fact that there are frequencies ω where $\Gamma(|g_+\rangle, \omega) \neq 0$, but $\Gamma(|g_-\rangle, \omega) = 0$. Logically one must be able to deterministically set the qubit into the state $|g_-\rangle$ by shining photons at those frequencies. A similar method can be used to set the qubit into $|g_+\rangle$. By working in the regime $J_c/N < \Omega < J_c$, we ensure that any atoms which exit in the “c” state carry away the information about the initial state of the qubit.

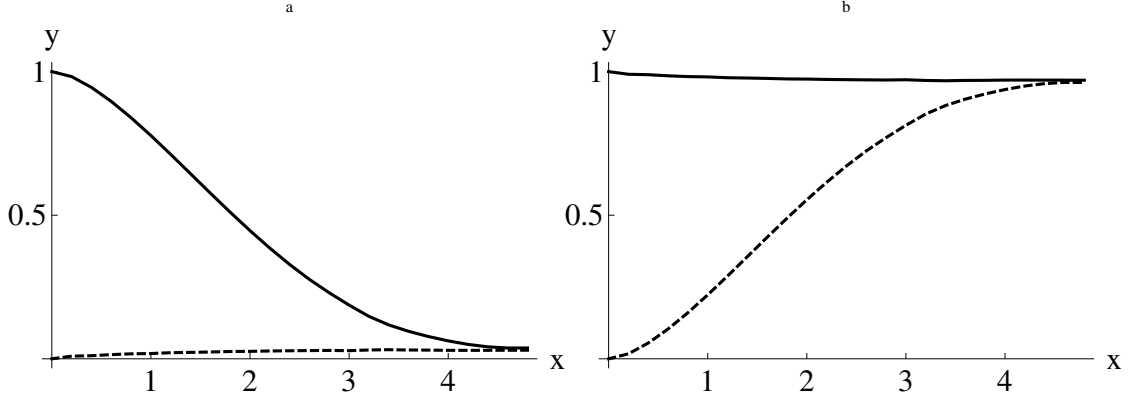


Figure 2.4: Dynamics of $\langle \hat{\gamma}_{\text{edge}}^\dagger \hat{\gamma}_{\text{edge}} \rangle$ during the initialization gate in a geometry where the system consists of a single wire immersed in a superfluid cloud. The wire is in the form of a ring, as explained in Sec. 2.5.1. Electromagnetic waves are shined upon the system, with frequencies (a) $\omega = -\mu_c - 2J_c$ and (b) $\omega = -\mu_c + 2J_c$. The solid curve corresponds to the system's initial state being $|\psi\rangle = |g_+\rangle$, and the dashed curve to $|\psi\rangle = |g_-\rangle$. The fidelities of the initialization gate in the two cases are nearly 100%.

Figure 2.4 shows the dynamics of $\langle \hat{\gamma}_{\text{edge}}^\dagger \hat{\gamma}_{\text{edge}} \rangle$ for the proximity-induced case (i.e., when Δ_j are constant) for two different microwave frequencies and two different initial states $|g_+\rangle$ and $|g_-\rangle$. In Fig. 2.4(a) we choose a frequency where $\Gamma(|g_-\rangle, \omega) = 0$, producing $|g_-\rangle$ as the final state for both initial states, and in Fig. 2.4(b) we choose a frequency where $\Gamma(|g_+\rangle, \omega) = 0$, producing $|g_+\rangle$ as the final state for both initial states. The fidelity of the final state produced in all four cases is nearly 100%.

We find that our algorithm to initialize the qubit does not work in the coupled-wire geometry, where Δ_j are determined self-consistently. Figure 2.5 shows the dynamics of $\langle \hat{\gamma}_{\text{edge}}^\dagger \hat{\gamma}_{\text{edge}} \rangle$ for this case. This failure is due to an induced chemical potential in the wires during photon absorption. We examine this failure in more detail below.

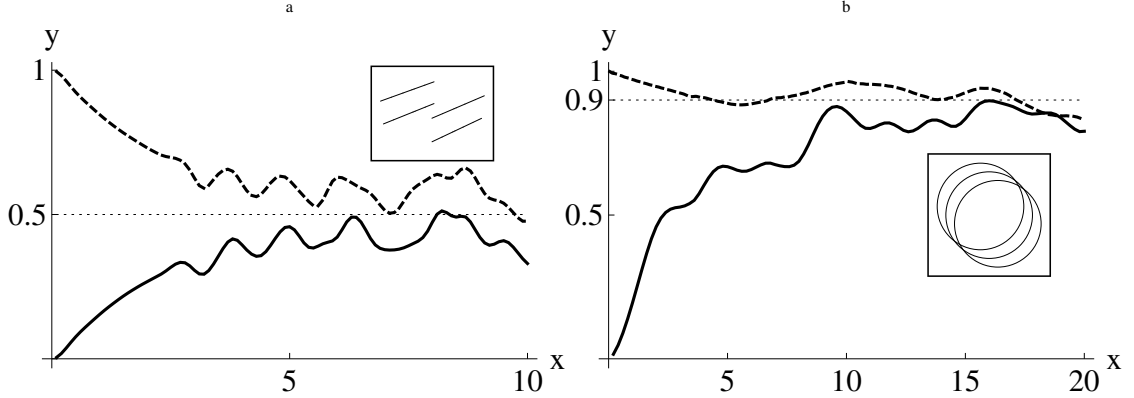


Figure 2.5: Dynamics of $\langle \hat{\gamma}_{\text{edge}} \hat{\gamma}_{\text{edge}}^\dagger \rangle$ during the initialization gate in a geometry of coupled wires or rings. (a) The atoms are trapped in an array of linear wires. Parameters: $\Delta_j = J = 40\Omega$, $J_c = 5\Omega$, $N = 25$, $\omega_0 = -\mu_c$. (b) The atoms are trapped in an array of rings. Parameters: $\Delta_j = J = 20\Omega$, $J_c = 7.5\Omega$, $N = 50$, $\omega_0 = -\mu_c - 2J_c$. Insets show the geometry of trapping. The solid line represents the case where the system is initially in the state $|g_+\rangle$, and the dashed line represents where it is initially in $|g_-\rangle$. A frequency ω_0 where $\Gamma(|g_-\rangle, \omega_0) = 0$ is shined upon the system, with the intention of setting the qubit to $|g_-\rangle$. The square of the fidelity of the final state is roughly 50% in (a) and 90% in (b). In both cases, there is some absorption when the initial state is $|g_-\rangle$ due to finite bandwidth of the “c” atoms. In both cases, this shifts ω to a new frequency where $|g_-\rangle$ is not dark. In case (a) the absorption at this new frequency is significant, while in case (b) the absorption is still small.

Failure of Projective Initialization in Arrays of Coupled Wires

As previously introduced, we consider an array of wires or rings, each initially in the state $|g_+\rangle$. We illuminate the atoms with photons of frequency ω_0 where $\Gamma(|g_+\rangle, \omega_0) \neq 0$, but $\Gamma(|g_-\rangle, \omega_0) = 0$, with the intention of driving all the clouds into $|g_-\rangle$. If this process was successful, it would remove one “a” atom from each wire and hence shift the chemical potential. This resulting shift $\delta\mu$ would be of order J/N , where J is the hopping amplitude of the “a” atoms and N is the number of lattice sites. As detailed in Eq. (2.8), the chemical potential enters into the relationship between the physical electromagnetic frequency ω_{physical} and the frequency ω that appears in Fermi’s golden rule. The condition $\Gamma(|g_-\rangle, \omega) = 0$

will be violated at the new frequency $\omega = \omega_0 - \delta\mu/\hbar$, and the gate instead drives the system into a steady-state mixture of $|g_+\rangle$ and $|g_-\rangle$. As a technical point, we do not have a time-dependent μ in our equations; rather this effect is manifest by a time-dependent phase for Δ_j . Figure 2.5(a) shows a self-consistent mean-field theory calculation of the evolution of $\langle \hat{\gamma}_{\text{edge}}^\dagger \hat{\gamma}_{\text{edge}} \rangle$ when the atoms are trapped in an array of finite wires. It illustrates that the square of the fidelity of the final state is only about 50%.

One might argue that the scaling of $\delta\mu \simeq O(J/N)$ with N implies that the gate will work in the thermodynamic limit. Such an argument is fallacious when the atoms are trapped in a linear geometry. In this case the spacing $\delta\omega$ of the peaks in the absorption spectra scales as $O(J_c/N\hbar)$. In order to have localized edge modes where the edge spectrum is separated from the bulk, one needs $J_c \ll \Delta \simeq J$. Therefore in this geometry, $\delta\mu$ is always large compared to $\hbar\delta\omega$, and the absorption rate in the state $|g_-\rangle$ at the new frequency $\omega = \omega_0 - \delta\mu/\hbar$ is significant. The fidelity is therefore poor.

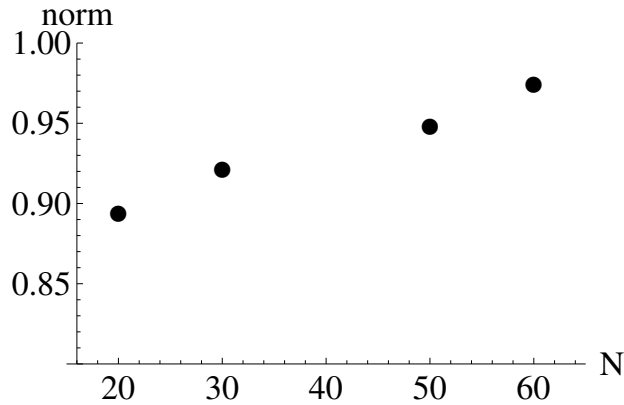


Figure 2.6: Fidelity of the initialization gate for different lengths of superfluid rings. The “a” and “c” atoms are confined in a ring geometry. We used parameters: $\Delta_j = J = 20\Omega$, $J_c = 7.5\Omega$, and $\omega_0 = \mu_c \pm 2J_c$ for desired final states $|\phi\rangle = |g_\pm\rangle$. $|\psi_f\rangle$ denotes the actual final state produced. The initialization gate has higher fidelity for larger lengths N .

Conversely, the initialization gate works in the thermodynamic limit for an array of rings. As shown in Fig. 2.2 for the ring geometry, the change in the spectral weights over a scale of $O(J_c/N)$ is small. Therefore, in this case one can spectroscopically set the qubit with higher fidelity. This success is illustrated in Fig. 2.5(b) for parameters where the square of the fidelity of the final state is roughly 90%. Figure 2.6 illustrates that the fidelity grows as N increases, albeit slowly.

We avoid these difficulties in the rest of this chapter by restricting ourselves to the case of a single wire in proximity to a superfluid cloud. Similar physics can be seen in arrays of coupled wires, but the changing chemical potential will result in smaller fidelities.

2.8.2 Fast and Slow Regimes: Coherent Gate Operations

In this section we explore algorithms to perform a set of gates required for quantum computing: X, Y, H (Hadamard) and C^Y (controlled- Y). It will be convenient to also define a Z gate: $Z = -iXY$. The X, Y, Z , and H gates act on single qubits and are described below. The C^Y gate is a two-qubit gate which will be analyzed in Sec. 2.9.

The X, Y and Z gates perform a rotation of the Bloch sphere by π radians around the x, y and z axes. That is,

$$\begin{aligned}
 X|g_+\rangle &= |g_-\rangle, X|g_-\rangle = |g_+\rangle, \\
 Y|g_+\rangle &= i|g_-\rangle, Y|g_-\rangle = -i|g_+\rangle, \\
 Z|g_+\rangle &= |g_+\rangle, Z|g_-\rangle = -|g_-\rangle.
 \end{aligned}
 \tag{2.38}$$

For our system, these gates can be expressed as $X = \hat{\gamma}_{\text{edge}} + \hat{\gamma}_{\text{edge}}^\dagger$, $Y = i(\hat{\gamma}_{\text{edge}} -$

$\hat{\gamma}_{\text{edge}}^\dagger$), and $Z = \hat{\gamma}_{\text{edge}}^\dagger \hat{\gamma}_{\text{edge}} - \hat{\gamma}_{\text{edge}} \hat{\gamma}_{\text{edge}}^\dagger$. The X and Y gates are related to each other by a gauge transformation of the fermionic creation and annihilation operators. To disambiguate the situation we take $\Delta_j > 0$. It can be observed from Eq. (2.20) that, in this case, the coherence factors $f_0(j)$ are peaked at $j = 1$.

The H gate is

$$\begin{aligned} H|g_+\rangle &= \frac{|g_+\rangle + |g_-\rangle}{\sqrt{2}}, \\ H|g_-\rangle &= \frac{|g_+\rangle - |g_-\rangle}{\sqrt{2}}. \end{aligned} \tag{2.39}$$

It can be expressed in terms of edge mode operators as $H = (\hat{\gamma}_{\text{edge}} + \hat{\gamma}_{\text{edge}}^\dagger + \hat{\gamma}_{\text{edge}}^\dagger \hat{\gamma}_{\text{edge}} - \hat{\gamma}_{\text{edge}} \hat{\gamma}_{\text{edge}}^\dagger)/\sqrt{2}$. The H gate creates superpositions between states of opposite number parity. Since the Hamiltonian modeling our system [Eq. (2.9)] is parity-conserving, it is not possible to implement the H gate using microwaves on these qubits: Any attempt to produce it using microwaves will result in a state with entanglement between the ‘‘a’’ and ‘‘c’’ atoms. We explain how to avoid this in Sec. 2.9, where we propose an architecture in which two logical qubits are encoded in three physical qubits. The logical gates will be made from X, Y , and Z rotations on physical qubits, which we explore below.

X Gate

To implement the X gate on a physical qubit, we illuminate only the left half of the qubit. Experimentally, this can be done by either placing a mask on the right half or by focusing light of short wavelength on the left half of the system, i.e, using Raman techniques with light of wavelength shorter than half the size of the system $\simeq O(\text{mm})$. In the rotating-wave approximation, the term in the Hamiltonian that involves electromagnetic waves [Eq. (2.6)] is now

$$\hat{H}_X = \Omega \sum_{j \leq N/2} \hat{c}_j^\dagger \hat{a}_j + h.c.. \tag{2.40}$$

We can decompose \hat{H}_X as $\hat{H}_X = \hat{H}_X^{\text{res}} + \hat{H}_X^{\text{off-res}}$, where \hat{H}_X^{res} includes terms in which edge modes are resonant with the “c” states, and $\hat{H}_X^{\text{off-res}}$ includes all the other terms which are off-resonant. This can be observed by rewriting \hat{a}_j in terms of quasiparticle operators. Inverting Eq. (2.12) and using the definition of $f_0(j)$, we obtain

$$\begin{aligned} \hat{a}_j = & f_0(j)(\hat{\gamma}_{\text{edge}} + \hat{\gamma}_{\text{edge}}^\dagger) + f_0(N+1-j)(\hat{\gamma}_{\text{edge}} - \hat{\gamma}_{\text{edge}}^\dagger) \\ & + \sum_{\nu \neq 0} (u_\nu(j)\hat{\gamma}_\nu + v_\nu(j)\hat{\gamma}_\nu^\dagger). \end{aligned} \quad (2.41)$$

The terms involving bulk quasiparticles ($\nu \neq 0$) are off-resonant and are included in $\hat{H}_X^{\text{off-res}}$. Further in Eq. (2.40), \hat{c}_j^\dagger can be decomposed into “c” eigenmode creation operators. All the eigenmodes will be excited in the fast regime $\Delta_j \gg \Omega > J_c$, while only one eigenmode will be resonantly coupled in the slow regime $\Omega_c < J_c/N$. Terms in Eq. (2.40) involving modes that are not excited are included in $\hat{H}_X^{\text{off-res}}$. Hereafter, we neglect the off-resonant terms, $\hat{H}_X^{\text{off-res}}$. We explicitly consider the form of \hat{H}_X^{res} in both the slow ($\Omega < J_c/N$) and the fast ($\Omega > J_c$) limits.

As explained above, in the fast regime $\Delta_j \gg \Omega > J_c$,

$$\hat{H}_X^{\text{res}} = \frac{\Omega}{2} \sum_{j \leq N/2} (f_0(j)\hat{c}_j^\dagger X - i f_0(N+1-j)\hat{c}_j^\dagger Y + h.c.), \quad (2.42)$$

where $X = \hat{\gamma}_{\text{edge}} + \hat{\gamma}_{\text{edge}}^\dagger$, $Y = i(\hat{\gamma}_{\text{edge}} - \hat{\gamma}_{\text{edge}}^\dagger)$, and $f_0(j)$ are the coherence factors discussed in Sec. 2.4. Since $f_0(j)$ falls exponentially to zero away from $j = 1$, the coefficients of Y are small and can be ignored. We define $\hat{c}^\dagger = \frac{\sum_{j \leq N/2} f_0(j)\hat{c}_j^\dagger}{\sum_{j \leq N/2} |f_0(j)|^2}$ and $\tilde{\Omega} = \Omega \sum_{j \leq N/2} |f_0(j)|^2$ to produce

$$\hat{H}_X^{\text{res}} = \frac{\tilde{\Omega}}{2} (\hat{c}^\dagger - \hat{c})X. \quad (2.43)$$

For short times $t \ll \hbar/J_c$, one can ignore the dynamics of “c” atoms. The state of the qubit at time t is

$$|\psi(t)\rangle = \left(\cos \frac{\tilde{\Omega}t}{2\hbar} + \sin \frac{\tilde{\Omega}t}{2\hbar} \frac{\hat{c} - \hat{c}^\dagger}{i} X \right) |\psi(0)\rangle + O(J_c t/\hbar). \quad (2.44)$$

The X gate is implemented by shining a π pulse lasting $T = \frac{\pi\hbar}{\Omega}$. The pulse also excites or deexcites a “c” atom, but, as explained in Sec. 2.6, these “c” atoms do not play any role in future dynamics. The dynamics of $\langle \hat{\gamma}_{\text{edge}}^\dagger \hat{\gamma}_{\text{edge}} \rangle$ and $\langle \hat{\gamma}_{\text{edge}} \rangle$ for a π pulse are illustrated in Figs. 2.7(a) and 2.7(b) for an initial state $\frac{|g_+\rangle + |g_-\rangle}{\sqrt{2}}$, which is an eigenstate of X . The average occupation of the edge mode, $\langle \hat{\gamma}_{\text{edge}}^\dagger \hat{\gamma}_{\text{edge}} \rangle$, does not change, indicating that the probability of the qubit being in $|g_+\rangle$ remains 50% throughout the pulse. The coherence $\langle \hat{\gamma}_{\text{edge}} \rangle$ also remains constant, indicating that the phase between $|g_+\rangle$ and $|g_-\rangle$ remains zero.

In the slow regime $\Omega < J_c/N$, the Majorana modes only resonantly couple to one eigenmode of the “c” state. This eigenmode is a momentum state in translationally invariant geometries. In this regime,

$$\hat{H}_X^{\text{res}} = \frac{\Omega}{2} \left((\alpha_k \hat{c}_k^\dagger - \alpha_k^* \hat{c}_k) X + i(\beta_k \hat{c}_k^\dagger + \beta_k^* \hat{c}_k) Y \right). \quad (2.45)$$

where k labels the spectrally selected mode, $\alpha_k = \frac{1}{2} \sum_{j \leq N/2} f_0(j) \psi_k(j)$, $\beta_k = \frac{1}{2} \sum_{j \leq N/2} f_0(N+1-j) \psi_k(j)$, and ψ_k is the wave function of the “c” mode discussed in Sec. 2.5. As before we neglect the coefficients of Y and arrive at a similar expression

$$|\psi(t)\rangle = \left(\cos \frac{|\alpha_k| \Omega t}{2\hbar} + \sin \frac{|\alpha_k| \Omega t}{2\hbar} \frac{\alpha_k^* \hat{c}_k - \alpha_k \hat{c}_k^\dagger}{i} X \right) |\psi(0)\rangle. \quad (2.46)$$

The X gate is implemented by shining a π pulse lasting $T = \frac{\pi\hbar}{|\alpha_k|\Omega}$.

Y Gate

To implement the Y gate we illuminate only the right half of the system. The term in the Hamiltonian that involves electromagnetic waves [Eq. (2.6)] is replaced with

$$\hat{H}_Y = \Omega \sum_{j > N/2} \hat{c}_j^\dagger \hat{a}_j e^{-i\omega t} + h.c. \quad (2.47)$$

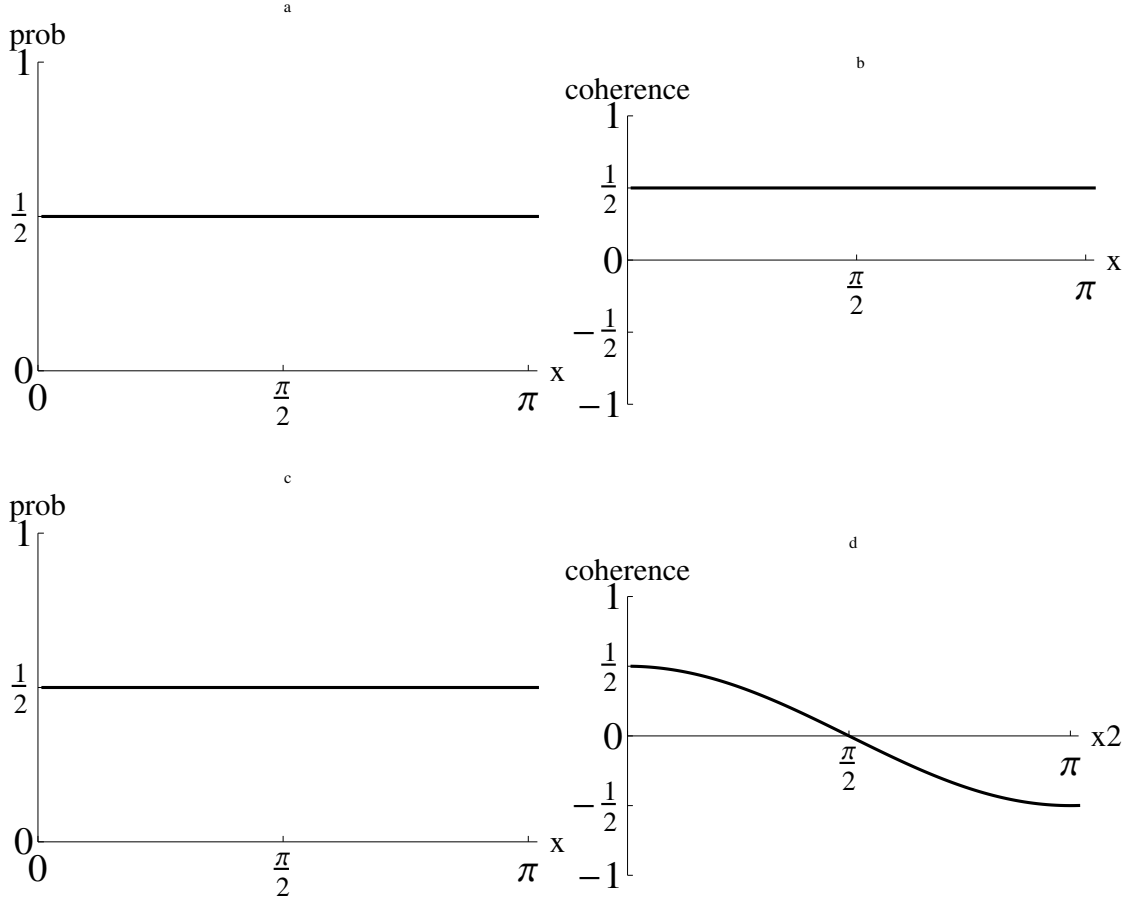


Figure 2.7: Dynamics of $\langle \hat{\gamma}_{\text{edge}}^\dagger \hat{\gamma}_{\text{edge}} \rangle$ and $\langle \hat{\gamma}_{\text{edge}} \rangle$ during the X and Y gates. The parameters used are $\Delta = J = 80\Omega$, $\mu = 0$, $J_c = 0$, $\omega = -\mu_c$, and the system is initialized to $\frac{1}{\sqrt{2}}(|g_+\rangle + |g_-\rangle)$. Panels (a) and (b) illustrate the dynamics in the case of an X gate operation and show that the final state is $\frac{1}{\sqrt{2}}(|g_+\rangle + |g_-\rangle)$. Panels (c) and (d) illustrate the dynamics in the case of a Y gate operation and show that the final state is $\frac{i}{\sqrt{2}}(|g_+\rangle - |g_-\rangle)$.

Neglecting off-resonant terms and exponentially small terms, Eq. (2.47) reduces to

$$\hat{H}_Y^{\text{fast}} = \frac{i\tilde{\Omega}}{2}(\hat{c}^\dagger + \hat{c})Y \quad (2.48)$$

in the fast regime, and to

$$\hat{H}_Y^{\text{slow}} = \frac{i\Omega}{2}(\beta_k^* \hat{c}_k + \beta_k \hat{c}_k^\dagger)Y \quad (2.49)$$

in the slow regime. Here $\tilde{\Omega}$, \hat{c} and β_k have the same meaning as in Sec. 2.8.2. The Y gate is implemented by shining a π pulse lasting $T = \frac{\pi\hbar}{\Omega}$ in the fast regime and

$T = \frac{\pi\hbar}{|\beta_k|\Omega}$ in the slow regime. The dynamics of $\langle \hat{\gamma}_{\text{edge}}^\dagger \hat{\gamma}_{\text{edge}} \rangle$ and $\langle \hat{\gamma}_{\text{edge}} \rangle$ for such a π pulse in the fast regime are illustrated in Figs. 2.7(c) and 2.7(d). Here we see a π phase introduced in the coherence between $|g_+\rangle$ and $|g_-\rangle$.

2.8.3 Z Gate

The $Z = -iXY$ gate can be implemented by illuminating a π pulse on the right half, followed by a π pulse on the left half.

2.9 Two Logical Qubits Composed Of Three Physical Qubits

As explained in Sec. 2.8, it is impossible to implement the H gate on individual physical qubits as our approach cannot create superpositions of states with odd and even numbers of particles. This motivates us to consider a more sophisticated architecture where we construct n logical qubits from $n + 1$ physical qubits. Alternatively, one could encode each logical qubit in a pair of physical qubits (for example, [170]), but our encoding is more compact. In this section, we focus on the case $n = 2$. We define our construction, and propose algorithms to produce all the quantum gates required for universal quantum computation. In Sec. 2.9.4 we discuss the generalization to arbitrary n .

2.9.1 Construction of Logical Qubits

We consider a 1D cloud of “a” atoms broken by a set of potential barriers into three segments, each of length N . We envision using spin-dependent potentials so that the barriers are invisible to atoms in the “c” state. Each segment of “a” atoms has a pair of Majorana edge modes. We label the three clouds as p_1, p_2 , and p_3 and denote the positions of their edges by r_1 and r'_1 , r_2 and r'_2 , and r_3 and r'_3 . We use the construction in Sec. 2.4 to uniquely define fermionic modes $\hat{\gamma}_1^\dagger, \hat{\gamma}_2^\dagger$, and $\hat{\gamma}_3^\dagger$ from the edge modes localized at r_1 and r'_1 , r_2 and r'_2 , and r_3 and r'_3 .

The ground-state manifold of this system is eight-fold degenerate, $|g_{\pm\pm\pm}\rangle$. We define $|g_{---}\rangle$ as the vacuum of quasiparticles: $\hat{\gamma}_1|g_{---}\rangle = \hat{\gamma}_2|g_{---}\rangle = \hat{\gamma}_3|g_{---}\rangle = 0$ and define the other ground states as $|g_{\sigma\sigma'\sigma''}\rangle = \left(\hat{\gamma}_1^\dagger\right)^{\frac{1+\sigma}{2}} \left(\hat{\gamma}_2^\dagger\right)^{\frac{1+\sigma'}{2}} \left(\hat{\gamma}_3^\dagger\right)^{\frac{1+\sigma''}{2}} |g_{---}\rangle$, where $\sigma, \sigma', \sigma'' = \pm$. For example, $|g_{+++}\rangle = \hat{\gamma}_1^\dagger \hat{\gamma}_2^\dagger \hat{\gamma}_3^\dagger |g_{---}\rangle$. We will use the notations $|g_{\sigma\sigma'\sigma''}\rangle$ and $|g_\sigma\rangle \otimes |g_{\sigma'}\rangle \otimes |g_{\sigma''}\rangle$ interchangeably, where \otimes is the Cartesian product.

Of the eightfold degenerate states, four have the same parity. We construct two logical qubits from these four states and assign them the labels:

$$\begin{aligned}
 |--\rangle &\equiv |g_{--+}\rangle = \hat{\gamma}_3^\dagger |g_{---}\rangle \\
 |-+\rangle &\equiv |g_{-+-}\rangle = \hat{\gamma}_2^\dagger |g_{---}\rangle \\
 |+-\rangle &\equiv |g_{+--}\rangle = \hat{\gamma}_1^\dagger |g_{---}\rangle \\
 |++\rangle &\equiv |g_{+++}\rangle = \hat{\gamma}_1^\dagger \hat{\gamma}_2^\dagger \hat{\gamma}_3^\dagger |g_{---}\rangle.
 \end{aligned} \tag{2.50}$$

We denote the logical qubits by l_1 and l_2 . We call p_1 and p_2 the representational bits as their states are identical to those of the logical qubits l_1 and l_2 . The ancillary bit p_3 serves the purpose of maintaining the total parity.

To spectroscopically measure and perform gate operations on the logical qubit,

we electromagnetically excite the atoms from the “a” state to the “c” state. We find that we can measure the state of the qubits and implement the initialization, X , Y , and Z gates on the logical qubits by addressing each physical qubit separately as outlined in Secs. 2.5 and 2.8. To implement the Hadamard and two-qubit gates, we address two physical qubits simultaneously. In the following, we let X_1 denote the X gate on the physical qubit p_1 and X_1^{logical} denote the X gate on the logical qubit l_1 . We use similar notations for the other gates. Below we describe the logical gates.

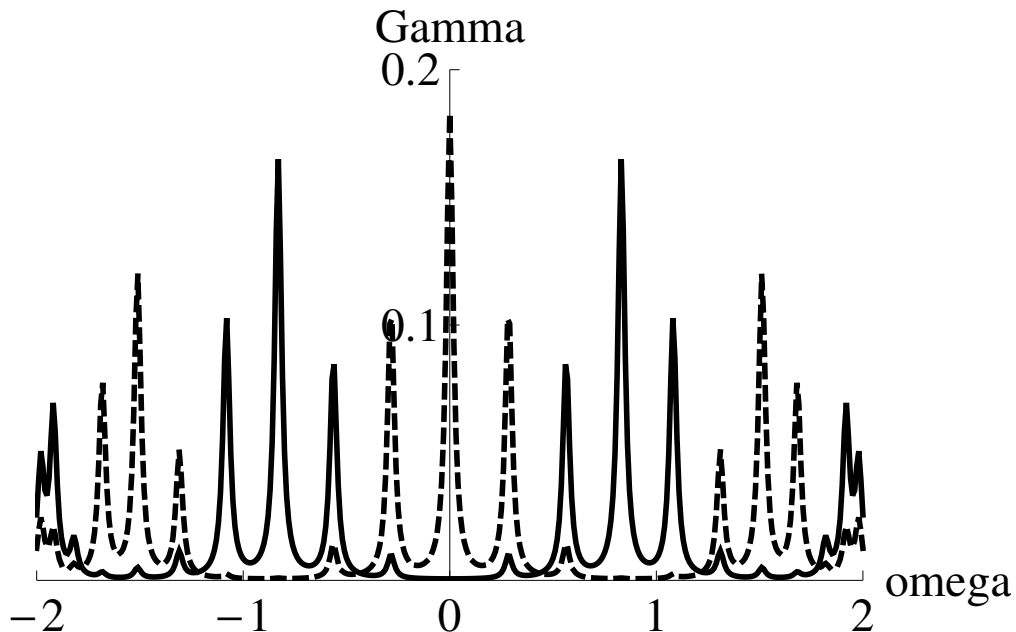


Figure 2.8: Absorption spectrum of physical qubit p_1 trapped in a linear geometry, where barriers create three physical qubits from one wire. Parameters used: $\Delta_j = J, \mu = 0, N = 7$. The solid curve corresponds to the spectrum of $|g_+\rangle$, and the dashed curve to the spectrum of $|g_-\rangle$.

2.9.2 Measurement and Initialization

As mentioned earlier, the states of the logical qubits l_1 and l_2 coincide with the states of physical qubits p_1 and p_2 . The spectra of each physical qubit are given

by expressions derived in Sec. 2.5. These spectra are plotted in Fig. 2.8. Since the cloud of “c” atoms is three times as long as the segment corresponding to a physical qubit, the spectra contain sets of three peaks interdigitated among each other.

Projective initialization of the two logical qubits can be achieved by three single-photon transitions, one for each physical qubit. For example, to set the logical qubits in the state $|++\rangle$, we initialize each physical qubit in the state $|g_+\rangle$. To achieve this we illuminate each wire separately at the frequencies which drive the qubits into the desired state.

2.9.3 Coherent Single Qubit Operations

We implement coherent single-qubit gates by a series of microwave pulses on individual physical qubits. One complication is that each microwave pulse not only flips a qubit, but can also add an undesired phase determined by the other qubits. This phase is a result of fermionic commutation relations. For illustration, we consider the action of the operator $\hat{\gamma}_2 + \hat{\gamma}_2^\dagger$ (which is the relevant operator when the left half of p_2 is illuminated, and would naively be expected to give the X_2 gate):

$$\begin{aligned} (\hat{\gamma}_2 + \hat{\gamma}_2^\dagger)|g_{-\sigma}\rangle &= |g_{-\sigma}\rangle = -Z_1 X_2 |g_{-\sigma}\rangle, \\ (\hat{\gamma}_2 + \hat{\gamma}_2^\dagger)|g_{+\sigma}\rangle &= -|g_{+\sigma}\rangle = -Z_1 X_2 |g_{+\sigma}\rangle. \end{aligned} \tag{2.51}$$

This operation yields $-Z_1 X_2$ instead of the intended gate X_2 . In the generic case, the result of a rotation $(z_i \hat{\gamma}_i + z_i^* \hat{\gamma}_i^\dagger)$ on a state $\otimes_{j=1}^3 |g_{\sigma_j}\rangle$ is

$$(z_i \hat{\gamma}_i + z_i^* \hat{\gamma}_i^\dagger) (\otimes_{j=1}^3 |g_{\sigma_j}\rangle) = (\otimes_{j<i} -Z_j |g_{\sigma_j}\rangle) \otimes \left((z_i \hat{\gamma}_i + z_i^* \hat{\gamma}_i^\dagger) |g_{\sigma_i}\rangle \right) \otimes (\otimes_{j>i} |g_{\sigma_j}\rangle) \tag{2.52}$$

The sequence of $-Z$ gates above can be thought of as a Jordan-Wigner transformation. As explicitly shown below, a simple sequence of pulses can remove these unwanted phases for the X, Y and Z gates.

Incorporating pulses to remove unwanted phases, we find

$$\begin{aligned}
X_1^{\text{logical}} &= X_1 X_3 \\
&= (\hat{\gamma}_1 - \hat{\gamma}_1^\dagger)(\hat{\gamma}_2 + \hat{\gamma}_2^\dagger)(\hat{\gamma}_2 - \hat{\gamma}_2^\dagger)(\hat{\gamma}_3 + \hat{\gamma}_3^\dagger), \\
Y_1^{\text{logical}} &= Y_1 X_3 \\
&= (\hat{\gamma}_1 + \hat{\gamma}_1^\dagger)(\hat{\gamma}_2 + \hat{\gamma}_2^\dagger)(\hat{\gamma}_2 - \hat{\gamma}_2^\dagger)(\hat{\gamma}_3 + \hat{\gamma}_3^\dagger), \\
X_2^{\text{logical}} &= X_2 X_3 \\
&= (\hat{\gamma}_2 - \hat{\gamma}_2^\dagger)(\hat{\gamma}_3 + \hat{\gamma}_3^\dagger), \\
Y_2^{\text{logical}} &= Y_2 X_3 \\
&= (\hat{\gamma}_2 + \hat{\gamma}_2^\dagger)(\hat{\gamma}_3 + \hat{\gamma}_3^\dagger).
\end{aligned} \tag{2.53}$$

As in Sec. 2.8, each operator in parentheses corresponds to illuminating one part of one segment. As before, $Z_i^{\text{logical}} = -iX_i^{\text{logical}}Y_i^{\text{logical}}$.

The logical Hadamard gate, H_i^{logical} , requires two-qubit operations (one representational bit and one ancillary bit) and is discussed in Sec. 2.9.4 along with the C^Y gate.

2.9.4 Two-Qubit Operations

We achieve two-qubit operations on physical qubits p_i and p_j by simultaneously illuminating p_i and p_j with a microwave coupling strength $\Omega < J_c/N$. To achieve different rotations in the ground-state manifold, we focus microwave pulses of different frequencies, durations and spatial distributions. For concreteness, we consider the rotation given by $\hat{\gamma}_1 + \hat{\gamma}_1^\dagger + \hat{\gamma}_2 + \hat{\gamma}_2^\dagger$. To achieve this, we illuminate the

left half of p_1 and p_2 simultaneously. Labeling the “c” eigenstate being excited by k , the Hamiltonian governing the excitation to that mode has the form

$$\begin{aligned} \hat{H}_{2\text{qubit}}^{\text{res}} = & \sum_{0 \leq j < N/2} f_1(r_1 + j) \psi_k(r_1 + j) \hat{c}_k^\dagger \frac{\hat{\gamma}_1 + \hat{\gamma}_1^\dagger}{2} + f_2(r_2 + j) \psi_k(r_2 + j) \hat{c}_k^\dagger \frac{\hat{\gamma}_2 + \hat{\gamma}_2^\dagger}{2} \\ & + f_1(r_1' - j) \psi_k(r_1' - j) \times \hat{c}_k^\dagger \frac{\hat{\gamma}_1 - \hat{\gamma}_1^\dagger}{2} + f_2(r_2' - j) \psi_k(r_2' - j) \hat{c}_k^\dagger \frac{\hat{\gamma}_2 - \hat{\gamma}_2^\dagger}{2} + h.c \end{aligned} \quad (2.54)$$

Since $f_1(r_1 + j)$ and $f_2(r_2 + j)$ exponentially decay away from $j = 0$, we neglect the coefficients of $\hat{\gamma}_1 - \hat{\gamma}_1^\dagger$ and $\hat{\gamma}_2 - \hat{\gamma}_2^\dagger$. We find that the microwave frequency should be chosen such that $\sum_{0 \leq j < N/2} f_1(r_1 + j) \psi_k(r_1 + j) = \sum_{0 \leq j < N/2} f_2(r_2 + j) \psi_k(r_2 + j)$ whose value we denote by α_k . In that case, Eq. (2.54) reduces to

$$\hat{H}_{2\text{qubit}}^{\text{res}} = \Omega \frac{\alpha_k \hat{c}_k^\dagger - \alpha_k^* \hat{c}_k}{2} \left(\hat{\gamma}_1 + \hat{\gamma}_1^\dagger + \hat{\gamma}_2 + \hat{\gamma}_2^\dagger \right). \quad (2.55)$$

A π pulse lasting $T = \frac{\pi \hbar}{|\alpha_k| \Omega}$ performs the intended operation $\hat{\gamma}_1 + \hat{\gamma}_1^\dagger + \hat{\gamma}_2 + \hat{\gamma}_2^\dagger$. Other rotations in the ground-state manifold can be produced by choosing the frequency, duration, and spatial distribution of the microwave pulse appropriately.

Below we provide explicit algorithms to perform the H_i^{logical} and C^Y gates. We first introduce two operations that will be useful building blocks and construct the H_i^{logical} and C^Y gates out of these building blocks. In Sec. 2.9.4, we consider the action of generic rotations on the qubits and the problems encountered in generic rotations.

Gates Involving Two-Qubit Operations

The first operation we consider, denoted by H_{ij} , consists of two steps which perform the rotation $(\hat{\gamma}_i^\dagger + \hat{\gamma}_i + \hat{\gamma}_j^\dagger + \hat{\gamma}_j)(\hat{\gamma}_i - \hat{\gamma}_i^\dagger)$. The second operation we introduce also consists of two steps: $S_{ij} = (\hat{\gamma}_i + \hat{\gamma}_i^\dagger + \hat{\gamma}_j + \hat{\gamma}_j^\dagger)(\hat{\gamma}_i - \hat{\gamma}_i^\dagger + \hat{\gamma}_j - \hat{\gamma}_j^\dagger)$. We construct H_i^{logical} and C^Y gates out of H_{ij} , S_{ij} and single-qubit gates.

In terms of these building blocks,

$$\begin{aligned}
H_2^{\text{logical}} &= H_{23}, \\
C_{12}^Y &= Z_1 Z_2 S_{23}, \\
C_{21}^Y &= Z_1 S_{12} S_{23} S_{12}, \text{ and} \\
H_1^{\text{logical}} &= C_{21}^Y S_{13}.
\end{aligned}
\tag{2.56}$$

Entanglement in Two-Qubit Operations

In this section we explore generic two-qubit operations that can be performed by microwave pulses on pairs of qubits. The H_{ij} and S_{ij} operations introduced earlier are special cases.

The term in the Hamiltonian [Eq. (2.6)] which resonantly couples the Majorana mode to a “c” eigenstate labeled by k has the form

$$\hat{H}^{\text{res}} = \Omega(\hat{c}_k^\dagger \hat{h}_{ij} + \hat{h}_{ij}^\dagger \hat{c}_k),
\tag{2.57}$$

where \hat{h}_{ij} consists of edge mode operators. The most generic h_{ij} is Hermitian; i.e, it has the form:

$$\hat{h}_{ij} = z_i \hat{\gamma}_i + z_i^* \hat{\gamma}_i^\dagger + z_j \hat{\gamma}_j + z_j^* \hat{\gamma}_j^\dagger.
\tag{2.58}$$

This can be derived as follows. In order for the “c” atoms to disentangle from the rotation performed on the qubits, \hat{h}_{ij} has to satisfy $\hat{h}_{ij}^\dagger = e^{i\phi} \hat{h}_{ij}$ where ϕ is an arbitrary phase. By absorbing this phase into the “c” operators, we arrive at the form in Eq. (2.58).

We illustrate that \hat{h}_{ij} leads to different physical consequences when acting upon neighboring qubits or distantly spaced qubits. If the segments i and $j = i + 1$ are neighbors, the result of the generic pulse in Eq. (2.58) only involves the physical

qubits on those sites, and

$$\hat{h}_{i,i+1}|g_{\sigma_i\sigma_{i+1}}\rangle = \left(z_i\hat{\gamma}_i + z_i^*\hat{\gamma}_i^\dagger|g_{\sigma_i}\rangle\right)\otimes|g_{\sigma_{i+1}}\rangle + (-1)^{\frac{1+\sigma_i}{2}}|g_{\sigma_i}\rangle\otimes\left(z_{i+1}\hat{\gamma}_{i+1} + z_{i+1}^*\hat{\gamma}_{i+1}^\dagger|g_{\sigma_{i+1}}\rangle\right), \quad (2.59)$$

where $\sigma_i, \sigma_{i+1} = \pm$. If instead the segments are further spaced, the action of the pulse involves all intervening qubits. For example, if they are separated by one segment (which is the largest separation allowed for three physical qubits),

$$\begin{aligned} \hat{h}_{i,i+2}|g_{\sigma_i\sigma_{i+1}\sigma_{i+2}}\rangle &= \left(z_i\hat{\gamma}_i + z_i^*\hat{\gamma}_i^\dagger|g_{\sigma_i}\rangle\right)\otimes|g_{\sigma_{i+1},\sigma_{i+2}}\rangle + (-1)^{\frac{2+\sigma_i+\sigma_{i+1}}{2}}|g_{\sigma_i,\sigma_{i+1}}\rangle \\ &\otimes\left(z_{i+2}\hat{\gamma}_{i+2} + z_{i+2}^*\hat{\gamma}_{i+2}^\dagger|g_{\sigma_{i+2}}\rangle\right). \end{aligned} \quad (2.60)$$

The generalization to longer chains is straightforward.

The extra phases produced when h_{ij} acts on nonadjacent qubits are the reason why the implementation of H_1^{logical} and C_Y^{21} in Sec. 2.9.4 were so much more complicated than H_2^{logical} and C_Y^{12} . Due to these phases, extending our proposal to more than two logical qubits is non-trivial. However we see no impediment to constructing generic gates for chains of N qubits for arbitrary N .

2.10 Summary

In summary, we have presented an experimentally feasible method to perform quantum computing with Majorana fermions in cold gases using microwaves. We considered two geometries which give rise to Majorana fermion excitations: a 2D array of coupled 1D wires, and a single 1D wire embedded in a superfluid cloud. We proposed various methods to generate nearest-neighbor interactions between atoms in the coupled wires, which is crucial to creating Majorana fermions. We modeled these systems with a mean-field theory and studied their single-particle excitation spectra. We observed that the systems supported Majorana modes for

a certain range of parameters, and that in this “topologically non-trivial phase”, the ground state is doubly degenerate. These two degenerate states can be used as a qubit. We calculated the absorption spectra, and showed that the lineshape gives evidence of Majorana fermions and can be used to measure the state of the qubit. We further showed that absorption of a photon flips between the degenerate states. We proposed that this feature could be used to perform quantum gates on the qubit. We found the geometries for which this protocol works. We presented algorithms to perform certain quantum gates on individual physical qubits. We constructed logical qubits out of physical qubits and gave generic arguments to perform rotations of the qubits. In addition to these arguments, we gave explicit pulse sequences for constructing a universal set of quantum gates for two logical qubits encoded in three physical qubits, hence allowing our system to be used for universal quantum computation.

ACKNOWLEDGMENT

We thank Matthew Reichl for useful discussions. We thank Prof. Mukund Ven- galattore for carefully checking for numerical errors. This work is supported by the National Science Foundation Grant no. PHY-1068165 and a grant from the Army Research Office with funding from the DARPA OLE program.

CHAPTER 3

LATTICE BOSONS WITH INFINITE RANGE INTERACTIONS

MANY-BODY PHYSICS USING COLD ATOMS

Bhuvanesh Sundar, Ph.D.

Cornell University 2016

Motivated by experiments performed by Landig *et al.* [Nature (London) **532**, 476 (2016)], we consider a two-dimensional Bose gas in an optical lattice, trapped inside a single mode superradiant Fabry-Perot cavity. The cavity mediates infinite-range checkerboard interactions between the atoms, which produces competition between Mott insulator, charge-density wave, superfluid, and supersolid phases. We calculate the phase diagram of this Bose gas in a homogeneous system and in the presence of a harmonic trap. The work in this chapter was done in collaboration with Prof. Erich Mueller. This chapter is adapted from a peer-reviewed article, Physical Review A **94**, 033631 (2016), which was co-authored with Prof. Erich Mueller.

3.1 Introduction

Introducing long-range interactions between bosonic atoms in an optical lattice provides the opportunity to explore different phases, driven by the competition between short-range interactions, long-range interactions, and quantum tunneling. Interactions mediated via an optical cavity provide an avenue to explore this physics [86, 80]. In this study, we calculate the phase diagram of bosonic atoms experiencing such cavity-mediated long-range interactions. We find a rich phase diagram with superfluid (SF), supersolid (SS), Mott insulator (MI), and charge-density wave (CDW) phases. We find a breakdown of the local-density approximation (LDA), and good agreement with experiments [86].

By trapping ^{87}Rb atoms in a transversely pumped single mode optical cavity and tuning the cavity into the superradiant phase, Landig *et al.* have produced infinite-range interactions between bosonic atoms [86]. Interference between the pump beam and the light scattered into the cavity results in a checkerboard intensity pattern, whose strength is proportional to the number of atoms on the high intensity sites. Integrating out the photons yields a long-range checkerboard interaction. By changing the lattice depth and the cavity detuning, the experimentalists can independently tune the strengths of the short-range and long-range atomic interactions relative to the tunneling strength. Adding these long-range interactions to a Bose-Hubbard model, we use a variational ansatz to produce a phase diagram. We consider both a homogeneous and a harmonically trapped system. In addition to SF order, characterized by off-diagonal long-range order in the single-particle density matrix, the system can also display CDW order, where the occupations on the even and odd sites differ. Coexistence of both orders results in a SS, and the absence of both orders a MI. All four of these phases are found

in our calculations, and were seen in experiments as well [86]. We predict that a reanalysis of existing experimental data will reveal previously undetected phase transitions. Some of our results for homogeneous systems have been seen in other theoretical studies [36, 22, 94, 124].

This chapter is organized as follows. In Sec. 3.2, we introduce our model for a homogeneous Bose gas, and present the phase diagram. In Sec. 6.4, we analyze the harmonically trapped case. We conclude in Sec. 6.6.

3.2 Homogeneous gas

In this section, we explore the phase diagram of a homogeneous Bose gas in an optical lattice, trapped inside a single mode optical cavity. We calculate the ground state of the bosons by minimizing the energy of a variational many-body wave function. We obtain the phase boundaries through a combination of numerical and analytical means. This section is organized as follows. In Sec. 3.2.1, we introduce our model for a homogeneous Bose gas in an optical lattice, including cavity-mediated infinite-range interactions. In Sec. 3.2.2, we introduce our variational ansatz and calculate the energy of the system. In Sec. 3.2.3, we present the phase diagram of our model.

3.2.1 Model

We consider an ultracold gas of bosons tightly confined to the x - y plane, where they experience a 2D optical lattice. The atoms are coupled to the fundamental mode of a high finesse Fabry-Perot cavity oriented along the x direction, and illuminated by

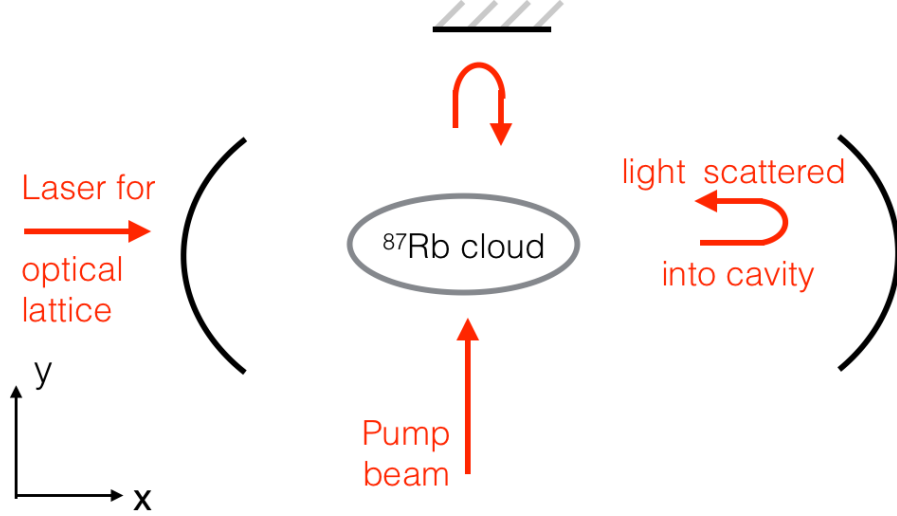


Figure 3.1: Schematic of the experimental setup. A trapped cloud of bosonic ^{87}Rb atoms sits in an off-resonant optical cavity. The atoms are pumped from the side, and scatter light into the cavity. A second laser enters the cavity along its axis, producing an optical lattice.

a pump beam along the y direction (see Fig. 3.1). The pump light scattered by the atoms into the cavity mediates an effective infinite-range atom-atom interaction. The effective atom-atom interactions are derived in [99], producing a Hamiltonian

$$\hat{H} = \hat{H}_{\text{lat}} + \hat{H}_{\text{cav}}. \quad (3.1)$$

The term \hat{H}_{lat} models the trap, tunneling of atoms, and on-site interactions in the two-dimensional optical lattice:

$$\hat{H}_{\text{lat}} = \sum_{\langle ij \rangle} -J \hat{c}_i^\dagger \hat{c}_j + \text{H.c.} + \sum_i \frac{U}{2} \hat{c}_i^\dagger \hat{c}_i^\dagger \hat{c}_i \hat{c}_i - \mu_i \hat{c}_i^\dagger \hat{c}_i. \quad (3.2)$$

The operator \hat{c}_i^\dagger (\hat{c}_i) creates (annihilates) a boson at lattice site i . The hopping strength J can be tuned by controlling the intensity of the laser creating the optical lattice. The on-site interaction strength U can be controlled via the laser intensity and the transverse confinement, or by tuning the magnetic field near a Feshbach resonance. The last term in Eq. (3.2) models the trap, where μ_i is an

effective spatially dependent chemical potential,

$$\mu_i = \mu - \frac{1}{2}m\omega^2 (x_i^2 + y_i^2), \quad (3.3)$$

where x_i and y_i denote the co-ordinates of lattice site i in integer multiples of the lattice constant. For a homogeneous gas, we set $\omega = 0$.

The term \hat{H}_{cav} models the infinite-range interactions mediated by the light in the Fabry-Perot cavity,

$$\hat{H}_{\text{cav}} = -\frac{U'}{K} \left(\sum_i (-1)^{x_i+y_i} \hat{c}_i^\dagger \hat{c}_i \right)^2, \quad (3.4)$$

where K is the total number of lattice sites. The effective long-range interaction strength U' is related to experimental parameters as

$$U' \simeq -K \frac{\hbar\eta^2}{\Delta_c} \quad (3.5)$$

where η is the two-photon Rabi frequency, and Δ_c is the detuning of the optical lattice laser from the fundamental mode of the Fabry-Perot cavity [99]. In this study, we only work in a regime where $U' > 0$. When at fixed density, the long-range interaction energy scales as K^2 , while all other energies scale as K . Thus, to achieve a reasonable thermodynamic limit, we fix U' while $K \rightarrow \infty$.

3.2.2 Gutzwiller ansatz

The model in Eq. (3.1) breaks the symmetry between two kinds of sites: those for which $x_i + y_i$ is even (which we call even sites), and for which $x_i + y_i$ is odd (which we call odd sites). We make a variational ansatz which includes this asymmetry:

$$|\psi\rangle = \left(\sum_{i \in \text{even}} \sum_{n=0}^{\infty} \frac{a_n}{\sqrt{n!}} (\hat{c}_i^\dagger)^n \right) \left(\sum_{j \in \text{odd}} \sum_{n=0}^{\infty} \frac{b_n}{\sqrt{n!}} (\hat{c}_j^\dagger)^n \right) |0\rangle, \quad (3.6)$$

where $|0\rangle$ is the vacuum of atoms. Our ansatz in Eq. (3.6) is an extension of the Gutzwiller ansatz for the Bose-Hubbard model [47, 69]. Normalization dictates that $\sum_{n=0}^{\infty} |a_n|^2 = \sum_{n=0}^{\infty} |b_n|^2 = 1$. The average energy of our variational wavefunction is

$$E_{\text{var}} = K \left(-zJ \left(\sum_n \sqrt{n} a_n a_{n+1} \right) \left(\sum_n \sqrt{n} b_n b_{n+1} \right) + \sum_n \left(\frac{U}{4} n(n-1) - \frac{\mu}{2} n \right) (|a_n|^2 + |b_n|^2) - \frac{U'}{4} \left(\sum_n n (|a_n|^2 - |b_n|^2) \right)^2 \right), \quad (3.7)$$

where z is the number of nearest neighbors to a lattice site. In our case of a two-dimensional square lattice, $z = 4$.

3.2.3 Phase diagram

$$J = 0$$

In the case of a deep optical lattice ($J = 0$), the variational wavefunction which minimizes the energy describes an insulator with parameters

$$\begin{aligned} a_n &= \delta_{n,n_e}, \\ b_n &= \delta_{n,n_o}. \end{aligned} \quad (3.8)$$

Here, $\delta_{m,n}$ is the Kronecker δ , and n_e and n_o are integers obtained by minimizing the energy in Eq. (3.7). If $n_e = n_o$, the ground state is a Mott insulator (MI). If $n_e \neq n_o$, the ground state is a charge-density wave insulator (CDW). The phase diagram for $J = 0$ is plotted in Fig. 3.2. All the phase transitions in this phase diagram are of first order.

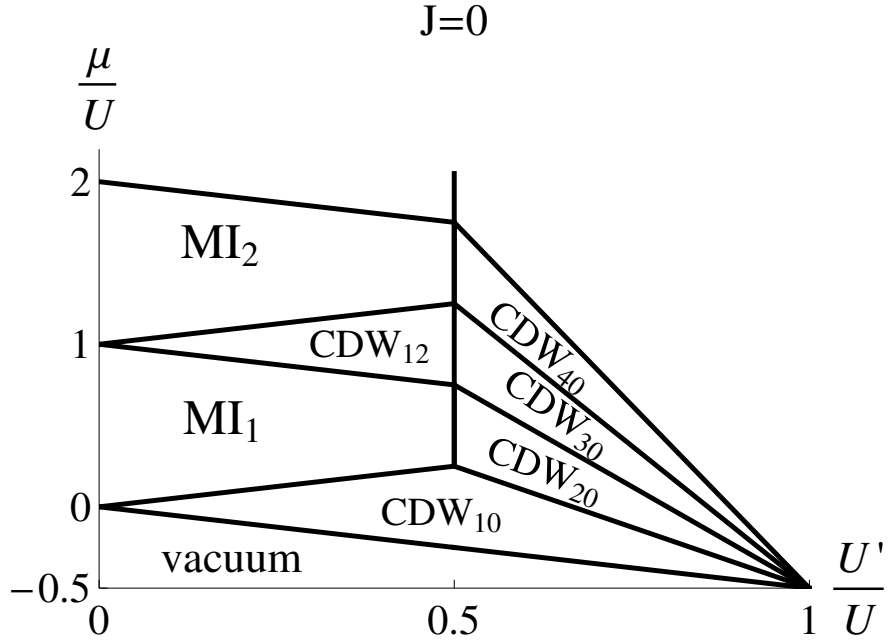


Figure 3.2: Phase diagram of a homogeneous Bose gas in the absence of tunneling between lattice sites. The label MI_n denotes a Mott insulating phase with n atoms on each lattice site, and CDW_{nm} denotes a charge-density wave phase with n and m atoms on even and odd sites, or vice versa. The parameters U and U' are the strengths of the short- and long-range interactions, while μ is the chemical potential.

We define the imbalance in the ground state to be

$$I = \left| \frac{\sum_i (-1)^{x_i+y_i} \langle \hat{c}_i^\dagger \hat{c}_i \rangle}{\sum_i \langle \hat{c}_i^\dagger \hat{c}_i \rangle} \right|. \quad (3.9)$$

For $J = 0$, the ground state is balanced ($I = 0$) or partially imbalanced ($I < 1$) for $\frac{U'}{U} < \frac{1}{2}$, and fully imbalanced ($I = 1$) for $\frac{U'}{U} > \frac{1}{2}$. The wavefunction collapses to a state with infinite particles on every site for $U' > U$.

$$J \neq 0, \quad 0 \leq U' \leq U/2$$

For finite tunneling strength J , we minimize the energy in Eq. (3.7) numerically. The ground state is a superfluid (SF) if $\langle c_i \rangle$ is uniform and non zero. The ground

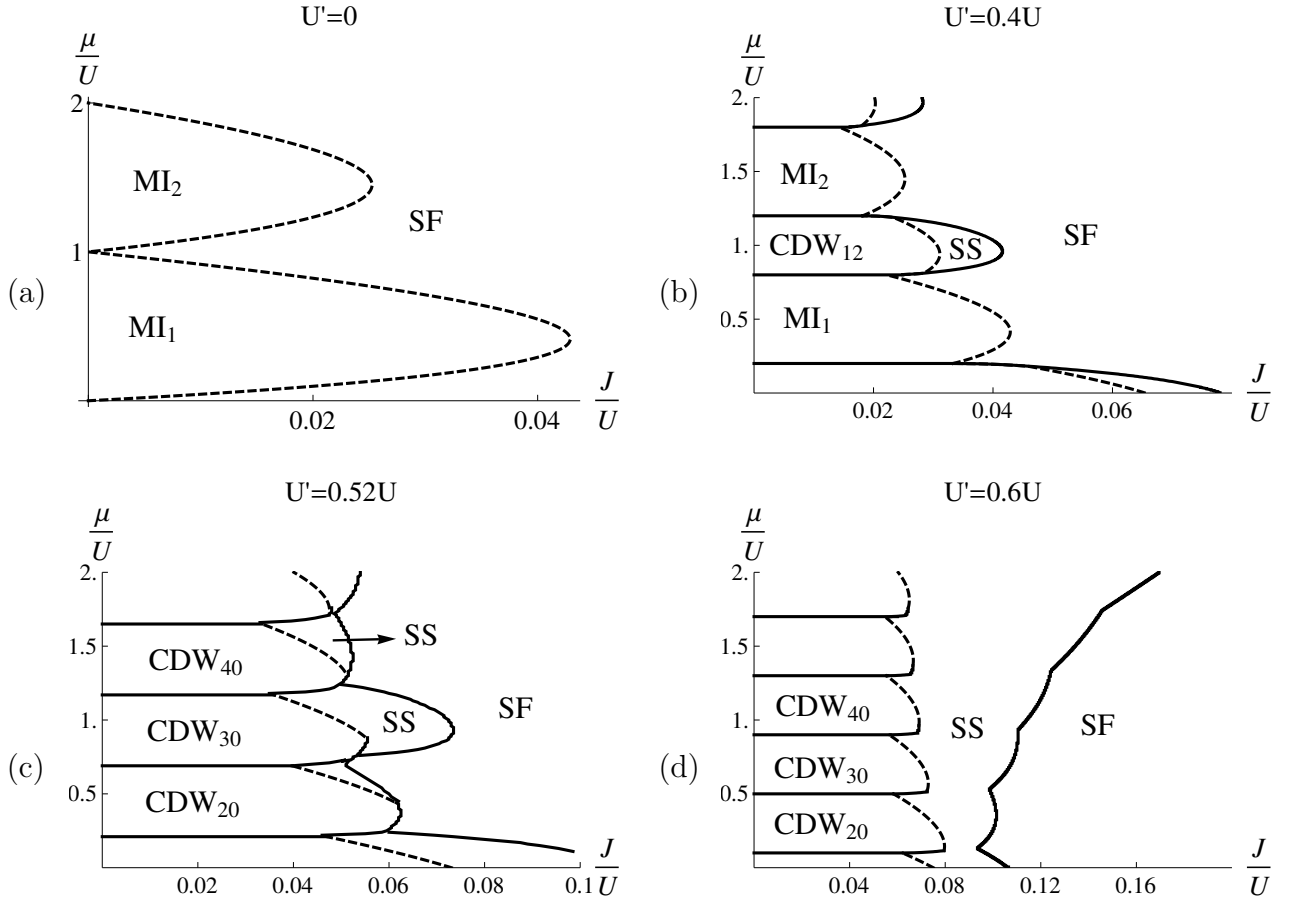


Figure 3.3: Phase diagram of a homogeneous Bose gas for four different values of the long-range interaction strength U' . SS denotes supersolid, and SF denotes superfluid. Dashed lines indicate second-order phase transitions, and solid lines indicate first order. The parameter J is the tunneling strength between lattice sites.

state is a supersolid (SS) if $\langle c_i \rangle \neq \langle c_j \rangle \neq 0$, where i and j are even and odd sites.

Phase diagrams for four different values of U' are plotted in Fig. 3.3.

For $0 < \frac{U'}{U} < \frac{1}{2}$, partially imbalanced CDW and SS phases (with $I < 1$) appear in regions where $nU - \frac{U'}{2} < \mu < nU + \frac{U'}{2}$, where n is any integer. In these phases, the density on even and odd sites is unequal, and the symmetry between even and odd sites is spontaneously broken. In most regions of the CDW lobes, the CDW phase undergoes a second-order phase transition to the SS phase as J is increased

at constant μ and U' . We define Ω to be the determinant of the Hessian of the free energy in Eq. (3.7), computed at the optimal variational parameters in Eq. (3.8). At the second-order phase transition from SS to CDW, $\Omega = 0$. This yields a simple analytic expression for the phase boundary,

$$J = \frac{1}{z} \sqrt{\frac{(U'^2 - (\mu - Un)^2) ((U - U')^2 - (\mu - Un)^2)}{(\mu + U)^2 - U'^2}}, \quad (3.10)$$

where n is the occupation number on lattice sites with fewer atoms, in the CDW phase at $J = 0$. Our numerics confirm this result. Upon increasing J further, the SS phase undergoes a first-order phase transition to the SF phase. Near the edges of the CDW lobes ($\mu \sim nU \pm \frac{U'}{2}$), the CDW phase directly undergoes a first-order phase transition to SF. There are no analytic expressions for these first-order phase boundaries.

$$J \neq 0, \quad U/2 < U' < U$$

In this regime, the ground state is always a fully imbalanced ($I = 1$) CDW phase at $J = 0$. In this ground state, all the odd sites are empty, and the even sites have $n = \lceil \frac{\mu + U/2}{U - U'} \rceil$ atoms each, or vice versa. The ground state undergoes a first-order phase transition between different CDW phases periodically as μ is increased at constant J . For U' near $U/2$, the CDW regions are partially surrounded by SS lobes [see Fig. 3.3(c)]. As U' is increased further, the SS lobes grow in size and connect together to form a continuous SS region [see Fig. 3.3(d)]. In Figs. 3.3(c) and 3.3(d), the second-order transitions from CDW to SS are indicated by a dashed line. The phase boundaries of these second-order transitions are given by

$$J = \frac{1}{z} \sqrt{\frac{(U'n - \mu) ((U - U')n - \mu) (\mu + U - (U - U')n)}{U + \mu + U'n}}. \quad (3.11)$$

The SS undergoes a first-order phase transition to SF as J is increased further.

3.3 Inhomogeneous gas

In this section, we explore the phase diagram of a Bose gas in a harmonic trap, in the presence of infinite-range interactions mediated by an optical cavity. In experiments, the number of atoms N can be a control parameter. Further, the total number of sites K is not well defined. Thus, it is convenient to define $V = U' \frac{N}{K}$, and rewrite Eq. (3.4) as

$$\hat{H}_{\text{cav}} = -\frac{V}{N} \left(\sum_i (-1)^{x_i+y_i} \hat{c}_i^\dagger \hat{c}_i \right)^2. \quad (3.12)$$

To find the ground state of this model, we generalize Eq. (3.6), writing

$$|\psi\rangle = \sum_i \sum_{n=0}^{\infty} \frac{a_{ni}}{\sqrt{n!}} \left(\hat{c}_i^\dagger \right)^n |0\rangle. \quad (3.13)$$

The variational energy is then

$$\begin{aligned} E_{\text{var}} = & -J \sum_{\langle ij \rangle} \left(\sum_n \sqrt{n} a_{ni} a_{n+1,i} \right) \left(\sum_n \sqrt{n} a_{nj} a_{n+1,j} \right) \\ & + \sum_{n,i} \left(U \frac{n(n-1)}{2} - \mu_i n \right) |a_{ni}|^2 - V \frac{\left(\sum_{n,i} (-1)^{x_i+y_i} n |a_{ni}|^2 \right)^2}{\sum_{n,i} n |a_{ni}|^2}. \end{aligned} \quad (3.14)$$

We minimize E_{var} with respect to all the variational parameters. Due to the presence of infinite-range interactions in our model, traditional methods of treating spatially varying potentials, such as the local-density approximation (LDA), fail. We demonstrate the failure of the local-density approximation in the insulating phases in Sec. 3.3.1. We present our numerical results for the phase diagram in Sec. 3.3.2

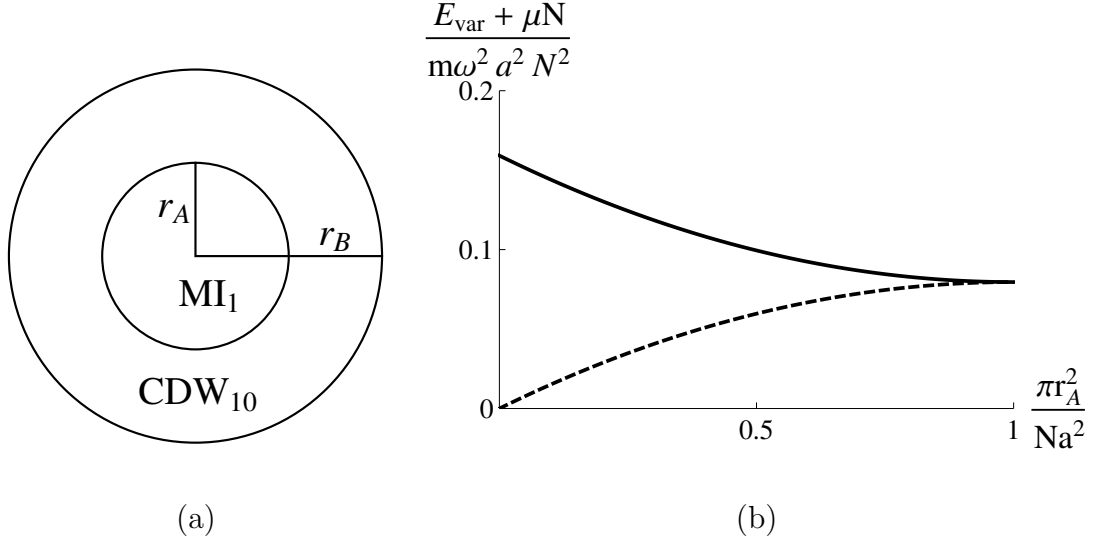


Figure 3.4: (a) A $n = 1$ Mott insulating core of radius r_A , surrounded by a CDW_{10} ring from radius r_A to r_B . (b) Scaled energy E_{var} as a function of scaled radius r_A for two cases: $V = 0$ (solid) and $V = \frac{Nm\omega^2 a^2}{2\pi}$ (dotted).

3.3.1 $J=0$

In the absence of tunneling, every lattice site has an integer number of atoms. For most of the experimentally relevant parameters, it suffices to consider only zero or one atom on every site. One expects the cloud to have a MI_1 core of radius r_A with unit filling, as shown in Fig. 3.4(a). This core is expected to be surrounded by a CDW_{10} ring extending from radius r_A to radius r_B . The CDW_{10} ring is surrounded by vacuum. In the limit of a slowly varying trap, the variational energy can be approximated as

$$\begin{aligned}
E_{\text{var}} &= \frac{1}{a^2} \int_0^{r_A} 2\pi r dr \left(\frac{1}{2} m\omega^2 r^2 - \mu \right) \\
&\quad + \frac{1}{a^2} \int_{r_A}^{r_B} \pi r dr \left(\frac{1}{2} m\omega^2 r^2 - \mu \right) - \frac{V}{N} \left(\frac{\pi(r_B^2 - r_A^2)}{2a^2} \right)^2 \\
&= \frac{\pi m\omega^2}{8a^2} (r_A^4 + r_B^4) - \frac{\pi\mu}{2a^2} (r_A^2 + r_B^2) - \frac{V}{N} \left(\frac{\pi(r_B^2 - r_A^2)}{2a^2} \right)^2.
\end{aligned} \tag{3.15}$$

Fixing the number of particles $N = \frac{\pi}{2a^2} (r_A^2 + r_B^2)$, the variational energy is

$$E_{\text{var}} = \left(\frac{m\omega^2 a^2}{4\pi} - \frac{V}{N} \right) \left(N - \frac{\pi r_A^2}{a^2} \right)^2 + \frac{N^2 m\omega^2 a^2}{4\pi} - \mu N. \tag{3.16}$$

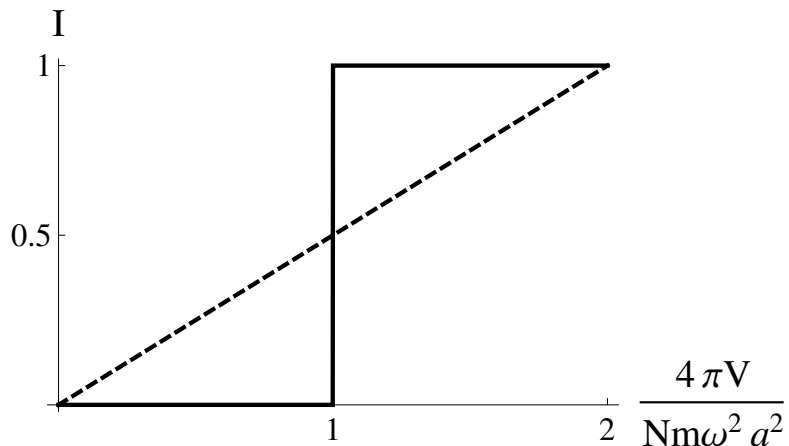


Figure 3.5: Comparison of LDA and full theory. Vertical axis shows the particle imbalance I between even and odd sites. Horizontal axis shows the strength of the long-range interaction. LDA (dashed line) shows a continuous growth of the imbalance, while the full theory (solid line) shows a discontinuity.

This variational energy is plotted as a function of r_A in Fig. 3.4(b). The energy minimum occurs at

$$r_A = \begin{cases} 0 & \text{if } V > \frac{Nm\omega^2 a^2}{4\pi}, \\ \sqrt{\frac{Na^2}{\pi}} = r_B & \text{if } V < \frac{Nm\omega^2 a^2}{4\pi}. \end{cases} \quad (3.17)$$

The ground state transitions from a completely Mott insulating gas to a completely checkerboarded gas at the critical value $V = \frac{Nm\omega^2 a^2}{4\pi}$, where the imbalance between even and odd sites undergoes an abrupt jump from 0 to 1 (see solid line in Fig. 3.5). We contrast this result to the predictions of LDA (which are not valid because of the long-range interactions). In traditional LDA, the local phase at position \vec{r} is that of a homogeneous system with chemical potential $\mu(\vec{r})$. As seen in Fig. 3.2, this implies that unless $V = 0$, one always has a CDW ring. A straightforward calculation of the imbalance between even and odd sites shows that within this approximation, the imbalance grows gradually as V is increased. The dashed line in Fig. 3.5 depicts the imbalance obtained from this LDA calculation, with $K = 2N$ lattice sites.

3.3.2 Phase diagram

In this section, we use numerical methods to calculate the phase diagram of an inhomogeneous Bose gas in a harmonic trap. We work in a relatively small density regime, and truncate the ansatz to allow 0, 1, or 2 atoms per site. For a 35×35 square lattice, we numerically minimize the variational energy in Eq. (3.14) with respect to 2450 independent variational parameters. In the ground state, the atoms arrange in concentric shells of insulating ($\text{MI}_n/\text{CDW}_{\text{mn}}$) and conducting (SS/SF) regions. We label the state of the gas at every point in the phase diagram by listing the phases of the atoms in these shells, in the order that they occur outwards from the center of the cloud. For example, SF denotes that the entire cloud is superfluid, and $\text{MI}_1\text{-SF}$ denotes that the center of the cloud is in the Mott insulating phase with unit filling, surrounded by a superfluid ring. In Fig. 3.6, we show the phase diagram for $\mu = 0.5U$ and $m\omega^2 a^2 = 0.01U$. For the range of hopping and long-range interaction that we consider, we find six different ways that the atoms arrange, namely SF, $\text{MI}_1\text{-SF}$, SS, $\text{SS-CDW}_{10}\text{-SS}$, $\text{CDW}_{10}\text{-SS}$, and $\text{CDW}_{20}\text{-SS-CDW}_{10}\text{-SS}$. We find similar results for other parameters, but the exact locations of the phase boundaries differ. Below, we discuss some of the interesting features in the phase diagram in Fig. 3.6.

The $\text{MI}_1\text{-SF}$ and SF phases have no sublattice imbalance, $I = 0$. In these phases, the long-range interaction term involving V does not contribute to the free energy. Therefore in this regime, the phase boundary between SF and $\text{MI}_1\text{-SF}$ does not depend on V , and the boundary is a vertical line at $J = \frac{\mu(U-\mu)}{z(U+\mu)} \simeq 0.04U$ for our parameters.

In the absence of tunneling and for a fixed chemical potential μ , the size of the cloud in the $\text{MI}_1\text{-SF}$ phase is $r = \sqrt{\frac{2\mu}{m\omega^2}}$. The free energy [from Eq. (3.16)] is

$E_{\text{var}} = -\frac{\pi\mu^2}{m\omega^2 a^2}$. In the CDW₁₀-SS phase, the cloud extends up to $r = \sqrt{\frac{2(\mu+V)}{m\omega^2}}$. The free energy of the CDW₁₀-SS phase is $E_{\text{var}} = -\frac{\pi(\mu+V)^2}{2m\omega^2 a^2}$. By comparing the free energies in the two phases, we find that the phase boundary between MI₁-SF and CDW₁₀-SS approaches $V = (\sqrt{2} - 1)\mu \simeq 0.2U$ as $J \rightarrow 0$. Numerically, we find that this is a good approximation even for $J \neq 0$.

A CDW₂₀ core appears inside the CDW₁₀ region if it is energetically cheaper to add atoms to the center rather than the edge of the cloud. In the absence of tunneling, the energy cost of adding an atom to an occupied site in the center of a CDW₁₀ cloud is $U - \mu - V$. There is no energy cost for adding an atom at the edge of a CDW₁₀ cloud. Therefore in the absence of tunneling, the phase boundary between CDW₁₀-SS and CDW₂₀-SS-CDW₁₀-SS occurs at $V = U - \mu = 0.5U$. Numerically, we find that this is a good approximation even for $J \neq 0$.

The phase diagram in Fig. 3.6 exhibits a multicritical point at $J \sim 0.04U, V \sim 0.2U$. At this multicritical point, the SF, MI₁-SF, CDW₁₀-SS, and SS-CDW₁₀-SS phases coexist. We find two other tricritical points at $J \sim 0.06U, V \sim 0.27U$, and $J \sim 0.018U, V \sim 0.5U$.

3.3.3 Comparison to experiment

Experimentalists in Zurich attempted to generate a phase diagram similar to Fig. 3.6 [86]. By monitoring the intensity in the cavity, they could detect a transition from a state with no sublattice imbalance to one in which imbalance is present. For example, this technique can find the transition from SF to SS. The researchers also monitored the condensate fraction as a function of lattice depth, finding kinks which they interpreted as phase transitions. Indeed, the appearance of an insulat-

ing region should generate such a kink. In generating their figures, the researchers only include the kink at largest J/U . The resulting phase diagram agrees well with the thick lines in Fig. 3.6(b). Further analysis of their data should reveal the other curves in Fig. 3.6(b).

3.4 Summary

We calculated the phase diagram of a two-dimensional Bose gas with short-range and long-range checkerboard interactions in an optical lattice. The long-range checkerboard interactions are produced by trapping the Bose gas in a single mode Fabry-Perot cavity, and illuminating it with a laser beam in the transverse direction. We found that, in the presence of these interactions, the Bose gas exhibits four phases - a Mott insulator with integer filling, a charge-density wave with different integer fillings on even and odd sites of the lattice, a superfluid with off-diagonal long-range order, and a supersolid with SF and CDW orders. We presented numerical results for the phase diagram of this homogeneous gas, and obtained analytical expressions for all the second-order phase boundaries. We also presented numerical results for the phase diagram of an inhomogeneous gas in a harmonic trap. Our numerical phase diagram agrees well with the phase diagram that was experimentally measured recently [86]. We predict that further analysis will reveal more phases in their data.

The system considered in this study is interesting for several reasons. First, due to long-range interactions, LDA fails. Second, the experiments in [86] made the first detection of a supersolid phase. One caveat is that this supersolid phase is a bit unusual, as it breaks only a global symmetry and not a local symmetry.

Thus one would never expect to see domain walls in the checkerboard order, unless they are imposed by using a cavity mode with nodes [81]. Beyond this system, atoms coupled to optical cavities provide an avenue to control atom-atom interactions. Similar setups which trap atoms in multimode cavities could be used to produce controllable medium-range interactions between atoms [81]. Multimode cavities can also be used to create phononlike excitations in the lattice. Atomic clouds trapped in cavities can be used to explore non-equilibrium phases [82] and nontrivial phase transitions in driven dissipative quantum systems [59, 35, 19].

ACKNOWLEDGMENT

This material was based upon work supported by the National Science Foundation Grant No. PHY-1508300.

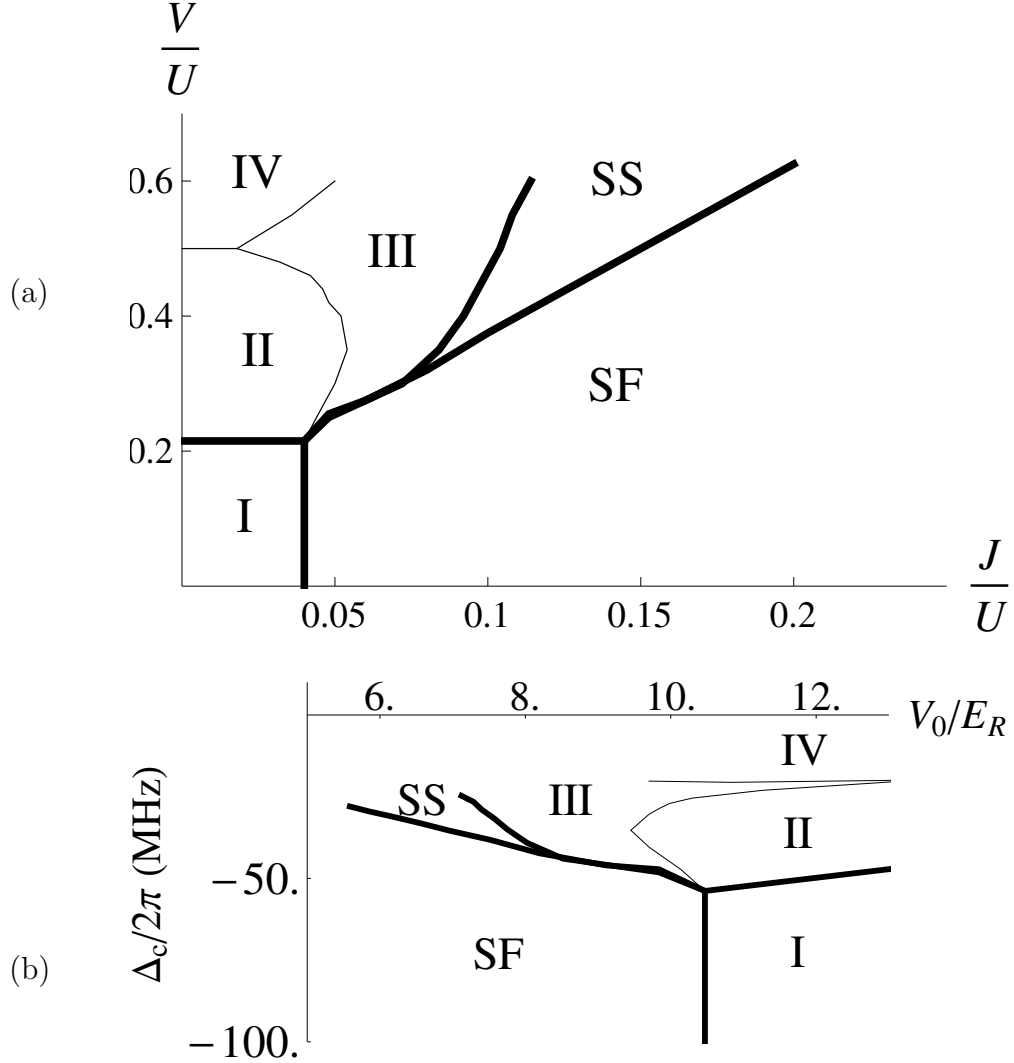


Figure 3.6: Phase diagram for an inhomogeneous Bose gas in a harmonic trap and an optical lattice, plotted against (a) model parameters, and (b) experimentally relevant parameters. Region I denotes MI₁-SF phase, II is CDW₁₀-SS, III is SS-CDW₁₀-SS, and IV is CDW₂₀-SS-CDW₁₀-SS. Thick lines denote phase boundaries measured in experiments [86]. The chemical potential is chosen to be $\mu = 0.5U$, and the trap frequency is such that $m\omega^2 a^2 = 0.01U$. In (b), V_0 is the lattice depth, and Δ_c is the detuning of the pump laser from the fundamental cavity mode. The Rabi frequency is chosen to be $\eta = \sqrt{\frac{2\pi}{N} \frac{E_R}{\hbar}}$, the scattering length is $100 a_0$, and the lattice constant and lattice depth in the z direction are 670 nm and $25E_R$, as consistent with experiments [86].

CHAPTER 4

PROPOSAL TO DIRECTLY OBSERVE THE KONDO EFFECT THROUGH ENHANCED PHOTOINDUCED SCATTERING OF COLD FERMIONIC AND BOSONIC ATOMS

MANY-BODY PHYSICS USING COLD ATOMS

Bhuvanesh Sundar, Ph.D.

Cornell University 2016

We propose an experimental protocol to directly observe the Kondo effect by scattering ultracold atoms. We propose using an optical Feshbach resonance to engineer Kondo-type spin-dependent interactions in a system with ultracold ${}^6\text{Li}$ and ${}^{87}\text{Rb}$ gases. We calculate the momentum transferred from the ${}^{87}\text{Rb}$ gas to the ${}^6\text{Li}$ gas in a scattering experiment and show that it has a logarithmically enhanced temperature dependence, characteristic of the Kondo effect and analogous to the resistivity of alloys with magnetic impurities. Experimentally detecting this enhancement will give a different perspective on the Kondo effect, and allow us to explore a rich variety of problems such as the Kondo lattice problem and heavy-fermion systems. The work in this chapter was done in collaboration with Prof. Erich Mueller. This chapter is adapted from a peer-reviewed article, *Physical Review A* **93**, 023635 (2016), which was co-authored with Prof. Erich Mueller.

Ultracold atomic gases provide a platform to engineer model Hamiltonians relevant for condensed matter physics phenomena. One such intriguing phenomenon is the Kondo effect [83, 63]. In this study, we propose an experimental protocol to engineer and measure the scattering properties of Kondo-like interactions between ultracold atoms. Such an experiment would give a new perspective on an iconic problem.

The Kondo effect is a transport anomaly that arises when itinerant electrons have spin-dependent interactions with magnetic impurities. The source of the phenomenon is a spin-singlet many-body bound state formed between the Fermi sea and an impurity. This bound state leads to resonant scattering of itinerant electrons off the screened impurities. As the temperature is lowered, this resonant scattering dominates over other scattering processes and leads to a characteristic logarithmic temperature dependence of the resistivity of the material. When the interactions between the electrons and the impurity are spin independent, no such bound state is formed, and the scattering is not enhanced.

The Kondo effect has been studied widely since the formulation of the Kondo model in 1964 [1, 2, 15, 16, 48, 49, 122, 58, 30]. Related problems such as the Kondo problem have been exactly solved [163, 5, 161, 6]. However, despite decades of intense research, some questions about the Kondo effect remain unresolved, and some of the key theoretical predictions have never been directly seen. For example, the electron cloud which screens the spin on the impurity has never directly been imaged [2, 1, 16, 15]. More importantly the analogous problem with an array of interacting impurities (the Kondo lattice) has aspects which are not well understood [155]. Exploring the Kondo lattice problem is of paramount importance to the understanding of heavy fermion systems and quantum criticality

[49, 48].

In this study, we propose using cold atoms to directly observe enhanced Kondo scattering. We envision a system consisting of a spin-1/2 Fermi gas and a dilute Bose gas with spin S , where bosonic atoms play the role of magnetic impurities and fermionic atoms play the role of electrons. To strengthen the analogy with immobile spin impurities in the Kondo model, we consider bosons which are much heavier than the fermions. Fermion-boson pairs such as ${}^6\text{Li}$ - ${}^{87}\text{Rb}$ ${}^7\text{Li}$ - ${}^{85}\text{Rb}$ or ${}^6\text{Li}$ - ${}^{133}\text{Cs}$ are good candidates with large mass ratios. Alkaline-earth-metal and rare-earth atoms are also promising.

We consider a rotationally symmetric interaction between the ultracold atoms, which includes both density-density and spin-dependent interactions. We present an experimental protocol to produce such an interaction using an optical Feshbach resonance. For this general interaction, we calculate that the scattering cross section is strongly enhanced by the Kondo effect. We propose directly measuring this enhancement by launching the Bose gas into the Fermi gas with a small velocity. One would then measure the momentum transferred to the Fermi gas. A number of related experiments have been used to probe atomic scattering in the past [162, 154, 57, 135]. We show that at temperatures smaller than the Fermi temperature, the final momentum of the Fermi gas varies logarithmically with temperature, analogous to the resistance of electrons in an alloy with magnetic impurities. The temperature dependence of the transferred momentum, depicted in Fig. 4.1, has a minimum which is a signature of the Kondo effect, and this minimum can be detected at experimentally accessible temperatures. Alternatively, the enhanced scattering could be seen in the damping of collective modes of the atomic clouds in a trap [113].

This chapter is organized as follows. In Sec. 4.1 we introduce our atomic system and the model we consider. In Sec. 4.2 we explain how an optical Feshbach resonance can be used to produce the interactions considered in our model. In Sec. 4.3 we calculate the momentum exchanged in a scattering experiment between atomic clouds. We calculate the momentum transferred as a function of temperature perturbatively up to third order in the interaction strength. We explicitly describe all parts of our calculation in Appendix C. In Sec. 4.4 we estimate experimental parameters needed to observe Kondo physics, and address the experimental challenges faced. We summarize in Sec. 4.5.

4.1 Model

In this section we describe our model. In Sec. 4.2 we describe how to experimentally implement our model.

We build our system out of spin-1/2 fermions and spin- S bosons. In our implementation these will be hyperfine spins. We let the operators $\hat{a}_{r\alpha}^\dagger$ and $\hat{b}_{r\mu}^\dagger$ create fermionic and bosonic atoms at position \vec{r} and spin projection $\alpha = \uparrow, \downarrow$ or $\mu = -S, \dots, S$ along the z -axis. Their Fourier transforms,

$$\begin{aligned}\hat{a}_{k\alpha}^\dagger &= \frac{1}{\sqrt{V}} \int d^3\vec{r} \hat{a}_{r\alpha}^\dagger e^{i\vec{k}\cdot\vec{r}}, \\ \hat{b}_{k\mu}^\dagger &= \frac{1}{\sqrt{V}} \int d^3\vec{r} \hat{b}_{r\mu}^\dagger e^{i\vec{k}\cdot\vec{r}},\end{aligned}\tag{4.1}$$

create particles in momentum eigenstates. Above, V is the volume of the system.

We explore a model with a Hamiltonian $\hat{H} = \hat{H}_0 + \hat{H}_{\text{int}}$. The first term models

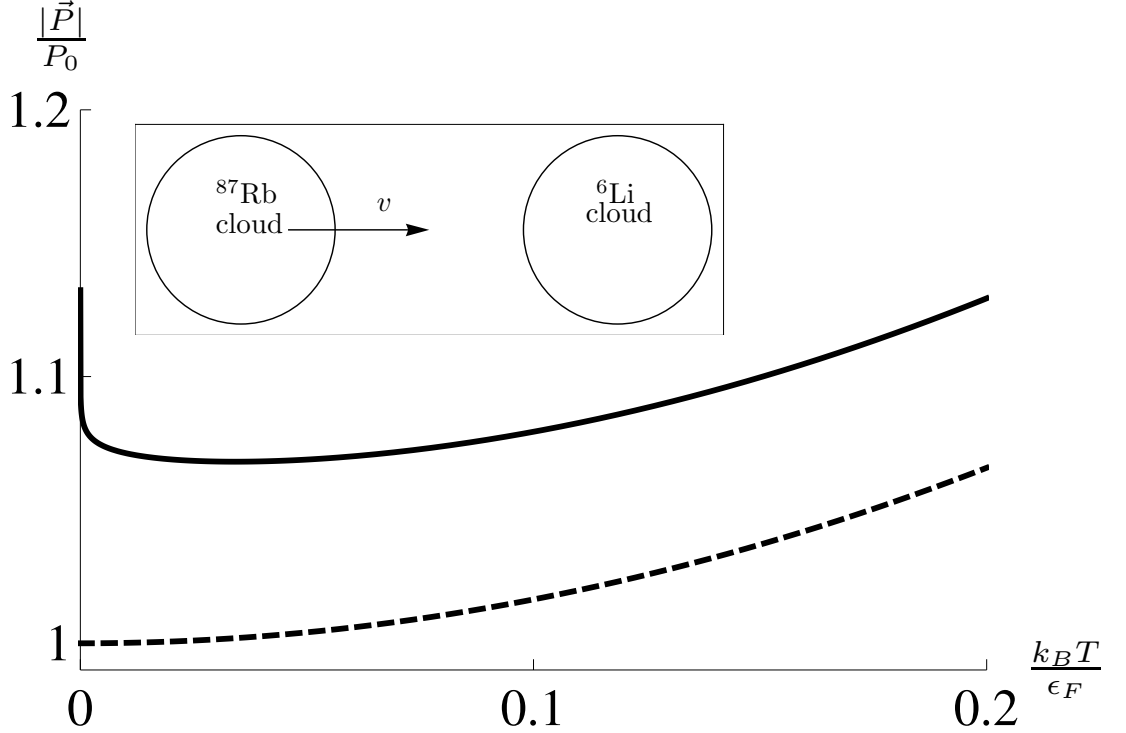


Figure 4.1: Temperature dependence of the momentum \vec{P} transferred from bosons to fermions in a scattering experiment with photoinduced interactions. Both \vec{P} and temperature have been rescaled to dimensionless quantities. P_0 denotes the momentum transferred to the Fermi gas at zero temperature when the interactions are spin independent ($g_s = 0$). (Solid line) Spin-dependent interactions between spin-1/2 fermions and spin-1 bosons with $g_s = \frac{-1}{3}g_n = \frac{0.1\epsilon_F}{N/v}$; (Dashed line) Spin-independent interactions ($g_s = 0$ and $g_n = -3 \times \frac{0.1\epsilon_F}{N/v}$). The minimum in \vec{P} is a signature of the Kondo effect, and may be detected experimentally. In Sec. 4.4 we estimate experimental parameters to achieve the interaction strength used here. Inset shows a cartoon of the collision.

the kinetic energy of the fermions and bosons,

$$\hat{H}_0 = \frac{V}{(2\pi)^3} \int d^3\vec{k} \left(\sum_{\alpha} (\epsilon_k - \mu) \hat{a}_{k\alpha}^{\dagger} \hat{a}_{k\alpha} + \sum_{\mu} E_k \hat{b}_{k\mu}^{\dagger} \hat{b}_{k\mu} \right),$$

$$\epsilon_k = \frac{\hbar^2 k^2}{2m_a}, \quad E_k = \frac{\hbar^2 k^2}{2M_b}. \quad (4.2)$$

For the interactions modeled by \hat{H}_{int} , we consider a generic form of local spherically symmetric pairwise Bose-Fermi interactions. Since the fermions have spin-1/2, the

most general such interaction has the form,

$$\hat{H}_{\text{int}} = \int d^3\vec{r} \sum_{\alpha\beta\mu\nu} \hat{a}_{r\alpha}^\dagger \hat{a}_{r\beta} \hat{b}_{r\mu}^\dagger \hat{b}_{r\nu} \left(g_s \vec{\sigma}_{\alpha\beta}^{(a)} \cdot \vec{\sigma}_{\mu\nu}^{(b)} + g_n \delta_{\alpha\beta} \delta_{\mu\nu} \right). \quad (4.3)$$

We denote the vector of spin matrices for the fermions and bosons by $\vec{\sigma}^{(a)}$ and $\vec{\sigma}^{(b)}$, and δ refers to the Kronecker delta function. It is important to note that \hat{H}_{int} contains terms where $\alpha \neq \beta$ and $\mu \neq \nu$. This encodes the fact that the atoms exchange spin when they collide. We point out that spherical symmetry of the Hamiltonian is not a necessary feature to observe Kondo physics. Any Hamiltonian which allows spin exchange processes at third order of interaction strength would produce an enhanced scattering cross section at low temperatures. We restrict ourselves to interactions modeled by Eq. (4.3), and we show in Sec. 4.2 that this has a simple experimental realization.

It is useful to rewrite \hat{H}_{int} in momentum space as

$$\hat{H}_{\text{int}} = \frac{V^2}{(2\pi)^9} \int d^3\vec{k} \int d^3\vec{p} \int d^3\vec{q} \sum_{\alpha\beta\mu\nu} \hat{a}_{k+q,\alpha}^\dagger \hat{a}_{k+p,\beta} \hat{b}_{k-q,\mu}^\dagger \hat{b}_{k-p,\nu} \left(g_s \vec{\sigma}_{\alpha\beta}^{(a)} \cdot \vec{\sigma}_{\mu\nu}^{(b)} + g_n \delta_{\alpha\beta} \delta_{\mu\nu} \right).$$

Our model in Eq. (4.4) differs from the one in the spin- S Kondo model [83] in two respects. The bosonic atoms, which play the role of impurities, are mobile. Due to their large mass however, the recoil of the bosonic atoms can be neglected, and formally the physics is equivalent to that of immobile spin impurities. In addition to the regular spin- S Kondo-like interaction, Eq. (4.4) contains a density-density interaction. We show that in spite of such an additional interaction term, the momentum transferred to the Fermi gas in a scattering experiment still has a minimum at a certain temperature, albeit at a lower temperature than the case with no density-density interaction.

The interaction we have considered in Eq. (4.3) does not occur in typical cold atom experiments in which interaction strengths are tuned using a magnetic

Feshbach resonance. In a typical magnetic Feshbach resonance, spin-exchange collisions are off-resonance and will not be observed. In the following section we propose using an optical Feshbach resonance to produce the interaction in Eq. (4.3) .

4.2 An experimental setup

In this section we describe our proposal to experimentally implement the model introduced in Sec. 4.1 using ${}^6\text{Li}$ and ${}^{87}\text{Rb}$ atoms as our itinerant fermions and spin impurities. As we will show, producing a strong interaction between ${}^6\text{Li}$ and ${}^{87}\text{Rb}$ using an optical Feshbach resonance requires a large matrix element for photoassociation. Experiments [39] show ${}^7\text{Li}$ and ${}^{85}\text{Rb}$ to have the highest photoassociation rate coefficient among all the bialkali metal combinations. We expect their isotopes ${}^6\text{Li}$ and ${}^{87}\text{Rb}$ to have similar photoassociation rates, and we chose ${}^6\text{Li}$ and ${}^{87}\text{Rb}$ in our proposal to produce the Kondo model because they are readily available in ultracold atomic experiments. The ${}^6\text{Li}$ and ${}^{87}\text{Rb}$ atoms have quantum numbers $S = 1/2$, $L = 0$ and $I = 1$ and $3/2$.

In an optical Feshbach resonance, a laser beam provides a coupling between the open scattering channel and a closed channel containing a bound state [44, 74, 26, 153]; here the open channel is an electronic spin-singlet of ${}^6\text{Li}$ and ${}^{87}\text{Rb}$, and the bound state is a highly excited LiRb molecular state. When the laser is far detuned from resonance with the bound state, the bound state can be adiabatically eliminated, and we are left with an AC Stark shift for the ${}^6\text{Li}$ - ${}^{87}\text{Rb}$ singlet. The triplet state sees no Stark shift. This provides a mechanism for spin exchange. While this optically induced spin exchange has not yet been experi-

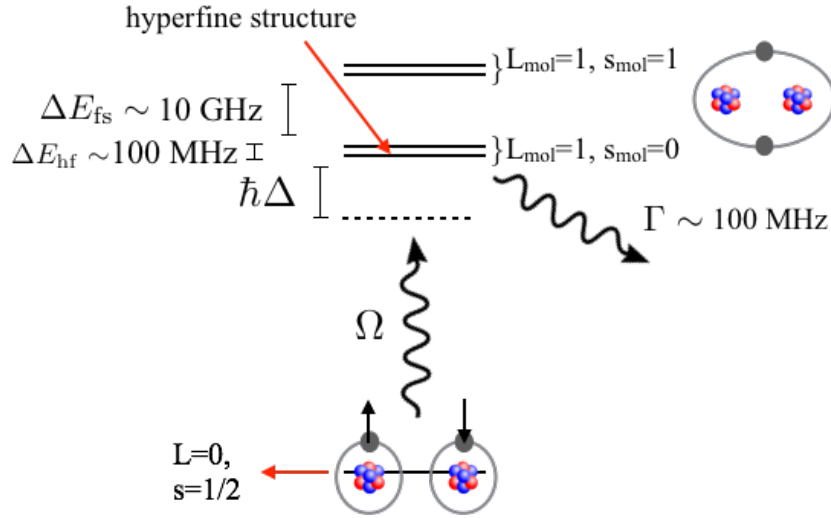


Figure 4.2: (Color online) Setup to produce an optical Feshbach resonance between ${}^6\text{Li}$ and ${}^{87}\text{Rb}$ atoms. We couple ${}^6\text{Li}$ and ${}^{87}\text{Rb}$ atoms in their ground states to a ${}^6\text{Li}{}^{87}\text{Rb}$ molecule with angular momenta $L = 1, S = 0$ by shining a laser whose detuning Δ from the molecule is such that $\hbar\Gamma, \Delta E_{\text{hf}} < \hbar\Delta \ll \Delta E_{\text{fs}}$. Here, Γ is the molecular linewidth, and ΔE_{hf} and ΔE_{fs} are the hyperfine and fine structure splitting in the molecule. Typical values of Γ , ΔE_{hf} , and ΔE_{fs} for molecules are provided in the figure (for example, see [38]). In this limit, we obtain an effective Kondo-type spin-dependent interaction between ${}^6\text{Li}$ and ${}^{87}\text{Rb}$ atoms.

mentally observed, there have been extensive studies of both elastic and inelastic scattering properties near heteronuclear optical Feshbach resonances of ${}^7\text{Li}$ and ${}^{85}\text{Rb}$ [39, 38]. Thus the transition frequencies for forming ${}^7\text{Li}{}^{85}\text{Rb}$ molecules are well known. We expect that the linewidths, transition matrix elements, and spectral densities for other alkali-metal combinations such as ${}^6\text{Li}{}^{87}\text{Rb}$ molecules will be similar.

Below we provide a mathematical framework to model the optical Feshbach resonance and obtain an effective interaction between the ${}^6\text{Li}$ and ${}^{87}\text{Rb}$ atoms. The scheme to produce the optical Feshbach resonance is illustrated in Fig. 4.2. All the physics described in this section is local, and we have dropped the index labeling the position of the atoms from the second-quantized operators.

The energy density for the relevant electronic and nuclear degrees of freedom in each atom and molecule is of the form,

$$\hat{H} = \hat{H}_{\text{HF}}^{\text{Li}} + \hat{H}_{\text{HF}}^{\text{Rb}} + \hat{H}_{\text{mol}} + \hat{H}_{\text{Fesh}}. \quad (4.4)$$

\hat{H}_{mol} models the binding energy of the molecule:

$$\hat{H}_{\text{mol}} = \sum_{mm'} E_b \hat{\gamma}_{mm'}^\dagger \hat{\gamma}_{mm'}, \quad (4.5)$$

where $\hat{\gamma}_{mm'}^\dagger$ creates a molecule with an electronic spin $S = 0$ and electronic orbital angular momentum $L = 1$. The indices m and m' label the nuclear spins of the ${}^6\text{Li}$ and ${}^{87}\text{Rb}$ atoms. If the quantization axis of the electronic orbital angular momentum is chosen along the direction of angular momentum of the laser photon inducing the Feshbach resonance, then only one of the molecular states in the $L = 1$ triplet is coupled via the laser to the atomic singlet. We denote the binding energy of this molecular state by E_b .

The hyperfine Hamiltonians for the atoms are

$$\begin{aligned} \hat{H}_{\text{HF}}^{\text{Li}} &= hA_{\text{Li}} \sum_{\substack{m_S, m'_S \\ m_I, m'_I}} \hat{a}_{m_S m_I}^\dagger \hat{a}_{m'_S m'_I} \vec{\sigma}_{m_S m'_S}^{(1/2)} \cdot \vec{\sigma}_{m_I m'_I}^{(1)} \\ \hat{H}_{\text{HF}}^{\text{Rb}} &= hA_{\text{Rb}} \sum_{\substack{m_S, m'_S \\ m_I, m'_I}} \hat{b}_{m_S m_I}^\dagger \hat{b}_{m'_S m'_I} \vec{\sigma}_{m_S m'_S}^{(1/2)} \cdot \vec{\sigma}_{m_I m'_I}^{(3/2)} \end{aligned} \quad (4.6)$$

where h is Planck's constant, $A_{\text{Li}} = 152\text{MHz}$ and $A_{\text{Rb}} = 3.4\text{GHz}$ are the hyperfine coupling constants of ${}^6\text{Li}$ and ${}^{87}\text{Rb}$ [7], $\vec{\sigma}^{(S)}$ is the vector of spin- S matrices, and $\hat{a}_{m_S m_I}^\dagger$ and $\hat{b}_{m_S m_I}^\dagger$ create a ${}^6\text{Li}$ and ${}^{87}\text{Rb}$ atom in the state $|m_S m_I\rangle$. In terms of the hyperfine eigenstates,

$$|m_S, m_I\rangle = \sum_{F, m_F} C_{m_S m_I}^{F m_F} |F, m_F\rangle \quad (4.7)$$

where $C_{m_S m_I}^{F m_F}$ are Clebsch-Gordan coefficients.

The terms in \hat{H}_{Fesh} describe the interactions between the photoassociation laser and the atoms. We model this photoinduced molecular formation by

$$\hat{H}_{\text{Fesh}} = \sum_{mm'} \Omega e^{i(\vec{k}\cdot\vec{r}-\omega t)} \hat{\gamma}_{mm'}^\dagger \frac{\hat{a}_{\frac{1}{2}m} \hat{b}_{-\frac{1}{2}m'} - \hat{a}_{-\frac{1}{2}m} \hat{b}_{\frac{1}{2}m'}}{\sqrt{2}} + \text{H.c.} \quad (4.8)$$

where \vec{r} is the position of the atoms, and $\hbar\vec{k}$ and ω are the momentum and frequency of the laser photon inducing molecule formation. In the rotating frame, the detuning Δ between the atomic and molecular states is $\Delta = \omega - \frac{E_b}{\hbar}$, and Ω is the transition matrix element from the atomic to the molecular state.

The laser detuning is typically larger than the transition matrix element. We also choose the detuning to lie between the hyperfine and fine structure of the molecular states, and to be larger than the molecular linewidth: $\Gamma, \Delta E_{\text{hf}} < \hbar\Delta \ll \Delta E_{\text{fs}}$. This is done for three reasons. First, choosing a detuning less than the fine structure splitting ensures that only the molecule with $L = 1, S = 0$ is coupled. Second, choosing a detuning larger than hyperfine structure ensures that all hyperfine molecular states in the $L = 1, S = 0$ manifold have the same transition matrix element Ω . Third, a detuning larger than the linewidth ensures that the occupation in the molecular state will be small, and enables us to obtain an effective interaction between the ${}^6\text{Li}$ and ${}^{87}\text{Rb}$ in second order perturbation theory in Ω :

$$\hat{H}_{\text{int}} = \sum_{mm'} \frac{-\Omega^2}{\hbar\Delta} \left(\frac{\hat{a}_{\frac{1}{2}m} \hat{b}_{-\frac{1}{2}m'} - \hat{a}_{-\frac{1}{2}m} \hat{b}_{\frac{1}{2}m'}}{\sqrt{2}} \right)^\dagger \times \left(\frac{\hat{a}_{\frac{1}{2}m} \hat{b}_{-\frac{1}{2}m'} - \hat{a}_{-\frac{1}{2}m} \hat{b}_{\frac{1}{2}m'}}{\sqrt{2}} \right). \quad (4.9)$$

Using Eq. (4.7), the operators $\hat{a}_{m_{SM_I}}^\dagger$ and $\hat{b}_{m_{SM_I}}^\dagger$ can be projected into the hyperfine eigenstate basis. Assuming that the chemical potential is set such that the $F = 3/2$ and $F = 2$ manifolds are unoccupied, we project \hat{H}_{int} into the $F = 1/2$ and $F = 1$ manifolds. We obtain an effective interaction

$$\hat{H}_{\text{int}} = \frac{-\Omega^2}{\hbar\Delta} \sum_{\alpha\beta\mu\nu} \hat{a}_\alpha^\dagger \hat{a}_\beta \hat{b}_\mu^\dagger \hat{b}_\nu \left(-\frac{1}{12} \vec{\sigma}_{\alpha\beta}^{(a)} \cdot \vec{\sigma}_{\mu\nu}^{(b)} + \frac{1}{4} \delta_{\alpha\beta} \delta_{\mu\nu} \right). \quad (4.10)$$

The first term in Eq. (4.10) is of the form of Kondo-like interactions with $g_s = \frac{1}{12} \frac{\Omega^2}{\hbar\Delta}$, and the second term a density-density interaction with $g_n = \frac{-1}{4} \frac{\Omega^2}{\hbar\Delta}$, where g_s and g_n were defined in Eq. (4.3). Generally, in addition there would also be intrinsic interactions which modify the values of g_s and g_n in the experiment. To explore Kondo physics, g_s should be positive.

If one wanted to exactly produce the Kondo model (where $g_n = 0$), one could add more photoassociation lasers, for example, coupling the electronic spin-triplet atomic states. However as we show in Sec. 4.3, the presence of a nonzero g_n does not change the physics.

4.3 Kondo-enhanced scattering between ^{87}Rb and ^6Li

Here we calculate the momentum transfer in a collision between a fermionic cloud and a bosonic cloud. We show that spin-exchange collisions lead to a logarithmic temperature dependence of the momentum transferred. This logarithm is characteristic of the Kondo effect, and analogous to the behavior of electrical resistance of magnetic alloys. As shown in Fig. 4.1, it leads to a minimum in the momentum transferred. The most naive way to measure this momentum exchanged would be to launch the Bose gas into a stationary Fermi gas and measure the final momentum of the Fermi gas. We briefly consider an alternative method in Sec. 4.3.1.

The duration of interaction between a boson and the Fermi gas in the experiment described above is $t = L/v$ where L is the size of the Fermi cloud. We calculate the momentum transferred from the Bose gas to the Fermi gas at time t to zeroth order in $1/M_b$, first order in \vec{v} , and third order in the interaction parameters g_s and g_n . We perform this calculation for general values of g_s and g_n

that are independent of each other. At the end of our calculation we specialize to the values of g_s and g_n produced by our proposal in Sec. 4.2. Since L is a macroscopic quantity and we work in the small v limit, we make a long time approximation wherever possible. We assume that the Bose gas is dilute, and neglect events involving scattering of a fermion with more than one boson. Equivalently we calculate the momentum transferred by one boson with momentum $M_b\vec{v}$, and sum over all bosons. The Fermi surface will play an important role.

We consider the collision of the Fermi gas with one boson with spin projection m at time 0. The momentum of the Fermi gas at time t is then $\vec{P}_m = \frac{V}{(2\pi)^3} \int d^3\vec{k} \sum_{\alpha} \hbar\vec{k} n_{k\alpha m}(t)$, where

$$n_{k\alpha m}(t) = \langle \hat{b}_{M_b v, m}(0) \hat{a}_{k\alpha}^{\dagger}(t) \hat{a}_{k\alpha}(t) \hat{b}_{M_b v, m}^{\dagger}(0) \rangle \quad (4.11)$$

is the occupation of fermions with momentum \vec{k} and spin projection α at time t . In Eq. (4.11) the expectation value is taken over a thermal ensemble of fermions, with no bosons present. The bosonic creation operator preceding the ket state in Eq. (4.11) ensures that we calculate the occupation n_k after the collision of *one* boson with the Fermi gas. Since the bosons are spin unpolarized, the average momentum imparted by a boson is $\vec{P}_{av} = \frac{V}{3(2\pi)^3} \int d^3\vec{k} \sum_{\alpha m} \hbar\vec{k} n_{k\alpha m}(t)$. Multiplying by N_b , the number of bosons, the net momentum of the Fermi gas is

$$\vec{P}(t) = \frac{N_b V}{3(2\pi)^3} \int d^3\vec{k} \sum_{\alpha m} \hbar\vec{k} n_{k\alpha m}(t). \quad (4.12)$$

In Appendix C.1, we describe our diagrammatic perturbation theory approach for calculating $n_{k\alpha m}(t)$. We find that

$$\frac{1}{3} \sum_m n_{k\alpha m}(t) = f_k - \frac{4t\vec{k} \cdot \vec{v} \rho(\epsilon_k)}{V^2} \frac{\partial f_k}{\partial \epsilon_k} \times \left(\frac{S(S+1)}{4} \tilde{g}_s^2 + \tilde{g}_n^2 - \frac{\tilde{g}_s^3 S(S+1)}{4(2\pi)^3} \int d^3\vec{p} \frac{f_p}{\epsilon_k - \epsilon_p} \right), \quad (4.13)$$

plus terms which scale as t^0, v^2 or $1/M_b$. Due to our use of point interactions, the interaction parameters g_s and g_n are renormalized to \tilde{g}_s and \tilde{g}_n . These renormalized (physical) coupling constants are the ones appearing in Eq. (4.13). This renormalization of the interaction strength occurs at all orders of perturbation theory.

To calculate $\vec{P}(t)$, we sum the contributions due to all momentum states, and include the temperature dependence of the fermionic chemical potential, $\mu = \epsilon_F \left(1 - \frac{\pi^2}{12} \left(\frac{k_B T}{\epsilon_F}\right)^2\right) + O\left(\frac{k_B T}{\epsilon_F}\right)^4$. We find that at long times,

$$\begin{aligned} \vec{P} = & \frac{3S(S+1)N_b}{8} \left(\frac{J}{\epsilon_F}\right)^2 (k_F L) \hbar k_F \left(\left(1 + \frac{4}{S(S+1)} \left(\frac{\tilde{g}_n}{\tilde{g}_s}\right)^2\right) \left(1 + \frac{\pi^2}{6} \left(\frac{k_B T}{\epsilon_F}\right)^2\right) \right. \\ & \left. - \frac{3J}{2\epsilon_F} \left(1.13 + \left(2.6 - \frac{\pi^2}{48}\right) \left(\frac{k_B T}{\epsilon_F}\right)^2 + \frac{1}{2} \log \frac{k_B T}{4\epsilon_F} \left(1 + \frac{5\pi^2}{12} \left(\frac{k_B T}{\epsilon_F}\right)^2\right)\right) \right), \end{aligned} \quad (4.14)$$

where $J = \tilde{g}_s \frac{N}{V}$, and $\frac{N}{V}$ is the density of fermions. In Eq. (4.14) we have neglected terms which scale as $t^0, v^2, \frac{1}{M_b}$ or T^4 . According to our proposal in Sec. 4.2, $\frac{\tilde{g}_n}{\tilde{g}_s} = -3$ and $S = 1$. The result of Eq. (4.14) is plotted in Fig. 4.1 using these parameters and $J = 0.1\epsilon_F$. For comparison, we also plot the momentum transferred to the Fermi gas for spin-independent interactions with the same value of $\tilde{g}_n = -3 \times \frac{0.1\epsilon_F}{N/V}$ and $\tilde{g}_s = 0$. The logarithmic temperature dependence of \vec{P} for spin-dependent interactions is characteristic of Kondo physics. Equation (4.14) breaks down when $\frac{J}{\epsilon_F} \log \frac{k_B T}{\epsilon_F} \simeq O(1)$. Below this temperature, the logarithmic increase saturates to a constant. Calculation of this saturation is the subject of the Kondo problem and can be addressed with renormalization group or Bethe ansatz methods. Equation (4.14) also breaks down when $v \simeq \frac{k_B T}{\hbar k_F}$.

The momentum transferred $|\vec{P}|$ has a minimum at a temperature

$$T_{\min} \sim \frac{3}{2\pi k_B} \sqrt{\frac{J\epsilon_F}{1 + \frac{4\tilde{g}_n^2}{\tilde{g}_s^2 S(S+1)}}}. \quad (4.15)$$

For the parameters $\frac{\tilde{g}_n}{\tilde{g}_s} = -3$, $S = 1$, and $J = 0.1\epsilon_F$, this minimum occurs at a temperature $\frac{T}{T_F} \simeq O(0.05)$. At this temperature and interaction strength, the momentum imparted by one boson to the Fermi gas is $\frac{|\vec{P}|}{N_b} \simeq \frac{3}{4}\hbar k_F \left(\frac{J}{\epsilon_F}\right)^2 (k_F L)$. For a $20\mu\text{m}$ long Fermi cloud at a density of 10^{13}cm^{-3} , the momentum imparted per boson is nearly $1.2\hbar k_F$. We estimate in Sec. 4.4 that achieving $J = 0.1\epsilon_F$ would require high intensity lasers and tight trapping of the fermions. The observation of this minimum will be a direct experimental confirmation of Kondo physics.

4.3.1 Alternative methods to measure enhanced Kondo scattering

Here we briefly explain an alternative method to measure the enhanced Kondo scattering between a Fermi cloud and a Bose cloud. We consider inducing dipole oscillations of a Bose cloud and a Fermi cloud in a harmonic trap of frequency ω . The clouds will collide every half-cycle and exchange momentum \vec{P} . As a result the amplitude of oscillations of the Fermi cloud will reduce each half cycle. Conservation of momentum implies that the maximum fermion displacement X will reduce each half cycle by $\delta X \simeq \frac{|\vec{P}|}{N_a m_a \omega}$ where N_a is the number of fermions; the Bose cloud's amplitude will not change very much because of the bosons' heavy mass. The Bose-Fermi interaction interval is longer for a smaller relative momentum, and vice versa. Thus the momentum exchanged $|\vec{P}|$ is independent of the relative velocities of the cloud, leading to a linear decay of the amplitude rather than exponential; $\frac{d\delta X}{dt} \sim \frac{|\vec{P}|}{N_a m_a \pi}$. If the Bose-Fermi interactions are Kondo-

like, the damping rate of amplitude of oscillations will have a minimum at the same temperature as $|\vec{P}|$ does, $T_{\min} \sim \frac{3}{2\pi k_B} \sqrt{\frac{J\epsilon_F}{1 + \frac{4g_b^2}{g_s^2 S(S+1)}}$. For a typical amplitude of oscillation $X \simeq 100\mu\text{m}$ in a trap of frequency $\omega = 2\pi \times 10$ Hz, and if $\frac{N_a}{N_b} = 200$, the amplitude will decay to zero in about 12 oscillations at $T = T_{\min}$. The observation of a minimum in the damping rate will also be an experimental confirmation of Kondo physics.

4.4 Experimental considerations for an optical Feshbach resonance

In this section we estimate experimental parameters to optimize model parameters, g_s and g_n , and the rates of heating and atom losses. The relevant independent parameters in an experiment that implements our proposal are the intensity I of the laser used to induce a Feshbach resonance, the laser detuning Δ , and the densities n_f and n_b of the fermions and bosons. These parameters have to be chosen to satisfy three criteria: a) The gas is always in thermal equilibrium; b) The allowed duration of the experiment is long enough for spin-dependent interaction effects to be significant; and c) The temperature and time scales in our proposal are accessible to current experiments. We in fact find below that satisfying these criteria requires a large intensity of about $1 \text{ MW}/\text{cm}^2$, and that a typical experiment would only last about $11\mu\text{s}$ before the gases heat up beyond the desired temperature. These limitations place our proposal beyond the reach of current experiments. A judicious choice of atomic species and of the resonance may reduce the intensity required.

Experiments implementing optical Feshbach resonances typically suffer from

high heating and atom loss rates, because pairs of atoms absorb photons to form bound molecules due to the molecules' finite linewidth. The excited molecular states have a finite recoil momentum, and either dissociate into free atoms with large kinetic energies, spontaneously decay to ground molecular states with a large kinetic energy, or tunnel out of the system. Spontaneous decay into particles with a large kinetic energy heats the gas, and molecules tunneling out of the system leads to particle loss.

The effect of a finite linewidth of the molecule can be incorporated by making the AC Stark shift obtained in Eq. (4.9) complex:

$$g = \frac{-\Omega^2}{\hbar\Delta + i\hbar\Gamma}, \quad (4.16)$$

where $\Delta = \omega - \frac{E_b}{\hbar}$ is the laser detuning from the molecular bound state. The real part of g , $|Re(g)| = \Omega^2 \frac{|\Delta|}{\hbar(\Delta^2 + \Gamma^2)}$, is a measure of the interaction strength, and determines the magnitude of the model parameters g_s and g_n [see Eq. (4.10)]. The temperature scale, T_{\min} , for observing Kondo physics is related to $g_s n_f$ and $g_n n_f$ where n_f is the density of fermions [see Eq. (4.15)]. The magnitude of the imaginary part of g is $Im(g) = -\Omega^2 \frac{\Gamma}{\hbar(\Delta^2 + \Gamma^2)}$. This imaginary part is denoted by $\hbar K_{PA}$, where K_{PA} is the inelastic collision rate co-efficient. A finite inelastic collision rate leads to a finite rate of molecule formation,

$$\gamma_{\text{mol}} = K_{PA} n_b, \quad (4.17)$$

where the rate of molecule formation is limited by the density n_b of bosons, since they are more dilute. Typically, the lifetime of a molecule is much shorter than the time a molecule takes to tunnel out of the system due to its recoil momentum. Therefore the dominant consequence of molecule formation is heating of the gas due to spontaneous decay. The recoil energy of the particles resulting from a spontaneous decay is larger when the excited molecule dissociates into a pair of

atoms than when the molecule decays to a ground molecular state, due to the light mass of ${}^6\text{Li}$ atoms. Therefore we focus on the heating of the gas due to spontaneous dissociation of a molecule into a ${}^6\text{Li}$ and a ${}^{87}\text{Rb}$ atom.

When an excited molecule dissociates, the recoil energy of the ${}^6\text{Li}$ atom is $E_R = \frac{\hbar^2}{2m_{\text{Li}}\lambda^2}$, where λ is the wavelength of the laser used to induce the Feshbach resonance. The rate of spontaneous decay, Γ , of the molecule is typically much shorter than the rate of molecule formation, γ_{mol} . Therefore the heating rate is given by

$$\Gamma_{\text{heat}} = \gamma_{\text{mol}}E_R. \quad (4.18)$$

An experimental run is limited to last until the gas heats up beyond the desired temperature. The temperature scale for observing Kondo physics is given by T_{min} in Eq. (4.15). At this temperature, the duration of an experimental run is $\delta t = \frac{k_B T_{\text{min}}}{\Gamma_{\text{heat}}}$.

During the experiment, collisions between the atoms maintain the gases in thermal equilibrium. The rate of collision between fermions and bosons is $\Gamma_{\text{coll}} = n_b \sigma \langle v \rangle$. Here, the collision rate is limited by the density of bosons, because they are more dilute; σ and $\langle v \rangle$ are the scattering cross-section and average speed of the fermions. The scattering cross-section is related to g as

$$\sigma = \pi \left(\frac{\mu g}{4\pi\hbar^2} \right)^2, \quad (4.19)$$

where $a_s = \frac{\mu g}{4\pi\hbar^2}$ is the scattering length induced by the Feshbach resonance, and μ is the reduced mass of a ${}^6\text{Li}$ - ${}^{87}\text{Rb}$ atom pair. To satisfy two of the three criteria stated earlier, we have to choose the intensity and detuning of the laser such that

$$\begin{aligned} \frac{|Re(g)|n_f\delta t}{\hbar} &= \frac{3}{2\pi E_R} \frac{\Delta}{\Gamma} \sqrt{\frac{n_f\epsilon_F}{228\hbar} \frac{\Omega^2\Delta}{\Delta^2+\Gamma^2}} > 1, \text{ and} \\ \Gamma_{\text{coll}}\delta t &= \frac{3\mu^2}{32\pi^2\hbar^4 E_R} \frac{\Delta v_F}{\Gamma} \sqrt{\frac{n_f\epsilon_F}{228\hbar} \left(\frac{\Omega^2\Delta}{\Delta^2+\Gamma^2} \right)^3} > 1. \end{aligned} \quad (4.20)$$

Here we have used $g_s = \frac{|Re(g)|}{12}$ and $g_n = \frac{Re(g)}{4}$, as produced by our proposal [Eq. (4.10)]. We note that the square of the matrix element for optical coupling, Ω^2 , is

proportional to the intensity of the laser. Ab-initio calculating Ω^2 for a transition requires detailed knowledge of molecular physics. Instead we heuristically calculate Ω^2 at different intensities from available experimental data for resonant photoassociation at a fixed intensity [38]: $K_{\text{PA}} = 4 \times 10^{-11} \text{cm}^3/\text{s}$ at $I = 100 \text{ W/cm}^2$.

In Fig. 4.3, we plot $\frac{|Re(g)|n_f\delta t}{\hbar}$ and $\Gamma_{\text{coll}}\delta t$ as a function of laser intensity and detuning, fixing the fermion density at 10^{14} cm^{-3} . This density is typical in experiments. The bosons' density is irrelevant for calculating $\frac{|Re(g)|n_f\delta t}{\hbar}$ and $\Gamma_{\text{coll}}\delta t$. We also choose a typical optical wavelength $\lambda = 500 \text{ nm}$, and a typical molecular linewidth $\Gamma = 100 \text{ MHz}$ [38]. We require the detuning to be larger than the linewidth of the molecule, and smaller than the fine structure splitting in the molecule. This limits the detuning to lie between 100 MHz and $\sim 10 \text{ GHz}$. In this region of detunings, we find that we require an intensity $I \gtrsim 1 \text{ MW/cm}^2$ to make $|Re(g)|n_f\delta t > 1$ and $\Gamma_{\text{coll}}\delta t > 1$. In particular, at $I = 1 \text{ MW/cm}^2$, $\Gamma_{\text{coll}}\delta t$ is maximized at $\Delta = 220 \text{ MHz}$. For these parameters and $n_b = \frac{n_f}{100}$, $|Re(g)|n_f\delta t = 1.73$, $\Gamma_{\text{coll}}\delta t = 7.7$, $T_{\text{min}} = 0.09T_F = 1.22\mu\text{K}$, and the duration of the experiment is $\delta t = 11\mu\text{s}$. We point out, however, that an intensity of 1 MW/cm^2 is significantly larger than typical intensities used in experiments on ultracold gases. For example, the intensity used to produce an optical Feshbach resonance in Ref. [38] is only 100 W/cm^2 . We also point out that an experimental duration as short as $11\mu\text{s}$ is atypical in ultracold atomic experiments. Such a short experimental duration is not suitable for the scattering experiment we propose to measure an enhanced scattering cross-section. A judicious choice of the resonance, for which the optical couplings Ω are larger, may reduce the intensity required to produce the Feshbach resonance. Another strategy could be to increase the density of fermions using a tight trap.

4.5 Summary

We considered scattering between a spin-1/2 Fermi gas and a dilute spin-unpolarized Bose gas. As an example we considered ${}^6\text{Li}$ and ${}^{87}\text{Rb}$ as our itinerant fermions and bosonic magnetic impurities. We proposed using an optical Feshbach resonance to produce rotationally symmetric interactions between the ${}^6\text{Li}$ and ${}^{87}\text{Rb}$ atoms, which included both spin-dependent Kondo-like and spin-independent density-density interactions. We argued that these interactions would give rise to enhanced Fermi-Bose scattering. We perturbatively calculated the temperature dependence of the momentum transferred to the Fermi gas in a scattering experiment, up to third order in the Bose-Fermi interaction strength. We showed that the temperature dependence of the momentum transferred has a minimum at a characteristic temperature and is logarithmic at low temperatures, characteristic of the Kondo effect and analogous to the behavior of electrical resistance in magnetic alloys.

Our proposal to implement spin-dependent interactions requires overcoming significant experimental challenges such as using high intensity lasers to achieve large interaction strengths. However, overcoming these challenges enable the possibility of exploring exotic phenomena due to Kondo physics. The ground state of a Bose-Fermi mixture with Kondo-type spin-dependent interactions should display interesting correlations, with each boson surrounded by a screening cloud of fermions with opposite spin [1]. These clouds may be observable through various imaging techniques [25, 126, 105]. Similar experiments with bosons confined to a lattice would probe an analog of the Kondo lattice problem.

One can explore other techniques to experimentally produce Kondo-type interactions. For example, optically coupling the electronic triplet states of ${}^6\text{Li}$ - ${}^{87}\text{Rb}$

with excited molecular states will lead to a rotationally asymmetric interaction which also displays Kondo physics. Alternatively, one can realize the Anderson model and Kondo-like situations by trapping impurities in deep potentials [50, 14, 121, 116].

ACKNOWLEDGMENT

We acknowledge support from ARO-MURI Non-equilibrium Many-body Dynamics grant (Grant no. W911NF-14-1-0003). We thank Prof. Kirk Madison for useful discussions, including suggesting the damping of dipole modes as a probe. We thank Todd Rutkowski for independently verifying the calculations in Sec. 4.2. A significant part of the section on experimental considerations came out of discussions with Prof. Mukund Vengalattore.

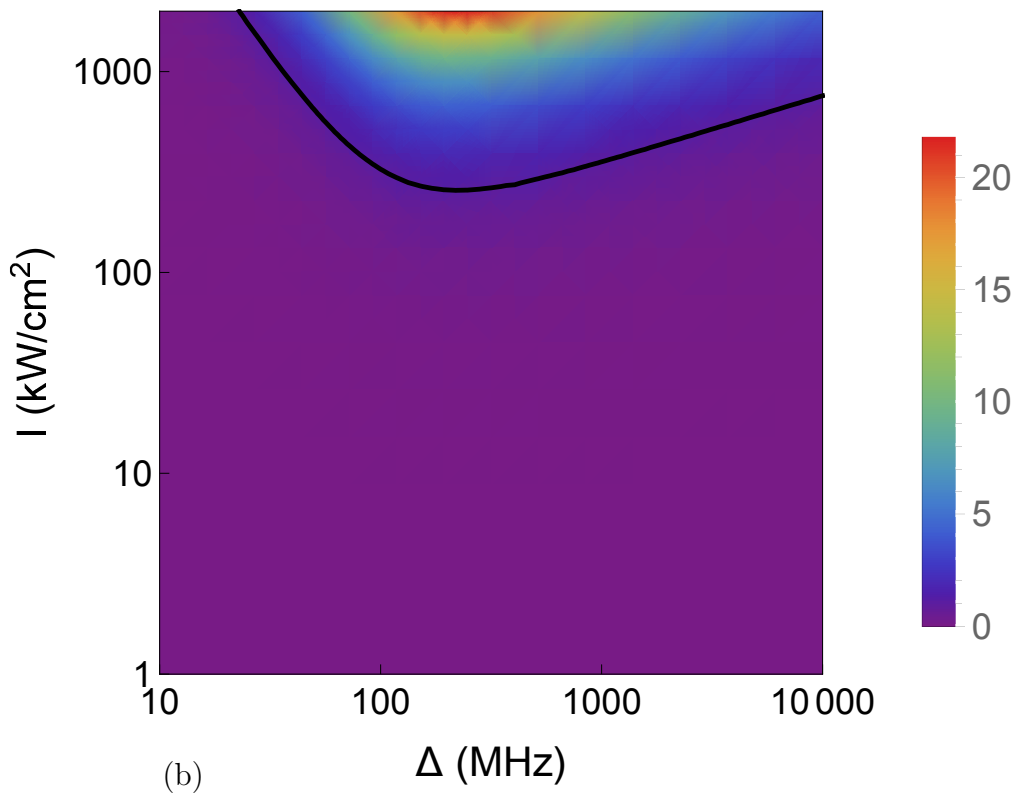
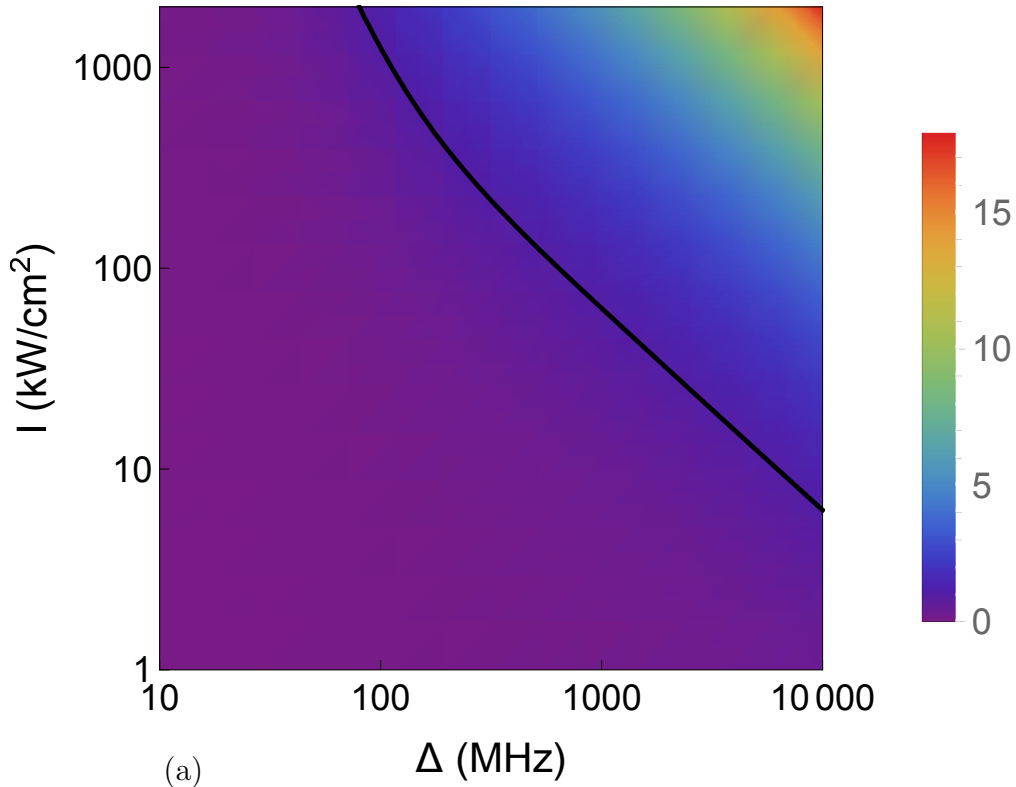


Figure 4.3: (Color online) A density plot of (a) $\frac{|Re(g)|n_f\delta t}{\hbar}$ and (b) $\Gamma_{\text{coll}}\delta t$ as a function of laser intensity and detuning. Here $Re(g)$ is the coherent spin-dependent interaction strength, Γ_{coll} is the collision rate between fermions and bosons, and δt is the allowed experimental duration before the gas significantly heats up. The black lines mark the boundary where $\frac{|Re(g)|n_f\delta t}{\hbar}$ and $\Gamma_{\text{coll}}\delta t$ are larger than 1.

CHAPTER 5

ENGINEERING QUANTUM DIMER MODELS VIA LARGE-SPIN MOTT-INSULATING ULTRACOLD BOSONS

MANY-BODY PHYSICS USING COLD ATOMS

Bhuvanesh Sundar, Ph.D.

Cornell University 2016

We propose an experimental protocol to produce quantum dimer models using ultracold bosonic atoms with a large hyperfine spin confined in a deep optical lattice. We explain how an optical Feshbach resonance can control the strength of interactions in different spin channels, leading to a limit where the low energy Hilbert space is defined by non-overlapping short-range dimers. Solving this model in different lattice geometries yields the columnar phase on a square lattice, and the $\sqrt{12} \times \sqrt{12}$ phase on a triangular lattice. The ground state is unknown on a cubic lattice. We give protocols to measure correlations in the ground state using photoassociation and quantum gas microscopy. Experimentally implementing our proposal would allow us to explore models that have a long history in condensed matter physics, and experimentally resolve theoretically unknown phase diagrams in three dimensional lattices. The work in this chapter was done in collaboration with Prof. Erich Mueller, Prof. Michael Lawler, and Todd Rutkowski. This work is being written up for publication in a peer-reviewed journal at the time of writing this dissertation.

Quantum dimer models—which describe the dynamics of close-packed hard-core dimers on a lattice—have received continued attention since their original proposal by Rokhsar and Kivelson in 1988 [137]. Several factors have motivated these studies, including an intimate connection to Anderson’s resonating valence bond description of high- T_c superconductivity [3, 90], the appearance of quantum critical points [139, 143, 156], topological order and fractionalized excitations [79, 160, 112, 142, 51], their mapping to lattice gauge theories [110, 108, 106], and their potential applications in quantum computation [68, 77]. In these models, interplay between quantum fluctuations, hard-core constraints, and the lattice geometry allows this rich variety of phenomena to emerge from a surprisingly simple physical picture. Unfortunately, quantum dimer models are believed to be cleanly realized in very few solid state systems, and thus far their study has remained mostly theoretical. Here we present a proposal to realize a range of dimer models in a gas of bosons in an optical lattice.

We consider a gas of bosonic atoms with no orbital angular momentum, $l = 0$, and relatively large hyperfine spin f , in an optical lattice. Candidate atoms could be ^{52}Cr with $f = 3$, or ^{87}Rb with $f = 2$. By tuning the lattice depth and trapping potential one can drive the system into a Mott insulating state with one atom per site [70] — effectively yielding immobile spins on each site. These spins interact via a virtual super-exchange process [4]. We propose manipulating these super-exchange interactions by optically coupling pairs of atoms to an excited $L = 1, S = 0$ molecular state. When tuned sufficiently off-resonance, this optical coupling favors the formation of nearest neighbor hyperfine singlets, which we refer to as dimers. In the limit of large f , the dimers are monogamous and orthogonal: A state where site i forms a singlet with site j is orthogonal to one in which i forms a singlet with k , as long as $j \neq k$. The resulting theory has the form

of a dimer model, whose ground state depends on the geometry of the lattice. We find the $\sqrt{12} \times \sqrt{12}$ phase on a triangular lattice [132]. However, the phases on a 2D square and a 3D cubic lattice are a matter of contention [139, 92, 10], which these experiments could resolve. We discuss quantum gas microscopy and photoassociation protocols for detecting these various phases.

There have been proposals to observe related physics in cold atom experiments, including crystallized dimer phases [33, 168, 67, 172, 42], resonating plaquette phases [21, 165, 151], and dimer liquid phases [62, 18, 144, 146, 138]—all hallmarks of the quantum dimer model. However, these studies involve different underlying physical mechanisms, and did not explore mappings of their systems onto quantum dimer models. In this chapter, we show that quantum dimer models describe the effective low-energy interactions of large-spin Mott insulating bosonic atoms in a unit-filled optical lattice, when the spin-dependent interactions are dominated by scattering processes in the spin-singlet channel.

To derive a quantum dimer model for our cold atom system, we begin with a tight-binding model for bosons in an optical lattice, which includes spin-dependent interactions. We write this model as [148]

$$\hat{H} = -J \sum_{\langle ij \rangle} \sum_{m=-f}^f \left(\hat{b}_{i,m}^\dagger \hat{b}_{j,m} + \text{H.c.} \right) + \sum_{F=0,2,\dots}^{2f} U_F \sum_{M=-F}^F \hat{A}_i^{F,M\dagger} \hat{A}_i^{F,M}, \quad (5.1)$$

where i runs over all sites of the lattice, and $\langle ij \rangle$ is a sum over all distinct nearest neighbor pairs. The $\hat{b}_{i,m}^\dagger$ ($\hat{b}_{i,m}$) operators create (annihilate) a bosonic atom at lattice site i with hyperfine spin f and spin projection m , while the $\hat{A}_i^{F,M\dagger}$ ($\hat{A}_i^{F,M}$) operators create (annihilate) a pair of bosonic atoms on site i in total angular momentum state F with total projection M . These pair operators are related to the bosonic operators via the relation $\hat{A}_i^{F,M\dagger} = \sum_m C_{m,M-m}^{F,M} \hat{b}_{i,m}^\dagger \hat{b}_{i,M-m}$, where $C_{m,m'}^{F,M} = \langle f, m; f, m' | F, M \rangle$ are Clebsch-Gordan coefficients. The kinetic energy term in Eq.

(5.1)—parameterized by the positive constant J —models the tunneling of bosons between neighboring lattice sites. The on-site potential energy—described by the set of parameters U_F —models the local spin-dependent s -wave scattering. The interaction U_F includes contributions from both the intrinsic interaction U_F^{bg} , and an optical Feshbach resonance, U_F^{Fesh} , which we describe below. The scattering occurs through only the even total-spin channels due to Bose statistics of the atoms. We choose atomic species for which the intrinsic interaction $U_F^{\text{bg}} > 0$. Typically, U_F^{bg} is uniform among all the even spin channels. As we explain below, U_F^{Fesh} is not.

We induce an optical Feshbach resonance between pairs of atoms by shining a laser tuned near a transition to an excited molecular state, labeled by orbital angular momentum L , electronic spin S , and total electronic angular momentum J . The nuclear angular momentum is not important as long as the detuning of the laser is large compared to the hyperfine splitting. Since the atoms are chosen to have no orbital angular momentum, the only allowed optical transitions are to $L = 1$. When the detuning of the laser is large compared to the linewidth of the molecular state, second order perturbation theory gives rise to a local spin-dependent pairwise interaction. As explained in Ref. [149], the induced interaction will be of the form in Eq. (5.1) if we choose a molecule with $S = 0$. In this case, there is no spin-orbit coupling in the molecular state, and therefore in the second order process, the photon’s angular momentum decouples from the atoms’. The resulting spin-dependent interaction is of the form $U_F^{\text{Fesh}} = \frac{\Omega^2}{\delta} \alpha_F$. The matrix element Ω^2 is proportional to the intensity of the laser, and δ is the detuning from the molecular transition. The coefficient α_F is the square of the overlap between the electronic spin singlet ($S = 0$) and the hyperfine state with total spin F [104]:

$$\alpha_F = |\langle (s_1 s_2)S(i_1 i_2)I; F | (s_1 i_1)f_1(s_2 i_2)f_2; F \rangle|^2. \quad (5.2)$$

Here, $s_1 = s_2 = s$ are the electronic spin of the atoms, $i_1 = i_2 = i$ are the nuclear spin of the atoms, $f_1 = f_2 = f$ are the hyperfine spin of the atoms, and the atoms have no orbital angular momentum, $l_1 = l_2 = 0$. The parameters S , I and F describe the state of a pair of atoms: $S = 0$ because the atoms only couple to the molecular state when they are in a singlet, in which case $I = F$. The notation $(j_1 j_2)j$ denotes that the total spin j is the sum of spins j_1 and j_2 . The coefficients α_F [in Eq. (5.2)] are related to Wigner $9j$ symbols. The results for α_F are different for different atomic species. For alkali atoms, which have $s = 1/2$, we calculate α_F from straightforward recursion relations, derived by using Clebsch Gordan coefficients to expand states of fixed S in terms of hyperfine states. We find

$$\begin{aligned}\alpha_{2f} &= \frac{2f+1}{4(i+1/2)^2}, \\ \alpha_{2f-2} &= \frac{3f}{2(i+1/2)^2}, \\ &\vdots \\ \alpha_0 &= \frac{2f+1}{4(i+1/2)}.\end{aligned}$$

These results are valid for both the ground state ($f = i - 1/2$) and the excited state ($f = i + 1/2$) manifolds. For ^{52}Cr , which has $l = i = 0$, the values of α_F are

$$\alpha_F = \delta_{F,0},$$

where δ is the Kronecker delta symbol. An important feature of the coefficients α_F in these two cases is that they decrease in magnitude as F increases.

We tune the Feshbach coupling and detuning such that $U_F^{\text{bg}} \simeq U_0^{\text{Fesh}}$. In this limit, the total interaction coefficients U_F form an increasing sequence, and in particular, $U_{F \neq 0} \gg U_0$. We consider a deep lattice where $J \ll U_0$, and by extension $J \ll U_F$. This suppresses tunneling, and the atoms only virtually hop between

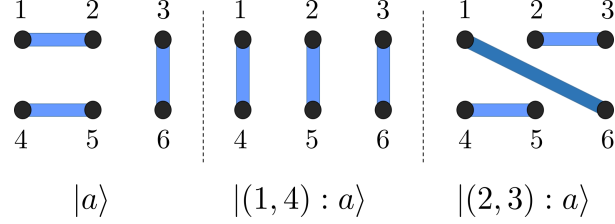


Figure 5.1: (Color online) Examples of singlet cover states. The numbers label the lattice sites, while connected sites represent a spin singlet between the atoms on those sites. In this example, $|a\rangle = \hat{A}_{1,2}^\dagger \hat{A}_{4,5}^\dagger \hat{A}_{3,6}^\dagger |0\rangle$. The notation $|(i, j) : a\rangle$ denotes a state where sites i and j are paired in a singlet, the original partners of i and j in $|a\rangle$ are paired in another singlet, and all the other bonds in $|a\rangle$ are left unchanged. This notation is used in Appendix D to derive an effective dimer model [Eq. (5.6)].

neighboring lattice sites. Taking $U_0 \ll U_{F \neq 0}$ causes the virtual hopping to be predominantly in the hyperfine spin singlet channel. At unit filling, the effective Hamiltonian at second order in the tunneling strength is then

$$\hat{H}_{\text{eff}} = -\frac{2J^2}{U_0} \sum_{\langle ij \rangle} \hat{A}_{ij}^{00\dagger} \hat{A}_{ij}^{00}, \quad (5.3)$$

where $\hat{A}_{ij}^{00} = \sum_m C_{m,-m}^{00} \hat{b}_{im} \hat{b}_{j,-m}$ annihilates a pair of bosons at sites i and j in a hyperfine spin singlet. Hereafter we drop the superscripts, and refer to this operator as \hat{A}_{ij} .

The low energy eigenstates of Eq. (5.3), with one atom per site, can be written as a superposition of singlet coverings. Each singlet cover is written as

$$|a\rangle = \prod_{(i,j) \in a} \hat{A}_{ij}^\dagger |0\rangle, \quad (5.4)$$

where (i, j) refers to a singlet bond between sites i and j , which are not necessarily nearest neighbors. In Eq. (5.4), each lattice site appears only once in the product over bonds. Some examples of singlet coverings are illustrated in Fig. 5.1. As explicitly shown in Appendix D, this subspace of states is closed under the operation of \hat{H}_{eff} .

The singlet coverings defined in Eq. (5.4) are not orthogonal. Their overlap $S_{a,b} = \langle a|b \rangle$ may be calculated through their transition graph, as shown in Fig. D.1 in Appendix D. We follow Ref. [137] and construct an orthogonal basis from these non-orthogonal singlet coverings,

$$|\bar{a}\rangle = \sum_b \left(\sqrt{S^{-1}} \right)_{a,b} |b\rangle. \quad (5.5)$$

We call the orthogonal basis states $|\bar{a}\rangle$ as dimer states. For large f , the overlap matrix S is the identity to leading order.

If we take $f \rightarrow \infty$, the dimer covers $|\bar{a}\rangle$ are eigenstates of \hat{H}_{eff} with energy $E_a = \frac{-2J^2}{U_0} N_a$, where N_a is the number of nearest neighbor bonds in $|a\rangle$. In this limit, the states consisting only nearest neighbor bonds span a degenerate ground state manifold. We use second order degenerate perturbation theory in $(2f+1)^{-1}$ to calculate an effective model in this space. On a square, triangular, or a cubic lattice, we find

$$\hat{H}_{\text{QDM}} = \sum -t (|=\rangle \langle ||| + \text{H.c.}) + V (|=\rangle \langle =| + ||\rangle \langle ||) - t' (|=| \rangle \langle |=| + \text{H.c.}). \quad (5.6)$$

The first term in this effective theory—parameterized by t —models a rotation of two parallel bonds within a four-site plaquette from a vertical to a horizontal configuration, or vice versa. Such four-site plaquettes with two parallel bonds are called flippable plaquettes. The second term—parameterized by V —models an effective interaction between two parallel bonds in a flippable plaquette. The third term—parameterized by t' —models a resonance for three bonds within a six-site plaquette. The effective dimer model on a hexagonal lattice has similar terms, but acting on larger plaquettes. In this lattice, the smallest ring exchange involves three bonds, and therefore its amplitude t is of $\mathcal{O}((2f+1)^{-2})$. Table 5.1 lists the parameters t, t' and V for different lattice geometries, and the expected ground state.

We point out that our proposal to produce a quantum dimer model using cold atoms has significant advantages over electronic systems. First, using atoms with a large spin allows for a controlled expansion in terms of a parameter, $(2f + 1)^{-1}$, which can be made relatively small. This is in contrast to spin-1/2 electronic systems, where orthogonality issues are neglected and $1/f$ expansions are made despite the lack of a small parameter. Second, tuning between lattice geometries is relatively easy in systems with cold atoms [73, 97, 164]. Third, dimer models studied in electronic systems typically have $t' = 0$; our proposal produces a richer model with $t' \neq 0$.

Lattice geometry	$\frac{t}{J^2/U_0}$	$\frac{V}{J^2/U_0}$	$\frac{t'}{J^2/U_0}$	Ground state at large f
Square lattice	$\frac{4}{2f+1}$	$\frac{8}{(2f+1)^2}$	$\frac{8}{(2f+1)^2}$	unresolved
Triangular lattice	$\frac{8(f+1)}{(2f+1)^2}$	$\frac{14}{(2f+1)^2}$	$\frac{8}{(2f+1)^2}$	$\sqrt{12} \times \sqrt{12}$
Cubic lattice	$\frac{4}{2f+1}$	$\frac{8}{(2f+1)^2}$	$\frac{8}{(2f+1)^2}$	unknown
Honeycomb lattice	$\frac{12}{(2f+1)^2}$	$\mathcal{O}(1/f^4)$	$\mathcal{O}(1/f^4)$	plaquette

Table 5.1: List of ring exchange amplitudes and bond interactions obtained from Eq. (5.3), in different lattice geometries.

The effective model for our system [Eq. (5.6)] has a rich phase diagram, which has been well explored along $t' = 0$ in a number of geometries [107, 139, 112, 108, 111, 109, 106, 132, 169, 92, 150, 131, 10]. For 2D bipartite lattices with $t' = 0$, one finds only valence bond solid phases. Dimer liquid phases are found in 3D, and non-bipartite 2D lattices. The phase diagram at finite t' is less explored [117].

The valence bond solid phases described in the literature fall into four types: columnar, plaquette, mixed, and staggered. The columnar phase is built from vertical columns of horizontal parallel bonds, or vice versa. In the plaquette phase, dimer bonds resonate between different configurations inside a multi-site unit cell. For example, on a square lattice, the plaquette phase has a unit cell with four lattice

sites; two parallel bonds resonate between horizontal and vertical configurations inside a plaquette. The plaquette phases on a triangular lattice have larger unit cells. The mixed phase is a hybrid between the columnar and plaquette phases. The staggered phase has no flippable plaquettes. The columnar phase is favored at large negative V , and the staggered phase at large positive V . There is some contention about the presence of plaquette and mixed phases as the ground state on a square lattice, and the location of the phase boundaries [10]. In nearly all theoretical analyses, our model on a square lattice yields a columnar phase as $f \rightarrow \infty$. Experiments on ultracold atoms with large f should be able to resolve the theoretical debates. On the triangular lattice, as $f \rightarrow \infty$, we expect to see a plaquette phase, called the $\sqrt{12} \times \sqrt{12}$ phase, which has a 12-site unit cell [132].

We propose to characterize the ground state of our model by measuring the dimer-dimer correlation function $\langle \hat{A}_{ij}^\dagger \hat{A}_{ij} \hat{A}_{kl}^\dagger \hat{A}_{kl} \rangle$. We provide a protocol to experimentally image dimer bonds and measure dimer-dimer correlations. Researchers have calculated dimer-dimer correlations for the ground states of quantum dimer models (with $t' = 0$) in different lattice geometries [106, 132, 169, 92]. We numerically calculate the correlations in our system for both large and realistic values of f .

To image dimer bonds, we propose shining an additional weak near-resonant photoassociation laser on the system, tuned near a molecular state with angular momenta $L = 1, S = 0$. The resonant light drives a pair of neighboring atoms in an electronic spin singlet, $S = 0$, to the molecular state via a second order process: tunneling brings two neighboring atoms to the same site, and absorption of a resonant laser photon produces an excited molecule. The excited molecule spontaneously decays back into a pair of atoms after a short lifetime. The resulting

atoms have a large kinetic energy, and leave the system. We propose to image the system with a quantum gas microscope [9, 75]. The image has empty neighboring sites wherever a neighboring pair of atoms absorbed a resonant photon to form a molecule. These neighboring atoms may or may not have been entangled in a dimer before they absorbed a photon. Absorption of a photon by unentangled atoms leads to false positives in our scheme to image dimer bonds. However, entangled atoms and unentangled atoms absorb photons at different rates. Calculation of the rate of absorption of photons by entangled atoms, and the related problem of absorption rate of entangled photons, is a rich field of study [45, 56, 71, 115, 134, 171]. We leave the calculation of the photon absorption rate by a pair of atoms entangled in a dimer versus an unentangled pair to a future study. Here we hypothesize that for atoms with a large spin, an entangled pair of atoms absorbs photons at a much higher rate than an unentangled pair. In this case, most of the neighboring empty sites in the image taken by the quantum gas microscope were occupied by atoms entangled in a dimer. In this way, a fraction of the dimer bonds can be imaged in a system consisting of atoms with a large spin. Correlations between two dimers can be extracted by analyzing the data from multiple realizations.

We simulate our system numerically by computing the ground state of the model in Eq. (5.3). The natural basis for a numerical simulation is spanned by the non-orthogonal singlet coverings. In our numerics, we do not rely on the large f approximation. Neither do we restrict ourselves to the low energy sector with only nearest neighbor dimer bonds. We are, however, limited to a small system with no more than 16 lattice sites. We exactly diagonalize the Hamiltonian [in Eq. (5.3)] to compute the ground state. We then compute the dimer-dimer correlation function $\langle \hat{A}_{ij}^\dagger \hat{A}_{ij} \hat{A}_{kl}^\dagger \hat{A}_{kl} \rangle$.

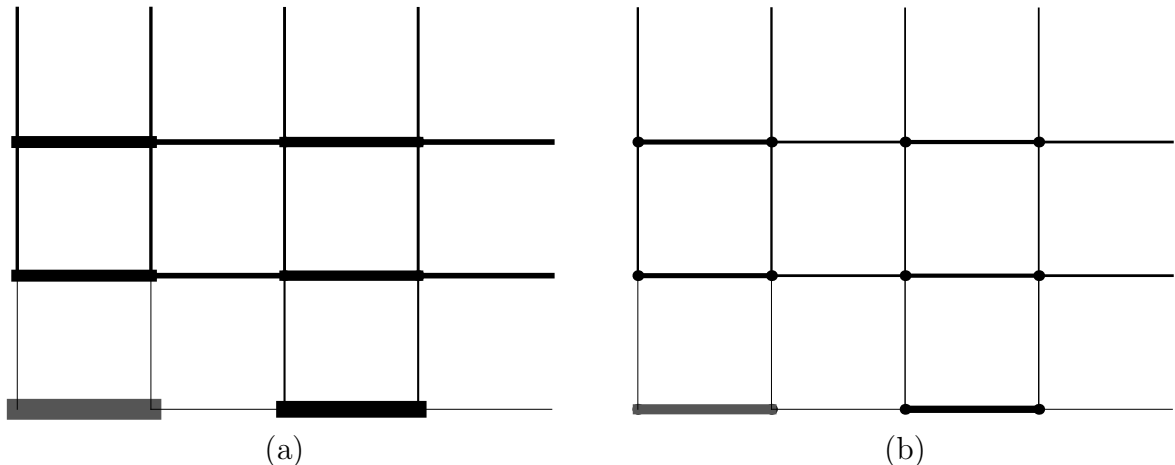


Figure 5.2: Dimer-dimer correlations on a square lattice with periodic boundary conditions, for (a) $f = 100$ and (b) $f = 3$. The reference dimer is marked grey in the lower left corner. The thickness of the lines is proportional to the strength of correlation. (Color online)

We plot the correlation between a bond (i, j) and a bond (k, l) on a square lattice for two different values of f in Fig. 5.2, where the bond (i, j) is fixed at the lower left corner, and the bond (k, l) is varied. For a large value of f , we find correlations consistent with a columnar phase. We also calculate correlations for a typical atomic species, ^{52}Cr , which has $f = 3$. The correlations are weaker in this case, but still indicative of a columnar phase.

We also compute the ground state of our model on a triangular lattice. For this lattice, we anticipate the ground state to be the $\sqrt{12} \times \sqrt{12}$ phase [132]. Therefore we assume our system to have the shape of a unit cell in the $\sqrt{12} \times \sqrt{12}$ phase. We again plot the correlation between a bond (i, j) and a bond (k, l) on a triangular lattice for two different values of f in Fig. 5.3. For both large and experimentally accessible values of f , we find correlations consistent with the $\sqrt{12} \times \sqrt{12}$ phase.

In summary, we propose an experimental protocol to produce quantum dimer models using ultracold bosonic atoms with a large hyperfine spin confined in a

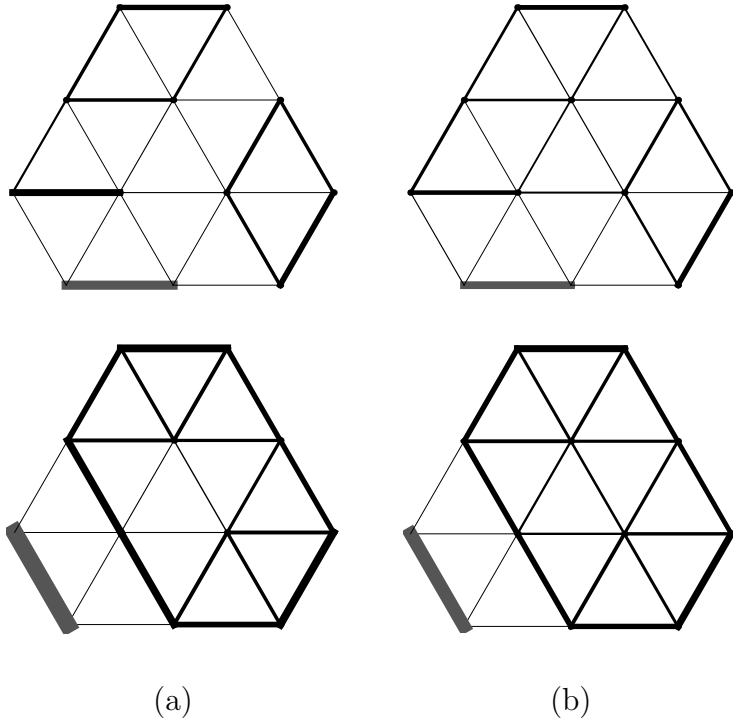


Figure 5.3: Dimer-dimer correlations on a triangular lattice for (a) $f = 100$ and (b) $f = 3$. The reference dimer is marked in grey. The thickness of the lines is proportional to the strength of correlation.

deep optical lattice. We show that the inter-particle interactions produced by an optical Feshbach resonance lead to a rich dimer model. For bosonic atoms with a large spin, the ground state of our model is the columnar phase on a square lattice, and the $\sqrt{12} \times \sqrt{12}$ phase on a triangular lattice. The ground state on a 3D cubic lattice is a matter of theoretical contention. We present protocols to detect the ground state by experimentally measuring dimer-dimer correlations via a combination of photoassociation and quantum gas microscopy. We computed dimer-dimer correlations for various spins on a small system, finding that the expected large f results persist into the experimentally accessible range of spins. Experimentally implementing our proposal will provide a method to produce a quantum dimer model in a clean way with a controllable small parameter, namely $(2f+1)^{-1}$. It will allow us to explore the phase diagram of quantum dimer models,

which is an iconic problem and has a long history in condensed matter physics. Moreover, our proposal will allow us to experimentally resolve theoretical debates regarding the phase diagrams in three dimensional lattices.

ACKNOWLEDGMENT

This material was based upon work supported by the National Science Foundation Grant No. PHY-1508300. We thank Prof. Mukund Vengalattore for discussions regarding the calculation of the false positive rate while imaging dimer bonds using resonant photoassociation.

CHAPTER 6
**SEMICLASSICAL TOOLS TO STUDY THE DYNAMICS OF A
FERMI GAS DURING A TIME-OF-FLIGHT EXPANSION**

MANY-BODY PHYSICS USING COLD ATOMS

Bhuvanesh Sundar, Ph.D.

Cornell University 2016

We develop semiclassical tools to calculate the dynamics of a Fermi gas during a time-of-flight expansion. We use Wigner functions to model a superfluid Fermi gas. We show that the equations of motion for the Wigner functions resemble semiclassical Boltzmann equations. We show that these equations map to the Gross Pitaevskii equation in the limit of strongly interacting fermions. We compare the dynamics obtained by numerically integrating the semiclassical Boltzmann equations to those obtained by integrating the Gross Pitaevskii equation. Our calculations are useful for all experiments involving a time-of-flight expansion of an ultracold gas. The work in this chapter was done in collaboration with Prof. Erich Mueller.

6.1 Introduction

Dynamics are ubiquitous in experiments on ultracold atomic gases. Some of the dynamical phenomena that ultracold atom researchers are interested in include quenches [133, 103, 43, 66, 20, 23, 128], periodic driving [125, 27, 130, 32, 89, 88, 40, 41, 157], transport phenomena [85], stability of condensates [40, 41, 157, 27, 89, 88, 32, 130], thermalization [43, 76, 147, 34], prethermalization [12, 60], and time-of-flight expansions [29, 166, 100]. Researchers lack a simple approach to calculate the dynamics of a superfluid Fermi gas. Here, we attempt to rectify this problem by introducing a novel semiclassical approximation. We use this approach to model an ultracold superfluid Fermi gas in a harmonic trap. We calculate the properties of the Fermi gas as it expands when the trap is released. This particular study is motivated by several experiments which explore dynamics of solitons in Fermi gases [167, 120, 8]. We believe that this approach can be used to calculate signatures in the density of an expanding spin-imbalanced Fermi gas to detect the Fulde-Ferrel-Larkin-Ovchinnikov phase [54, 87, 95, 96]. We find that the results of our semiclassical approach are accurate for strongly interacting fermions, but suffer from numerical instabilities for weakly interacting fermions.

Dynamics of superfluid Fermi gases are well-modeled by time-dependent Bogoliubov-de-Gennes equations [31]. However, integrating time-dependent Bogoliubov-de-Gennes equations can be difficult. In the strongly interacting limit, the dynamics of the Fermi gas are modeled well by the Gross-Pitaevskii equation, which is a simpler equation to integrate [61, 46]. In this chapter, we develop semiclassical tools to calculate the dynamics of a superfluid Fermi gas for both weak and strong interactions, during a time-of-flight expansion. We calculate and numerically integrate the equations of motion for the Wigner function [129] and an

anomalous Wigner function for a Fermi gas. We show that the equations of motion of the Wigner functions map to the Gross-Pitaevskii equation in the strongly interacting limit of the Fermi gas. Our technique is complementary to modeling the dynamics via time-dependent Bogoliubov-de-Gennes equations. We also numerically integrate the equations of motion for the Wigner functions of a weakly interacting Fermi gas, during a time-of-flight expansion. At short times, our numerical results agree with results obtained from Bogoliubov-de-Gennes equations. We discuss limitations of our semiclassical approach for a weakly interacting Fermi gas at long times.

This chapter is organized as follows. In Sec. 6.2, we introduce the formalism for Wigner functions. In Sec. 6.3, we calculate the Wigner functions for a homogeneous Fermi gas with no trap. In Sec. 6.4, we calculate the Wigner functions for a strongly interacting inhomogeneous Fermi gas, and show that the equation of motion for the order parameter is the Gross Pitaevskii equation. In Sec. 6.5, we explore the dynamics of the gas during a time-of-flight expansion. We compare the results of our semiclassical approach with those obtained from Gross-Pitaevskii and Bogoliubov-de-Gennes equations. We conclude in Sec. 6.6.

6.2 Formalism

An interacting Fermi gas in a harmonic trap is modeled by a Hamiltonian

$$\hat{H} = \int d^3\vec{r} \sum_{\sigma} \hat{\psi}_{\sigma}^{\dagger}(\vec{r}, t) \left(\frac{-\hbar^2 \nabla^2}{2m} + V(\vec{r}) - \mu \right) \hat{\psi}_{\sigma}(\vec{r}, t) + U \hat{\psi}_{\uparrow}^{\dagger}(\vec{r}, t) \hat{\psi}_{\uparrow}(\vec{r}, t) \hat{\psi}_{\downarrow}^{\dagger}(\vec{r}, t) \hat{\psi}_{\downarrow}(\vec{r}, t), \quad (6.1)$$

where $V(\vec{r}) = \frac{1}{2}m\omega^2 r^2$ is the trapping potential. Here, $\hat{\psi}_{\sigma}(\vec{r}, t)$ is the fermionic field operator in real space in the Heisenberg picture, and U is the contact interaction

strength. In reality, fermions have a finite range of interaction. The renormalized physical interaction strength is g , given by

$$\frac{1}{g} = \frac{1}{U} + \frac{1}{(2\pi\hbar)^3} \int \frac{d^3\vec{p}}{2\epsilon_p}, \quad (6.2)$$

where $\epsilon_p = p^2/2m$ is the dispersion for non-interacting free particles. The three dimensional scattering length a_s is related to g as $g = \frac{4\pi\hbar^2 a_s}{m}$. We self-consistently define a mean field order parameter

$$\Delta(\vec{r}, t) = U \left\langle \hat{\psi}_\downarrow(\vec{r}, t) \hat{\psi}_\uparrow(\vec{r}, t) \right\rangle. \quad (6.3)$$

The mean field Hamiltonian modeling the gas is

$$\begin{aligned} \hat{H} = \int d^3\vec{r} \sum_{\sigma} \hat{\psi}_{\sigma}^{\dagger}(\vec{r}, t) & \left(\frac{-\hbar^2 \nabla^2}{2m} + V(\vec{r}) - \mu \right) \hat{\psi}_{\sigma}(\vec{r}, t) + \Delta(\vec{r}, t) \hat{\psi}_{\uparrow}^{\dagger}(\vec{r}, t) \hat{\psi}_{\downarrow}^{\dagger}(\vec{r}, t) \\ & + \Delta^*(\vec{r}, t) \hat{\psi}_{\downarrow}(\vec{r}, t) \hat{\psi}_{\uparrow}(\vec{r}, t) - \frac{|\Delta(\vec{r}, t)|^2}{U}. \end{aligned} \quad (6.4)$$

The Heisenberg equation of motion for the field operators is

$$i\hbar\partial_t \hat{\psi}(\vec{r}, t) = [\hat{\psi}(\vec{r}, t), \hat{H}]. \quad (6.5)$$

In the mean field theory, this Heisenberg equation of motion and its hermitian conjugate leads to the time-dependent Bogoliubov-de-Gennes equations:

$$i\hbar\partial_t \begin{pmatrix} \hat{\psi}_{\uparrow}(\vec{r}, t) \\ \hat{\psi}_{\downarrow}^{\dagger}(\vec{r}, t) \end{pmatrix} = \begin{pmatrix} -\frac{\hbar^2 \nabla^2}{2m} + V(\vec{r}) - \mu & \Delta(\vec{r}, t) \\ -\Delta^*(\vec{r}, t) & \frac{\hbar^2 \nabla^2}{2m} - V(\vec{r}) + \mu \end{pmatrix} \begin{pmatrix} \hat{\psi}_{\uparrow}(\vec{r}, t) \\ \hat{\psi}_{\downarrow}^{\dagger}(\vec{r}, t) \end{pmatrix}. \quad (6.6)$$

As mentioned earlier, the dynamics of the Fermi gas are captured well by these equations. In this section, we introduce an alternative formalism to compute the dynamics of a Fermi gas. Later, we will compare the results obtained by numerically integrating the time-dependent Bogoliubov-de-Gennes equations [Eq. (6.6)] with those obtained from our alternative formalism.

The quantum Wigner function for a Fermi gas is defined as

$$W_\sigma(\vec{r}, \vec{p}, t) = \int \frac{d^3\vec{s}}{(2\pi\hbar)^3} \left\langle \hat{\psi}_\sigma^\dagger \left(\vec{r} + \frac{\vec{s}}{2}, t \right) \hat{\psi}_\sigma \left(\vec{r} - \frac{\vec{s}}{2}, t \right) \right\rangle e^{-i\vec{p}\cdot\vec{s}/\hbar}. \quad (6.7)$$

The Wigner function can also be written as:

$$W_\sigma(\vec{r}, \vec{p}, t) = \int \frac{d^3\vec{q}}{(2\pi\hbar)^3} \left\langle \hat{\psi}_\sigma^\dagger \left(\vec{p} + \frac{\vec{q}}{2}, t \right) \hat{\psi}_\sigma \left(\vec{p} - \frac{\vec{q}}{2}, t \right) \right\rangle e^{i\vec{q}\cdot\vec{r}/\hbar}, \quad (6.8)$$

where $\hat{\psi}_\sigma(\vec{p}, t) = \int d^3\vec{r} \hat{\psi}_\sigma(\vec{r}, t) e^{i\vec{p}\cdot\vec{r}/\hbar}$ is the fermionic field operator in momentum space. The Wigner function is always real. Observables such as the density of the gas can be calculated from the Wigner function:

$$\begin{aligned} n_\sigma(\vec{r}, t) &= \int d^3\vec{p} W_\sigma(\vec{r}, \vec{p}, t), \\ \tilde{n}_\sigma(\vec{p}, t) &= \int d^3\vec{r} W_\sigma(\vec{r}, \vec{p}, t). \end{aligned} \quad (6.9)$$

In this sense, the Wigner function is a semiclassical analog of the phase space density of a Fermi gas. However, it is important to note that W_σ is a strictly quantum mechanical distribution which can take both positive and negative values. For example, negative Wigner functions are indicative of entanglement in the system (see [65] for example).

We also define an anomalous Wigner function

$$\begin{aligned} F(\vec{r}, \vec{p}, t) &= \int \frac{d^3\vec{s}}{(2\pi\hbar)^3} \left\langle \hat{\psi}_\downarrow \left(\vec{r} + \frac{\vec{s}}{2}, t \right) \hat{\psi}_\uparrow \left(\vec{r} - \frac{\vec{s}}{2}, t \right) \right\rangle e^{-i\vec{p}\cdot\vec{s}/\hbar} \\ &= \int \frac{d^3\vec{q}}{(2\pi\hbar)^3} \left\langle \hat{\psi}_\downarrow \left(\frac{\vec{q}}{2} - \vec{p}, t \right) \hat{\psi}_\uparrow \left(\frac{\vec{q}}{2} + \vec{p}, t \right) \right\rangle e^{i\vec{q}\cdot\vec{r}/\hbar}. \end{aligned} \quad (6.10)$$

The order parameter is related to the anomalous Wigner function as

$$\Delta(\vec{r}) = U \int d^3\vec{p} F(\vec{r}, \vec{p}, t). \quad (6.11)$$

Using the Heisenberg equations of motion for the field operators, $i\hbar\partial_t\hat{\psi}(\vec{r}, t) =$

$[\hat{\psi}(\vec{r}, t), \hat{H}]$, we calculate the equations of motion for $W_\sigma(\vec{r}, \vec{p}, t)$ and $F(\vec{r}, \vec{p}, t)$:

$$\begin{aligned}
\partial_t W_\uparrow &= \frac{\vec{p}}{m} \cdot \nabla W_\uparrow - \nabla V \cdot \nabla_p W_\uparrow + \frac{1}{i\hbar} \int \frac{d^3 \vec{s}}{(2\pi\hbar)^3} e^{-i\vec{p}\cdot\vec{s}/\hbar} \\
&\quad \times \left(\Delta \left(\vec{r} - \frac{\vec{s}}{2}, t \right) \left\langle \hat{\psi}_\uparrow^\dagger \left(\vec{r} + \frac{\vec{s}}{2}, t \right) \hat{\psi}_\downarrow \left(\vec{r} - \frac{\vec{s}}{2}, t \right) \right\rangle \right. \\
&\quad \left. - \Delta^* \left(\vec{r} + \frac{\vec{s}}{2}, t \right) \left\langle \hat{\psi}_\downarrow \left(\vec{r} + \frac{\vec{s}}{2}, t \right) \hat{\psi}_\uparrow \left(\vec{r} - \frac{\vec{s}}{2}, t \right) \right\rangle \right) \\
\partial_t W_\downarrow &= \frac{\vec{p}}{m} \cdot \nabla W_\downarrow - \nabla V \cdot \nabla_p W_\downarrow + \frac{1}{i\hbar} \int \frac{d^3 \vec{s}}{(2\pi\hbar)^3} e^{-i\vec{p}\cdot\vec{s}/\hbar} \\
&\quad \times \left(\Delta \left(\vec{r} - \frac{\vec{s}}{2}, t \right) \left\langle \hat{\psi}_\uparrow^\dagger \left(\vec{r} - \frac{\vec{s}}{2}, t \right) \hat{\psi}_\downarrow^\dagger \left(\vec{r} + \frac{\vec{s}}{2}, t \right) \right\rangle \right. \\
&\quad \left. - \Delta^* \left(\vec{r} + \frac{\vec{s}}{2}, t \right) \left\langle \hat{\psi}_\downarrow \left(\vec{r} - \frac{\vec{s}}{2}, t \right) \hat{\psi}_\uparrow \left(\vec{r} + \frac{\vec{s}}{2}, t \right) \right\rangle \right) \\
i\hbar \partial_t F &= \left(2(\epsilon_p - \mu + V(\vec{r})) - \frac{\hbar^2}{4m} \nabla^2 - \frac{m\omega^2 \hbar^2}{4} \nabla_p^2 \right) F + \frac{\Delta}{(2\pi\hbar)^3} - \int \frac{d^3 \vec{s}}{(2\pi\hbar)^3} e^{-i\vec{p}\cdot\vec{s}/\hbar} \\
&\quad \times \left(\Delta \left(\vec{r} - \frac{\vec{s}}{2}, t \right) \left\langle \hat{\psi}_\downarrow^\dagger \left(\vec{r} - \frac{\vec{s}}{2}, t \right) \hat{\psi}_\downarrow \left(\vec{r} + \frac{\vec{s}}{2}, t \right) \right\rangle \right. \\
&\quad \left. + \Delta \left(\vec{r} + \frac{\vec{s}}{2}, t \right) \left\langle \hat{\psi}_\uparrow^\dagger \left(\vec{r} + \frac{\vec{s}}{2}, t \right) \hat{\psi}_\uparrow \left(\vec{r} - \frac{\vec{s}}{2}, t \right) \right\rangle \right). \tag{6.12}
\end{aligned}$$

Here, ∇ denotes spatial gradient, and ∇_p denotes gradient in momentum space. The equations of motion for W_σ resemble Boltzman equations, with additional terms due to the order parameter. In the limit that Δ varies smoothly in space, we can Taylor expand $\Delta(\vec{r} \pm \frac{\vec{s}}{2}, t)$ about \vec{r} :

$$\Delta \left(\vec{r} \pm \frac{\vec{s}}{2}, t \right) = \Delta(\vec{r}, t) \pm \vec{s} \cdot \nabla \Delta(\vec{r}, t) + \mathcal{O}(\nabla^2 \Delta). \tag{6.13}$$

In this limit, Eq. (6.12) can be rewritten as

$$\begin{aligned}
\partial_t W_\uparrow &= \frac{\vec{p}}{m} \cdot \nabla W_\uparrow - \nabla V \cdot \nabla_p W_\uparrow - \frac{2}{\hbar} \text{Im}(\Delta^* F(\vec{r}, \vec{p}, t)) - \text{Re}(\nabla \Delta^* \cdot \nabla_p F(\vec{r}, \vec{p}, t)) + \mathcal{O}(\nabla^2 \Delta) \\
\partial_t W_\downarrow &= \frac{\vec{p}}{m} \cdot \nabla W_\downarrow - \nabla V \cdot \nabla_p W_\downarrow - \frac{2}{\hbar} \text{Im}(\Delta^* F(\vec{r}, -\vec{p}, t)) - \text{Re}(\nabla \Delta^* \cdot \nabla_p F(\vec{r}, -\vec{p}, t)) + \mathcal{O}(\nabla^2 \Delta) \\
i\hbar \partial_t F &= \left(2(\epsilon_p - \mu + V(\vec{r})) - \frac{\hbar^2}{4m} \nabla^2 - \frac{m\omega^2 \hbar^2}{4} \nabla_p^2 \right) F - \Delta (W_\uparrow(\vec{r}, \vec{p}, t) + W_\downarrow(\vec{r}, -\vec{p}, t)) \\
&\quad - \frac{i\hbar}{2} \nabla \Delta \cdot \nabla_p (W_\uparrow(\vec{r}, \vec{p}, t) - W_\downarrow(\vec{r}, -\vec{p}, t)) + \frac{\Delta}{(2\pi\hbar)^3} + \mathcal{O}(\nabla^3 \Delta). \tag{6.14}
\end{aligned}$$

6.3 Homogeneous gas

In this section, we calculate $W_\sigma(\vec{r}, \vec{p}, t)$ and $F(\vec{r}, \vec{p}, t)$ for the case of a homogeneous gas ($\omega = 0$) in steady state. In this limit, we can explicitly diagonalize the Hamiltonian in Eq. (6.4), and calculate $W_\sigma(\vec{r}, \vec{p}, t)$ and $F(\vec{r}, \vec{p}, t)$. We find that

$$\begin{aligned} W_\sigma(\vec{r}, \vec{p}, t) &= \frac{1}{2(2\pi\hbar)^3} \left(1 - \frac{\epsilon_p - \mu}{E_p} \right) \\ F(\vec{r}, \vec{p}, t) &= \frac{-1}{2(2\pi\hbar)^3} \frac{\Delta}{E_p}, \end{aligned} \quad (6.15)$$

where $E_p = \sqrt{(\epsilon_p - \mu)^2 + |\Delta|^2}$ is the single particle dispersion for a superfluid. We can calculate the order parameter by substituting the self-consistency condition [Eq. (6.11)] into the definition of the renormalized interaction [Eq. (6.2)]. We obtain the implicit equation for Δ :

$$\begin{aligned} \frac{1}{g} &= \frac{1}{U} + \frac{1}{(2\pi\hbar)^3} \int \frac{d^3\vec{p}}{2\epsilon_p} \\ &= \frac{1}{2(2\pi\hbar)^3} \int d^3\vec{p} \left(\frac{1}{\epsilon_p} - \frac{1}{E_p} \right). \end{aligned} \quad (6.16)$$

We investigate the behavior of W_σ and F in the limits of weakly and strongly interacting fermions. We calculate the density of the gas and the order parameter in these limits.

6.3.1 Weakly interacting limit

For a weakly interacting gas, $\Delta \ll \mu$. For momenta far away from the Fermi surface, $p \ll p_F$, we Taylor expand E_p as

$$E_p = |\epsilon_p - \mu| + \frac{|\Delta|^2}{2|\epsilon_p - \mu|} + \mathcal{O}(\Delta^4) \quad (6.17)$$

We do not make this approximation when $p \sim p_F$. We find that the density of the gas in the weakly interacting limit is

$$n_\sigma = \int d^3\vec{p} W_\sigma(\vec{r}, \vec{p}, t) = \frac{4\pi}{3} \rho_F^3 + \mathcal{O}(\Delta^2). \quad (6.18)$$

where $\rho_F = \frac{8\pi m \sqrt{2m\mu}}{(2\pi\hbar)^3}$ is the single particle density of states at the Fermi energy.

We calculate the order parameter using the implicit equation Eq. (6.16); we obtain

$$\Delta = \frac{8\mu}{e^2} e^{-2/|g|\rho_F} + \mathcal{O}(e^{-4/|g|\rho_F}). \quad (6.19)$$

6.3.2 Strongly interacting limit

In the strongly interacting limit, the fermions form a dilute gas of weakly bound diatomic molecules with a large negative chemical potential μ , which we denote as $-\nu$. For strong interactions, $\Delta \ll \nu$. We Taylor expand E_p as

$$E_p = |\epsilon_p + \nu| + \frac{|\Delta|^2}{2|\epsilon_p + \nu|} + \mathcal{O}(\Delta^4) \quad (6.20)$$

We find that the density of the gas in this limit is

$$n_\sigma = \int d^3\vec{p} W_\sigma(\vec{r}, \vec{p}, t) = \frac{\pi^2 \Delta^2 m^2}{\sqrt{2m\nu} (2\pi\hbar)^3} + \mathcal{O}(\Delta^4). \quad (6.21)$$

We use the implicit equation in Eq. (6.16) to calculate the order parameter; we obtain

$$\Delta = \sqrt{8\nu(E_b - \nu)}, \quad (6.22)$$

where $E_b = \frac{\hbar^2}{2ma_s^2}$ is the binding energy of a weakly bound molecule.

We also observe from Eq. (6.15) that

$$2\epsilon_p F - \Delta (W_\uparrow + W_\downarrow) + \frac{\Delta}{(2\pi\hbar)^3} = -(2E_b + gn_\sigma)F. \quad (6.23)$$

We will use this relation in Sec. 6.4 to derive the Gross Pitaevskii equation.

6.4 Gross Pitaevskii equation

In this section, we consider cases where the effective chemical potential varies smoothly in space due to a weak harmonic trap, $V(\vec{r}) = \frac{1}{2}m\omega^2 r^2$, and Δ varies smoothly in space and time due to a harmonic trap and/or excitations such as solitons. We derive an equation of motion for $\Delta(\vec{r}, t)$ in the strongly interacting regime, and show that it is the Gross Pitaevskii equation.

For an inhomogeneous gas that varies smoothly in space, we calculate $W_\sigma(\vec{r}, \vec{p}, t)$ and $F(\vec{r}, \vec{p}, t)$ from Eq. (6.15), where we replace the constants Δ and μ with their smoothly varying counterparts. In particular, we find that Eq. (6.23) is replaced by

$$2\epsilon_p F(\vec{r}, \vec{p}, t) - \Delta(\vec{r}, t) (W_\uparrow(\vec{r}, \vec{p}, t) + W_\downarrow(\vec{r}, \vec{p}, t)) + \frac{\Delta(\vec{r}, t)}{(2\pi\hbar)^3} = -(2E_b + gn_\sigma(\vec{r}, t))F(\vec{r}, \vec{p}, t). \quad (6.24)$$

Substituting this relation in the equation of motion for $F(\vec{r}, \vec{p}, t)$ [Eq. (6.14)], we find that

$$i\hbar\partial_t F = \left(2 \left(V(\vec{r}) + \nu - E_b - \frac{gn_\sigma}{2} \right) - \frac{\hbar^2}{4m} \nabla^2 - \frac{m\omega^2 \hbar^2}{4} \nabla_p^2 \right) F - \frac{i\hbar}{2} \nabla \Delta \cdot \nabla_p (W_\uparrow(\vec{r}, \vec{p}, t) - W_\downarrow(\vec{r}, -\vec{p}, t)) + \mathcal{O}(\nabla^3 \Delta). \quad (6.25)$$

We obtain the Gross Pitaevskii equation by integrating Eq. (6.25) over all momenta,

$$i\hbar\partial_t \Delta = -\frac{\hbar^2}{2m_b} \nabla^2 \Delta + \left(\frac{1}{2} m_b r^2 \omega^2 - \mu_b + g_b n_b \right) \Delta + \mathcal{O}(\nabla^3 \Delta). \quad (6.26)$$

Here, $m_b = 2m$ is the mass of a weakly bound molecule, $\mu_b = 2(E_b - \nu)$ is the chemical potential for the molecules, $g_b = g$ is the effective interaction between molecules in the mean field approximation, and $n_b = n_\sigma$ is the number of molecules.

6.5 Example: Time-of-flight expansion

In this section, we numerically compute the dynamics of a quasi one-dimensional Fermi gas along the x axis during a time-of-flight expansion along the x axis. We initialize the gas in a weak harmonic trap of frequency ω along the x axis, and a tight harmonic trap in the other two directions. We consider two cases, one where the Fermi gas has a soliton and another where it does not. We calculate the initial equilibrium order parameter of the Fermi gas before the time-of-flight expansion using the time-independent Bogoliubov-de-Gennes equations [Eq. (6.6) with the left hand side set to zero] and the self-consistency condition [Eq. (6.11)]. We compute $W_\sigma(\vec{r}, \vec{p}, t)$ and $F(\vec{r}, \vec{p}, t)$ from the order parameter using Eq. (6.15). This computation is quick, and agrees well with an analogous computation of W_σ and F from their microscopic definitions, Eqs. (6.7) and (6.10). After calculating the Wigner functions in the ground state, we release the trap in the x direction only. We compute the dynamics of W_σ and F by numerically integrating their equations of motion [Eq. (6.14)].

In the strongly interacting regime, the gas is modeled well by the Gross-Pitaevskii equation [Eq. (6.26)]. In this regime, we show that our numerical results obtained from the semiclassical [Eq. (6.14)] and Gross Pitaevskii equations [Eq. (6.26)] agree. In the weakly interacting regime, we show that our numerical results obtained from the semiclassical [Eq. (6.14)] and time-dependent Bogoliubov-de-Gennes equations [Eq. (6.6)] agree at short times. We discuss the limitations of our semiclassical approach at long times.

First, we consider an inhomogeneous strongly interacting quasi-one dimensional superfluid Fermi gas in its ground state which is initially trapped in an anisotropic harmonic potential. We release the trap along the weak direction, which is the

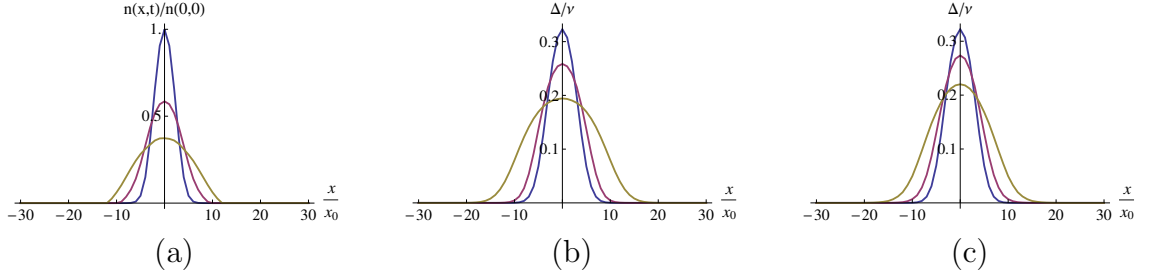


Figure 6.1: Dynamics of a strongly interacting Fermi gas during a time-of-flight expansion in the x direction. The gas is initialized in a weak harmonic trap of frequency ω in the x direction, and tight traps in the y and z directions. During the expansion, only the trap in the x direction is switched off. (a,b) Density and order parameter of the Fermi gas versus x at $y = z = 0$, computed by numerically integrating the equations of motion for W_σ and F [Eq. (6.14)]. The density is normalized by the density at the centre of the trap at $t = 0$. (c) Order parameter computed by numerically integrating the Gross Pitaevskii equation [Eq. (6.26)]. In the figures, $x_0 = \sqrt{\hbar/m\omega}$ is the harmonic oscillator length. The blue, pink, and yellow curves correspond to $t = 0, 10\hbar/\mu$, and $20\hbar/\mu$, where the expansion began at $t = 0$. For typical trap frequencies $\omega \sim 30$ Hz, and system sizes ~ 1 mm for ultracold gases, $20\hbar/\mu$ corresponds to about 12 ms of expansion.

x direction. Figures 6.1a,b show the density and order parameter of this gas at different times during the expansion, computed from numerically integrating the equations of motion of W_σ and F [Eq. (6.14)]. Figure 6.1c shows the order parameter at different times, computed from the Gross-Pitaevskii equation [Eq. (6.26)]. The results for the order parameter obtained from the two approaches agree well with each other. The relation between the density and the order parameter is also in agreement with Eq. (6.21).

In Fig. 6.2, we consider the expansion of a strongly interacting quasi-one dimensional gas with a soliton. The gas was again initially in an anisotropic harmonic potential, and the trap was released along the weak direction, which is the x direction. In Fig. 6.2a,b, we plot the density and order parameter of the gas at different times during the expansion, computed by numerically integrating Eq. (6.14). In Fig. 6.2c, we plot the order parameter for the same scenario, where

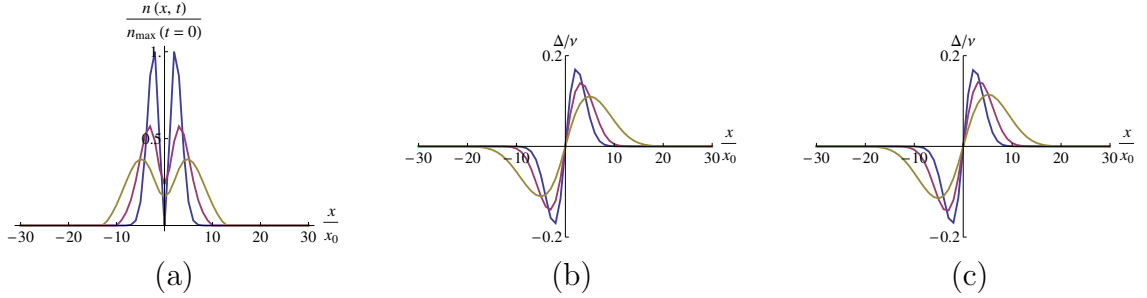


Figure 6.2: Dynamics of a strongly interacting Fermi gas during a time-of-flight expansion in the x direction. The gas is initialized in a weak harmonic trap of frequency ω in the x direction, and tight traps in the y and z directions. The gas is also initialized to have a soliton. During the expansion, only the trap in the x direction is switched off. (a,b) Density and order parameter of the Fermi gas versus x at $y = z = 0$, computed by numerically integrating the equations of motion for W_σ and F [Eq. (6.14)]. The density is normalized by the maximum density in the trap at $t = 0$. (c) Order parameter computed by numerically integrating the Gross Pitaevskii equation [Eq. (6.26)]. In the figures, $x_0 = \sqrt{\hbar/m\omega}$ is the harmonic oscillator length. The blue, pink, and yellow curves correspond to $t = 0, 10\hbar/\mu$, and $20\hbar/\mu$, where the expansion began at $t = 0$. For typical trap frequencies $\omega \sim 30$ Hz, and system sizes ~ 1 mm for ultracold gases, $20\hbar/\mu$ corresponds to about 12 ms of expansion.

the order parameter is computed from the Gross-Pitaevskii equation [Eq. (6.26)]. The results for the order parameter obtained from the two approaches again agree with each other. An important feature of the plots in Fig. 6.2 is the appearance of a soliton as a reduction in density. This density dip is used in experiments as a marker to image a soliton. We find that the density dip is visible even when the gas expands, allowing researchers to image solitons even after a time-of-flight expansion.

In Fig. 6.3, we consider an inhomogeneous weakly interacting quasi-one dimensional superfluid Fermi gas in its ground state which is initially trapped in an anisotropic harmonic potential. Figures 6.3a,b show the density and order parameter of this gas at different times during the expansion, computed from numerically integrating the equations of motion of W_σ and F [Eq. (6.14)]. The initial profile

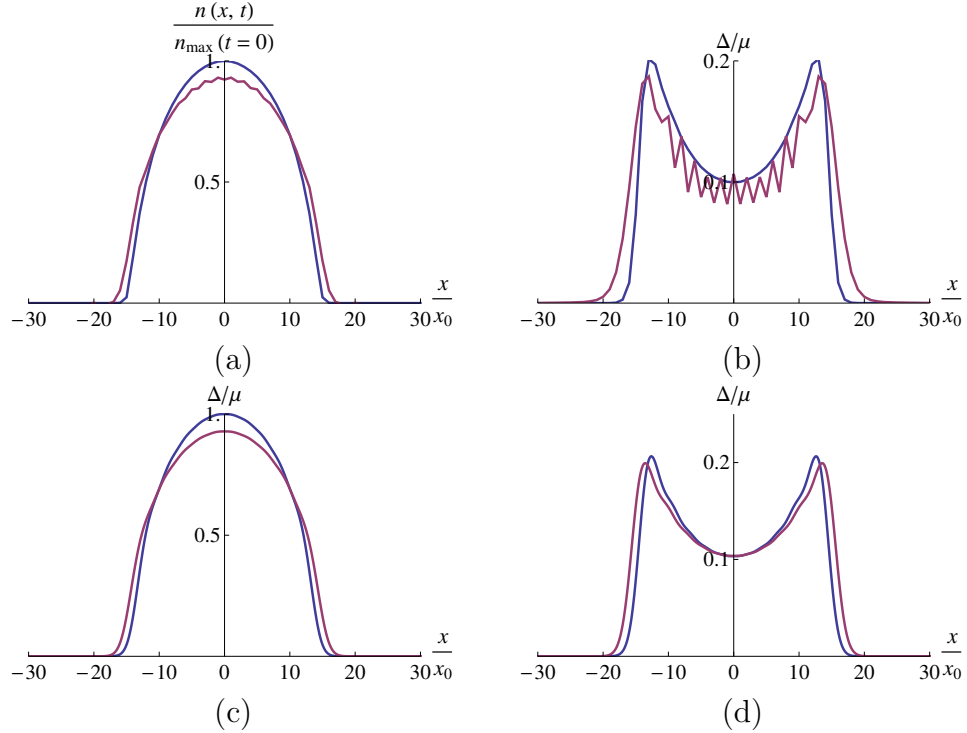


Figure 6.3: Dynamics of a weakly interacting Fermi gas during a time-of-flight expansion in the x direction. The gas is initialized in a weak harmonic trap of frequency ω in the x direction, and tight traps in the y and z directions. During the expansion, only the trap in the x direction is switched off. (a,b): Density and order parameter of the Fermi gas versus x at $y = z = 0$, computed by numerically integrating the equations of motion for W_σ and F [Eq. (6.14)]. (c,d): Density and order parameter of the Fermi gas versus x at $y = z = 0$, computed by numerically integrating the time-dependent Bogoliubov-de-Gennes equations [Eq. (6.6)]. The density in (a) and (c) is normalized by the density at the centre of the trap at $t = 0$. The blue and pink curves correspond to $t = 0$ and $5\hbar/\mu$, where the expansion began at $t = 0$. At $t = 5\hbar/\mu$, the numerical integration in (a) and (b) develops errors due to the truncation of Eq. (6.14) at second derivatives. For typical trap frequencies $\omega \sim 30$ Hz, and system sizes ~ 1 mm for ultracold gases, $5\hbar/\mu$ corresponds to about 3 ms of expansion.

of the order parameter (depicted in blue in Fig. 6.3) drops sharply near the edges of the cloud. In this region, the order parameter does not vary smoothly, and our assumption to truncate Eq. (6.14) at $\nabla^2\Delta$ is not valid. Therefore, the numerical computation develops errors which appear as noise during the dynamics. These errors are visible in the pink curve at $t = 8\hbar/\mu$ in Fig. 6.3b. These errors

propagate to the density as well soon after. In contrast, the dynamics computed from time-dependent Bogoliubov-de-Gennes equations [Eq. (6.6)], shown in Figs. 6.1c,d, are smooth and error-free. Including higher derivatives in the equations for W_σ and F to reduce numerical errors requires high spatial resolution in the numerics. For such high spatial resolution, the semiclassical approach does not have a significant advantage over numerically integrating time-dependent Bogoliubov-de-Gennes equations [Eq. (6.6)] in computation time.

6.6 Conclusions

We developed semiclassical tools to compute the properties of a Fermi gas during dynamics. We used Wigner functions to describe a superfluid Fermi gas. The equations of motion of these Wigner functions resemble Boltzman equations in statistical mechanics. We considered examples of an expanding superfluid Fermi gas with and without a soliton. We numerically integrated the Boltzman-type equations to compute the density and order parameter of the Fermi gas during its expansion. We compared these results with those obtained from Gross-Pitaevskii and time-dependent Bogoliubov-de-Gennes equations. Our results agree well with those from Gross-Pitaevskii equations for strong interactions. Our results agree well with those from time-dependent Bogoliubov-de-Gennes equations for weak interactions and short times.

Several experiments aim to measure important things using a time-of-flight expansion. One example is the FFLO gas, which has a train of solitons, and therefore a train of density dips. Typically, the gas is initialized in an array of tubes. The images are integrated columnar densities after a TOF. It is speculated

that the solitons would couple via tunneling and align with each other. This can be verified by our computation. TOF on the BEC side was done by [] using blah.

ACKNOWLEDGMENT

This material was based upon work supported by the National Science Foundation Grant No. PHY-1508300.

CHAPTER 7

CONCLUSIONS

I have used my doctoral study to explore a wide variety of topics. In this chapter, we summarize the results of my explorations. The topics of our study have been motivated by recently performed experiments, or experiments that can be performed with current technology. Experiments on ultracold atoms progress at a rapid rate, and significant experimental advances have been made since we completed our theoretical explorations on each topic in my doctoral study. In this chapter, we also review the experimental progress made on topics that we have theoretically explored, in the years between the completion of our exploration and the writing of this dissertation.

In Chapter 2, Prof. Erich Mueller and I proposed an experimental method to perform universal quantum computation using information stored in the Majorana fermion excitations of a quasi one dimensional topological superfluid formed in a cold Fermi gas. This project was motivated by several experiments that induced artificial spin orbit coupling in both Bose [162] and Fermi gases [158, 24]. In these experiments, the researchers shone two Raman lasers on an ultracold gas. The lasers couple two Zeeman states of the atoms in a ground state manifold to an excited manifold. In the far detuned limit, the atoms undergo a two photon transition, and flip their Zeeman spin. The two photon process also imparts a net momentum kick to the atoms, which is equal to the difference in momenta of the photons in the two Raman lasers. This process induces an artificial spin orbit coupling for the atoms along the direction of the net momentum kick, say the x direction. The induced spin orbit coupling is equal parts in Rashba and Dresselhaus spin orbit coupling [17, 37]. Local interactions between fermionic atoms

give rise to an effective p_x interaction in the dressed basis. In the limit of strong interactions, this gas forms a topological superfluid. We consider the case where the gas is trapped in a quasi one dimensional geometry. In this case, the system supports zero-energy Majorana fermion excitations at its edges. The ground state of the system is doubly degenerate, and encodes a qubit. We proposed using microwave spectroscopy to read and manipulate the qubit encoded in the ground state. We provided protocols to implement all the quantum gates necessary for universal quantum computation.

Our theoretical exploration of performing universal quantum computation using Majorana fermion excitations in a quasi one dimensional superfluid of spin orbit coupled fermionic atoms was completed in 2013, and published in the article Physical Review A 88, 063632 (2013), in co-authorship with Prof. Erich Mueller. However, at the time of writing this dissertation, researchers have not yet successfully tuned to the regime of a strongly interacting spin orbit coupled Fermi gas. Experiments have been hindered by the challenge due to finite occupation of excited states. The Raman lasers couple atoms in their ground state manifold to an excited manifold. The excited atoms can spontaneously decay, and impart a lot of kinetic energy to the gas. This causes heating. Typically, experimenters overcome this issue by increasing the detuning of the Raman lasers from the excited manifold, which reduces the occupation of the excited state. Increasing the detuning in turn reduces the strength of p wave interactions, which reduces the critical temperature for topological superfluidity. An alternative strategy is to produce synthetic spin orbit coupling without using Raman lasers. There have been several recent proposals that adopt this strategy (for example, [93]).

In 2016, researchers performed a related experiment, in which they induced

two dimensional synthetic Rashba spin orbit coupling for ^{40}K atoms using three Raman lasers [64]. Here, each laser coupled to a different Zeeman state of the lowest hyperfine manifold ($F = 9/2$) of ^{40}K . This system with two dimensional Rashba spin orbit coupling is more similar to the scenario in spin orbit coupled condensed matter systems such as Sr_2RuO_4 . In the strongly interacting regime, these systems will also support Majorana fermion excitations.

In Chapter 3, Prof. Erich Mueller and I modeled an experiment performed in Tilman Esslinger's group at ETH Zurich [86]. In this experiment, the researchers trap ^{87}Rb atoms inside a transversely pumped single mode optical cavity. The researchers also shine an external laser along the cavity axis, to maintain a lattice along the cavity direction at all times. The cavity mode constructively interferes when the atoms arrange in a checkerboard pattern, and lowers the energy of the atomic system. In this way, the cavity mediates infinite range checkerboard interaction between the atoms. The checkerboard pattern of the atoms breaks a discrete translational symmetry in the system, along the cavity axis. The infinite range interactions compete with quantum tunneling and short range interactions to produce a rich variety of phases for the atoms, including charge density wave, Mott insulator, superfluid and supersolid phases. Here, the supersolid phase has both charge density wave and superfluid order. We explored the phase diagram of this system using a variational approach. The presence of infinite range interactions restricts us from using local approximations for our variational parameters. Therefore, we calculated the phase diagram for this system by numerically minimizing the variational energy in a high-dimensional space: 2450 dimensions in our case. Our numerical results for the phase diagram agree well with the phase diagram measured by the Zurich group. In addition, we pointed out additional phase boundaries present in their experimental data, which would be uncovered

via further analysis of their data. Our results were published in the article *Physical Review A* 94, 033631, in co-authorship with Prof. Erich Mueller.

In 2016, the same group of experimenters at Zurich performed a similar experiment, in which they trapped ^{87}Rb atoms simultaneously inside two optical cavities aligned orthogonal to each other [91]. The researchers do not shine external lasers along the cavity axes in this experiment. When the detuning of the pump laser from the two optical cavities is equal, both the cavities are equally susceptible to support a macroscopic occupation of the respective cavity mode. In this regime, the system spontaneously chooses the strength of the electric field in the two cavities. The resulting interference pattern of the light from the two cavities spontaneously breaks a continuous translational symmetry. In this case, the atoms have supersolid order which breaks a continuous translational symmetry.

Researchers at Stanford University have also performed other related experiments where they trap ^{87}Rb atoms in a nearly confocal cavity [82]. In the ideal limit where the radius of the end mirrors equals the length of the cavity, the cavity supports an infinite number of degenerate modes at all multiples of the fundamental frequency. If the pump laser is tuned near one of the harmonics of the fundamental frequency, then all the cavity modes at that harmonic contribute to an effective interaction between the atoms trapped in the cavity. Kollar *et al* [82] consider a cavity in the few-mode-degenerate regime. They can dynamically tune the length of the cavity, which allows them to adjust the number of modes that couple to the atoms in a limited manner. When the atoms couple to a few modes, the effective interaction mediated by the cavity still has a global range, and drives the atoms towards checkerboard order with domains. For example, if the atoms couple only to the TEM_{01} mode, which is antisymmetric under inversion across the

x axis, then the atoms arrange in a checkerboard order with a larger occupation on the even sites for $x > 0$, and on the odd sites for $x < 0$. As more modes couple to the atoms, the range of the interaction shrinks. In Appendix B, we calculate the effective interaction mediated by the cavity in the infinite-mode-degenerate (i.e. ideal confocal) cavity regime. We find that the cavity-mediated interaction has two contributions: a local short range interaction centered at an atom's location (x, y) , and a nonlocal short range interaction centered at $(-x, -y)$. Such a nonlocal interaction is novel. We believe that such a novel interaction could be exciting and useful. A similar calculation by Ref. [81] did not find the nonlocal part of the interaction.

We have also explored methods to simulate iconic models in condensed matter phenomena, namely the Kondo effect and quantum dimer models. We proposed a method to produce spin dependent interactions between atoms with no orbit angular momentum ($l = 0$), using an optical Feshbach resonance. We induce a resonance between pairs of atoms by shining a laser tuned near a transition to an excited molecular state. When the detuning of the laser is large compared to the linewidth of the molecular state, second order perturbation theory gives rise to a local spin-dependent rotationally symmetric pairwise atom-atom interaction. This method to produce spin dependent interactions between the atoms was first outlined in our work published in Physical Review A 93, 023635 (2016).

To produce the Kondo model, we considered a mixture of ultracold ${}^6\text{Li}$ and ${}^{87}\text{Rb}$ atoms in Chapter 4. The ${}^6\text{Li}$ atoms act as itinerant fermions, and ${}^{87}\text{Rb}$ atoms are analogs of massive spin impurities in the conventional Kondo effect. The optical Feshbach resonance outlined above produces a Kondo-type spin-dependent interaction between the ${}^6\text{Li}$ and ${}^{87}\text{Rb}$ atoms. The spin-dependent interaction produces

spin dynamics during a scattering event between a ${}^6\text{Li}$ and a ${}^{87}\text{Rb}$ atom. This is crucial to observe an enhancement in the scattering cross section at low temperatures. To observe this enhancement, we propose launching the ${}^{87}\text{Rb}$ gas into the ${}^6\text{Li}$ gas, and measuring the final momentum of the ${}^6\text{Li}$ gas. We calculated the momentum exchanged between the ${}^{87}\text{Rb}$ and ${}^6\text{Li}$ gases during this scattering experiment, perturbatively to third order in the interaction strength. We show that the momentum exchanged varies nonmonotonically with temperature. In particular, the momentum exchanged has an experimentally detectable minimum at a characteristic temperature, and increases logarithmically below this temperature, analogous to the electrical resistivity of magnetic alloys in the conventional Kondo effect. Our work was published in the article *Physical Review A* 93, 023635 (2016), in co-authorship with Prof. Erich Mueller.

Next, I entered into a collaboration with Prof. Erich Mueller, Prof. Michael Lawler, and Todd Rutkowski, and proposed a method to produce a quantum dimer model for bosonic atoms (see Chapter 5). We considered a gas of bosons with no orbital angular momentum, $l = 0$, and a relatively large hyperfine spin f . Candidate atoms could be ${}^{87}\text{Rb}$, which has $f = 2$, and ${}^{52}\text{Cr}$, which has $f = 3$. We imagined loading these atoms in a deep optical lattice, and tuning to the regime where the occupation on the lattice sites is unity. We induced an optical Feshbach resonance, and tuned to the regime where the net interaction in the hyperfine spin singlet channel is smaller than the interaction in the other hyperfine spin channels, but larger than the tunneling between lattice sites. In this regime, virtual hopping drives the atoms to entangle in hyperfine spin singlets with neighboring atoms. The resulting theory has the form of a quantum dimer model. In the limit of large f , we found a rich variety of ground states in different lattice geometries: columnar phase on a square lattice, $\sqrt{12} \times \sqrt{12}$ phase on a triangular lattice, and a plaquette phase

on a hexagonal lattice. The ground state on a cubic lattice is a matter of theoretical debate. We also calculated the ground state for different lattice geometries and different values of the hyperfine spin f , using an exact diagonalization of a small system. Our calculations indicated that the ground states for a typical value of $f = 3$ are the same as those for a large f . We proposed using a combination of resonant photoassociation and quantum gas microscopy to experimentally image dimer bonds, and measure dimer-dimer correlations in the system. We produced numerical calculations of dimer-dimer correlations for different lattice geometries and hyperfine spins f , on a small system. We are currently preparing an article on this work for publication in a peer-reviewed journal.

Experimenters have not yet produced tunable spin dependent interactions between atoms. Optical Feshbach resonances are rarely used as the primary mechanism to tune inter-atom interactions. Some researchers have attempted to tune the scattering length of a gas using an optical Feshbach resonance in conjunction with a magnetic Feshbach resonance [28, 53]. To date, the largest change in scattering length obtained using this scheme is $\sim 180a_0$ in a gas of ^{133}Cs atoms [28]. In comparison, in that experiment, the background scattering length in the presence of a magnetic field was $950a_0$. We calculated that our proposal to optically induce spin-dependent interactions between atoms in a gas requires a large laser intensity $\sim 1 \text{ MW/cm}^2$.

Producing a reasonably large tunable rotationally symmetric spin dependent inter-atom interaction would have several immediate applications. As we have discussed in this dissertation, it would allow us to produce several iconic models in condensed matter physics, namely the Kondo model and the quantum dimer model. Apart from these, we can explore spinor phases for homogeneous spinor

gases by spin dependent interactions in them. Researchers have proposed exotic phases and phase diagrams for homogeneous spinor gases at finite temperature and finite values of the spin-dependent interaction [118].

We also imagine that our techniques for producing spin dependent interaction can be adapted to measure spin correlations in ultracold gases. For example, researchers are interested in extracting spin correlations in ultracold Fermi gases loaded in a deep lattice, at half filling. These experiments are motivated by studies of antiferromagnetic phases of electrons at half filling in superconducting materials with a high T_c . In these systems, adjacent electrons are entangled in spin singlets. Researchers on ultracold fermions extract long range correlations in the azimuthal spins of ultracold fermions on a lattice, by imaging the different spin species independently [127]. We imagine that one could directly image spin entanglement between adjacent fermions on the lattice, using the resonant photoassociation that we have outlined earlier. Measurements of spin entanglement between nearest neighbor fermions would complement current efforts to measure azimuthal spin correlations.

In Chapter 6, Prof. Erich Mueller and I developed semiclassical tools to explore the dynamics of ultracold fermionic superfluids. We used Wigner functions to model the Fermi gas, and showed that the equations of motion of the Wigner functions resembled semiclassical Boltzman equations. In the strongly interacting regime, our tools are complementary to computing the dynamics by integrating time-dependent Bogoliubov-de-Gennes equations. In this regime, we integrated the semiclassical Boltzman equations in phase space, and showed that these equations led to the Gross Pitaevskii equation. In the weakly interacting regime, our tools are complementary to integrating time-dependent Bogoliubov-de-Gennes equations at

short times. At long times, our semiclassical tools are unstable to numerical errors due to sharp variations in the order parameter. We compared results of numerical integrations of semiclassical Boltzman, time-dependent Bogoliubov-de-Gennes, and Gross-Pitaevskii equations in different regimes of interaction. We found that the dynamics computed from the semiclassical method were in agreement with methods that used Gross-Pitaevskii or time-dependent Bogoliubov-de-Gennes equations in the strongly interacting regime, and time-dependent Bogoliubov-de-Gennes methods in the weakly interacting regime at short times.

We hope that our explorations provide useful input to the community researching on ultracold atoms. In the case of projects where we made proposals for experiments, our greatest reward would be an experiment that implements our proposal. In the case of projects where we model experiments, our greatest reward would be an experiment that builds on the understand provided by our model. We hope the reader found this dissertation useful, and enjoyed reading it as much as I enjoyed writing it.

APPENDIX A
MAJORANA FERMIONS

A.1 Superfluid gap from nearest-neighbor interactions

Nearest-neighbor interactions in the tight-binding model [Eq. (2.2)] for the “a” atoms in an optical lattice lead to a superfluid gap Δ , given implicitly by the gap equation,

$$\frac{-1}{V} = \frac{1}{N} \sum_k \frac{\sin^2 ka}{\sqrt{(2J \cos ka - \mu)^2 + (2\Delta \sin ka)^2}}, \quad (\text{A.1})$$

where N is the number of lattice sites, a is the lattice constant, V is the nearest-neighbor interaction strength, J is the hopping amplitude, and allowed momenta $k = \frac{2n\pi}{Na}$, ($n = 0, 1, \dots, N-1$) are summed over. J is typically controlled by the depth of the optical lattice, and V depends on the parameters dictating the mechanism creating nearest-neighbor interactions, and the s -wave scattering length if applicable. Below we calculate the superfluid gap created in three different mechanisms producing nearest-neighbor interactions.

A.1.1 Dipolar molecules

Dipolar molecules such as KRb or LiCs have nearest-neighbor dipole-dipole interactions. The interaction strength of two molecules at adjacent lattice sites, with dipole moments \vec{d}_1 and \vec{d}_2 is

$$V = \frac{\vec{d}_1 \cdot \vec{d}_2 - 3\vec{d}_1 \cdot \hat{r} \vec{d}_2 \cdot \hat{r}}{4\pi\epsilon_0 a^3}, \quad (\text{A.2})$$

where a is the lattice constant and \hat{r} is the unit vector joining the two lattice sites. For typical dipole moments of the order of 10 D and typical lattice spacings of

a few μm , this interaction strength is on the order of a few kHz. For hopping amplitudes of a few kHz, Eq. (A.1) results in a superfluid gap of the order of kHz.

A.1.2 Artificial spin-orbit coupling

Nearest-neighbor interaction arises in spin-orbit coupled gases as an effective interaction between atoms in dressed states (the helicity states). The Hamiltonian describing the bare atoms is

$$\hat{H} = \sum_k \begin{pmatrix} \hat{a}_{\uparrow k+k_L}^\dagger & \hat{a}_{\downarrow k-k_L}^\dagger \end{pmatrix} \begin{pmatrix} \epsilon_{k+k_L} & \Omega \\ \Omega & \epsilon_{k-k_L} \end{pmatrix} \begin{pmatrix} \hat{a}_{\uparrow k+k_L} \\ \hat{a}_{\downarrow k-k_L} \end{pmatrix} + V \sum_i \hat{a}_{\uparrow i}^\dagger \hat{a}_{\downarrow i}^\dagger \hat{a}_{\downarrow i} \hat{a}_{\uparrow i} \quad (\text{A.3})$$

where the Raman coupling strength Ω will dictate the energy gap between the two helicity states, $\epsilon_k = -2J \cos ka$ is the kinetic energy due to tunneling in an optical lattice. For small momenta, the spin-orbit coupling strength is $-2Ja \sin k_L a$, where k_L is the recoil momentum due to a Raman photon. The effective nearest-neighbor interaction between two atoms in the lower helicity state is

$$V_{eff} \simeq V \left(\frac{2J}{\Omega} \sin k_L a \right)^2 \quad (\text{A.4})$$

for $\Omega \gg 2J$. $J_{eff} \simeq J \cos k_L a$ is the effective hopping amplitude between atoms in dressed states. For typical scattering lengths of the order of 100 Bohr radii at Feshbach resonance and typical hopping amplitudes of a few kHz, the superfluid gap from Eq. (A.1) is a few kHz.

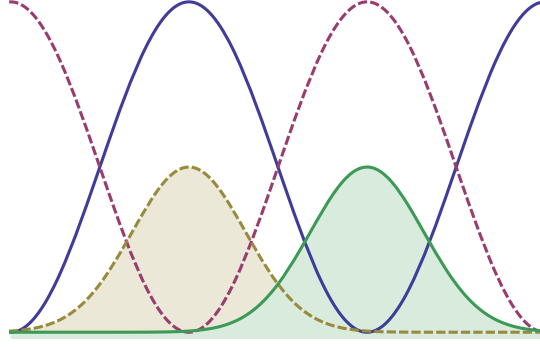


Figure A.1: (Color online) Schematic of a deep spin-dependent lattice and a transverse magnetic field.

A.1.3 Spin-dependent lattices

Another way to create strong nearest-neighbor interactions between atoms is to increase the overlap between Wannier functions at two adjacent sites on an optical lattice. For example, consider the spin-dependent lattice along the x direction illustrated in Fig. A.1, with its spin-quantization axis along the z direction. The sites for \uparrow -spins are shifted by half a lattice constant relative to the sites of the \downarrow -spins. Equivalently, we can consider a superlattice with \uparrow -spins on the even sites and \downarrow -spins on the odd sites. In the presence of a transverse magnetic field $B\hat{y}$, this system can be modeled by the Hamiltonian

$$\begin{aligned}
\hat{H} = \int dx \frac{-\hbar^2}{2m} \sum_{\sigma} \left(\hat{\psi}_{\sigma}^{\dagger}(x) \frac{\partial^2}{\partial x^2} \hat{\psi}_{\sigma}(x) \right) \\
+ U_0 \cos^2 \frac{\pi x}{a} \hat{\psi}_{\uparrow}^{\dagger}(x) \hat{\psi}_{\uparrow}(x) + U_0 \sin^2 \frac{\pi x}{a} \hat{\psi}_{\downarrow}^{\dagger}(x) \hat{\psi}_{\downarrow}(x) \\
- \mu_0 B (\hat{\psi}_{\uparrow}^{\dagger}(x) \hat{\psi}_{\downarrow}(x) + \hat{\psi}_{\downarrow}^{\dagger}(x) \hat{\psi}_{\uparrow}(x)) + g \hat{\psi}_{\uparrow}^{\dagger}(x) \hat{\psi}_{\downarrow}^{\dagger}(x) \hat{\psi}_{\downarrow}(x) \hat{\psi}_{\uparrow}(x),
\end{aligned} \tag{A.5}$$

where m is the mass of the fermion, U_0 is the lattice depth, μ_0 is the Bohr magneton, and g is the on-site interaction strength. Here $\hat{\psi}_{\uparrow}(x) = \sum_i \hat{a}_{2i\uparrow} \phi(x - x_{2i})$ and $\hat{\psi}_{\downarrow}(x) = \sum_i \hat{a}_{2i+1\downarrow} \phi(x - x_{2i+1})$ are field operators for \uparrow -spins and \downarrow -spins, where $\hat{a}_{i\sigma}$ annihilates a fermion with spin σ at site i , $\phi(x)$ is the Wannier function, x_i are the positions of the lattice sites, and all sites i have been summed over. The

first term in Eq. (A.5), which gives rise to hopping between sites with the same spin on the lattice, can be quenched by increasing the lattice depth. The magnetic field enables the fermions to hop between adjacent sites on the superlattice while flipping their spin. The last term in Eq. (A.5) gives rise to interactions between adjacent fermions with opposite spin. This is clearly illustrated by rewriting the Hamiltonian in terms of new operators $\hat{b}_{2i} = \hat{a}_{2i\uparrow}$, $\hat{b}_{2i+1} = \hat{a}_{2i+1\downarrow}$ as

$$\hat{H} = \sum_i -J_{eff}(\hat{b}_i^\dagger \hat{b}_{i+1} + h.c.) + V_{eff} \hat{b}_i^\dagger \hat{b}_{i+1}^\dagger \hat{b}_{i+1} \hat{b}_i. \quad (\text{A.6})$$

This is equivalent to a model for a gas of spinless fermions with nearest-neighbor interactions on an optical lattice. Direct computation yields

$$J_{eff} = \mu_0 B \int dx \phi^*(x) \phi(x - a/2) \quad (\text{A.7})$$

and

$$V_{eff} = g \int dx |\phi(x)|^2 |\phi(x - a/2)|^2. \quad (\text{A.8})$$

Magnetic fields of a few Gauss lead to hopping amplitudes in the MHz range. If we tune the interaction strength to a few MHz via a Feshbach resonance, the superfluid gap from Eq. (A.1) would be on the order of a few MHz.

A.2 Edge modes

The creation operator for the zero-energy quasiparticle has the form

$$\hat{\gamma}_{\text{edge}}^\dagger = \sum_j f_0(j) \left(\frac{\hat{a}_j^\dagger + \hat{a}_j}{2} + i \frac{\hat{a}_{N+1-j}^\dagger - \hat{a}_{N+1-j}}{2i} \right). \quad (\text{A.9})$$

Demanding that the quasiparticle created by this operator has zero energy leads to difference equations governing the coherence factors $f_0(j)$,

$$(J - \Delta_{j-1})f_0(j-1) + (J + \Delta_{j+1})f_0(j+1) - \mu f_0(j) = 0, \quad 1 < j < N, \quad (\text{A.10})$$

For the non-self-consistent case of uniform $\Delta_j = \Delta$, these equations are solved by assuming a solution of the form $f_0(j) = \alpha x_+^j + \beta x_-^j$. α and β are determined by the boundary conditions

$$\begin{aligned} f_0(2) &= \frac{\mu}{J+\Delta} f_0(1), & \text{if } \Delta > 0, \\ f_0(N-1) &= \frac{\mu}{J-\Delta} f_0(N), & \text{if } \Delta < 0, \end{aligned} \tag{A.11}$$

and the normalization condition

$$\sum_j \left| \frac{f_0(j) + f_0(N+1-j)}{2} \right|^2 + \left| \frac{f_0(j) - f_0(N+1-j)}{2} \right|^2 = 1. \tag{A.12}$$

The difference equations yield

$$x_{\pm} = \frac{\mu}{2(J+\Delta)} \pm \sqrt{\left(\frac{\mu}{2(J+\Delta)} \right)^2 + \frac{\Delta - J}{\Delta + J}}, \tag{A.13}$$

and the boundary conditions yield $\alpha = -\beta$ if $\Delta > 0$, and $\alpha = -\left(\frac{x_-}{x_+}\right)^{N+1} \beta$ if $\Delta < 0$.

APPENDIX B

**ATOMIC INTERACTIONS MEDIATED BY AN IDEAL
CONFOCAL CAVITY**

Here, we calculate the effective interactions between bosonic atoms trapped in a transversely pumped ideal confocal cavity, where the interactions are mediated by superradiant light in the cavity. A cavity mode is described by three numbers—two integers l and m for the transverse shape, and one integer n for the wavelength. The frequency of a cavity mode parameterized by n , l , and m is

$$\omega_{nlm} = \frac{\pi c}{L} \left(n + \frac{l+m+1}{\pi} \right) \cos^{-1} \sqrt{\left(1 - \frac{L}{R_1}\right) \left(1 - \frac{L}{R_2}\right)}, \quad (\text{B.1})$$

where L is the length of the cavity, and R_1 and R_2 are the radii of the end mirrors. The wavelength is related to n as $\lambda_n = 2L/n$. In an ideal confocal optical cavity, where $R_1 = R_2 = L$, the frequency of the modes has the simple form

$$\omega_{nlm} = \frac{\pi c}{L} \left(n + \frac{l+m+1}{2} \right). \quad (\text{B.2})$$

In this case, the cavity has a fundamental frequency of $\frac{\pi c}{2L}$. There are an infinite number of degenerate modes at every harmonic; here, the harmonic frequencies are multiples of $\frac{\pi c}{2L}$. All the degenerate modes at one frequency have the same parity of $l+m$. The transverse shape of a mode parameterized by n , l and m is

$$E_{nlm}^\perp(x, y) = E_0 e^{-(x^2+y^2)/2w^2(z)} \frac{H_l(x/\sqrt{2}w(z))H_m(y/\sqrt{2}w(z))}{\sqrt{2^{l+m}l!m!}}, \quad (\text{B.3})$$

where the cavity lies along the z direction, $w(z)$ is the width of the mode at longitudinal position z , $R(z)$ is the curvature of the mode, and H_l is a Hermite Gaussian function. The mode shape does not depend on n .

We consider the setup in Ref. [82], where bosonic atoms are trapped in a lattice in the confocal cavity. We assume that the lattice is deep in the y direction. When

the cavity is transversely pumped in the x direction by a laser of frequency ω near one of the mode frequencies ω_{nlm} , the cavity modes mediate pairwise effective interactions between the trapped atoms. Let us denote the positions of the atoms by $(x_1, y_1, z_1), \dots, (x_n, y_n, z_n)$. Following the methods in [99], the Hamiltonian modeling the effective pairwise interaction between the atoms, in first quantization, is

$$H_{\text{int}} = U_{\text{int}} \sum_{lm} \frac{\left(\sum_{i=1}^n \cos kx_i \cos k_n z_i E_{nlm}^\perp(x_i, y_i)\right)^2}{\Delta_{nlm}}, \quad (\text{B.4})$$

where $k_n = 2\pi/\lambda_n$ is the wavenumber of the mode, and $k = 2\pi/\lambda$ is the wavenumber of the pump. In Eq. (B.4), U_{int} is an interaction coefficient that depends on optical coupling strengths, and $\Delta_{nlm} = \omega - \omega_{nlm}$ is the detuning of the pump from the cavity mode. We assume the pump frequency is tuned close to an odd multiple of $\pi c/2L$. In this case, only one infinite set of degenerate modes couple to the atoms, i.e $\Delta_{nlm} = \Delta$ is a constant. All the modes that couple to the atoms have the same integer value of $n + \frac{l+m+1}{2}$. In particular, $l + m$ is an even number. We find from Eq. (B.4) that the interaction between a pair of atoms at $\vec{r}_1 = (x_1, y_1, z_1)$ and $\vec{r}_2 = (x_2, y_2, z_2)$ is

$$H_{\text{int}}(\vec{r}_1, \vec{r}_2) = \frac{2U_{\text{int}}}{\Delta} \sum_{\substack{lm \\ \omega_{nlm}=\omega}} \cos kx_1 \cos k_n z_1 \cos kx_2 \cos k_n z_2 E_{nlm}^\perp(x_1, y_1) E_{nlm}^\perp(x_2, y_2). \quad (\text{B.5})$$

In the sum in Eq. (B.5), the value of n is such that ω_{nlm} is a constant. The contributions from a mode parameterized by l and m grows smaller as l and m increase; this is because the strength of the mode grows smaller. Therefore, significant contributions come only from terms in the sum up to critical values l_c and m_c . We assume the wavenumber k_n is sufficiently large that $k_{n-l_c-m_c} \sim k_n \sim k$. In this case, all the cosine terms in Eq. (B.5) can be pulled out of the sum. Since the contributions to the sum from modes beyond l_c and m_c is negligible, we extrapolate

the limits for l and m in the sum in Eq. (B.5) to be ∞ , *still* assuming that k_n is a constant.

We calculate the expression $\sum_{lm} E_{nlm}^\perp(x_1, y_1) E_{nlm}^\perp(x_2, y_2)$ using the generating functional of Hermite Gaussian functions:

$$\sum_{n=0}^{\infty} \frac{z^n}{n!} H_n(\alpha) = e^{-z^2 + 2z\alpha}. \quad (\text{B.6})$$

We obtain the result

$$\begin{aligned} \sum_{l=0}^{\infty} \frac{H_l(\alpha) H_l(\beta)}{2^l l!} &= \frac{2}{\pi} \int d^2 z e^{-2|z|^2} e^{-z^2 + 2z\alpha} e^{-\bar{z}^2 + 2\bar{z}\alpha} \\ &= \sqrt{\pi} e^{\alpha^2} \delta(\alpha - \beta), \end{aligned}$$

where \bar{z} is the complex conjugate of z , and δ is the Dirac delta function. Similarly, we obtain

$$\begin{aligned} \sum_{l=0, l \in \text{even}}^{\infty} \frac{H_l(\alpha) H_l(\beta)}{2^l l!} &= \frac{\sqrt{\pi}}{2} e^{\alpha^2} (\delta(\alpha - \beta) + \delta(\alpha + \beta)), \\ \sum_{l=0, l \in \text{odd}}^{\infty} \frac{H_l(\alpha) H_l(\beta)}{2^l l!} &= \frac{\sqrt{\pi}}{2} e^{\alpha^2} (\delta(\alpha - \beta) - \delta(\alpha + \beta)). \end{aligned} \quad (\text{B.7})$$

The sum in Eq. (B.5) involves l and m of the same parity, to keep ω_{nlm} a constant.

Using the results in Eq. (B.7), we calculate the desired expression

$$\sum_{l+m \in \text{even}} E_{nlm}^\perp(\vec{r}_1) E_{nlm}^\perp(\vec{r}_2) = \frac{\pi}{4} (\delta^{(2)}(\vec{r}_{1\perp} - \vec{r}_{2\perp}) + \delta^{(2)}(\vec{r}_{1\perp} + \vec{r}_{2\perp})), \quad (\text{B.8})$$

where \vec{r}_\perp is the projection of \vec{r} onto the x - y plane. The effective pairwise interaction between two atoms is

$$H_{\text{int}}(\vec{r}_1, \vec{r}_2) = \frac{\pi U_{\text{int}}}{2\Delta} \cos kx_1 \cos kx_2 \cos kz_1 \cos kz_2 \left(\delta^{(2)}\left(\frac{\vec{r}_{1\perp} - \vec{r}_{2\perp}}{w(z)}\right) + \delta^{(2)}\left(\frac{\vec{r}_{1\perp} + \vec{r}_{2\perp}}{w(z)}\right) \right). \quad (\text{B.9})$$

A calculation for the case where ω is tuned near an even multiple of $\frac{\pi c}{2L}$ yields a similar form of the interaction, with a relative minus sign between the Dirac delta functions.

We remark that the effective interaction obtained in Eq. (B.9) has an unusual form: the interaction is short ranged due to its Dirac delta form, but is nonlocal because one of the Dirac delta functions is centered at $\vec{r}_{1\perp} = -\vec{r}_{2\perp}$. The form of this interaction seems to suggest that each atom at $\vec{r}_1 + (x_1, y_1, z_1)$ has a shadow at $\vec{r}_2 = (-x_1, -y_1, z_1)$, and the atoms other interact with this atom *and* its shadow with a short ranged interaction.

APPENDIX C

THE KONDO EFFECT: MOMENTUM EXCHANGED IN A SCATTERING EXPERIMENT

C.1 Calculation of the momentum transferred

Here we calculate $n_{k\alpha m}(t)$ in Eq. (4.11) and $\vec{P}(t)$ in Eq. (4.12). The standard way to calculate quantities like $n_{k\alpha m}(t)$ is using the S -matrix [98]:

$$\begin{aligned} n_{k\alpha m}(t) &= \langle T \hat{S} \hat{b}_{M_b v, m}(0) \hat{a}_{k\alpha}^\dagger(t) \hat{a}_{k\alpha}(t) \hat{b}_{M_b v, m}^\dagger(0) \rangle_0, \\ \hat{S} &= e^{-i \int d\tau \hat{H}_{\text{int}}(\tau)}, \end{aligned} \tag{C.1}$$

where T orders the operators along a path shown in Fig. C.1 which starts at time 0, passes through time t , and returns to time 0. All our integrals over time follow this path. The notation $\langle \rangle_0$ implies that all operators inside $\langle \rangle_0$ evolve according to

$$\begin{aligned} \hat{a}_{k\alpha}(t) &= e^{i\hat{H}_0 t/\hbar} \hat{a}_{k\alpha} e^{-i\hat{H}_0 t/\hbar}, \\ \hat{b}_{k\mu}(t) &= e^{i\hat{H}_0 t/\hbar} \hat{b}_{k\mu} e^{-i\hat{H}_0 t/\hbar}, \end{aligned} \tag{C.2}$$

and states are weighted by $e^{-\beta\hat{H}_0}$. Since \hat{H}_0 is quadratic in $\hat{a}_{k\alpha}$ and $\hat{b}_{k\mu}$, the right-hand side of $n_{k\alpha m}(t)$ in Eq. (C.1) can be contracted using Wick's theorem. As a result, $n_{k\alpha m}(t)$ can be expressed diagrammatically as a sum of Feynman's diagrams. We calculate these Feynman's diagrams up to $O(g_s^3)$ and $O(g_n^3)$ in the long time limit.

C.1.1 Feynman rules

We denote the propagator for fermions, $\langle T \hat{a}_{k\alpha}(t_1) \hat{a}_{k\alpha}^\dagger(t_2) \rangle_0$, by a solid line, and the propagator for bosons, $\langle T \hat{b}_{k\mu}(t_1) \hat{b}_{k\mu}^\dagger(t_2) \rangle_0$, by a dotted line, depicted in Figs.

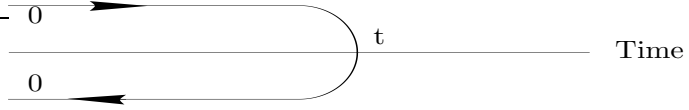


Figure C.1: In our integrals, time begins at 0, passes through t , then returns to 0. Our perturbation theory requires ordering operators along this path.

C.2(a) and C.2(b). Their values are

$$\begin{aligned} \langle T \hat{a}_{k\alpha}(t_1) \hat{a}_{k\alpha}^\dagger(t_2) \rangle_0 &= e^{-i\epsilon_k(t_1-t_2)} (\Theta(t_1-t_2) - f_k), \\ \langle T \hat{b}_{k\mu}(t_1) \hat{b}_{k\mu}^\dagger(t_2) \rangle_0 &= e^{-iE_k(t_1-t_2)} \Theta(t_1-t_2). \end{aligned} \quad (\text{C.3})$$

In Eq. (C.3), $\Theta(t_1-t_2) = 1$ if t_1 is after t_2 along the path in Fig. C.1, and 0 otherwise.

We perturbatively expand $n_{k\alpha m}(t)$ in the vertex depicted in Fig. C.2(c), whose value is

$$= \frac{(2\pi)^3}{V^2} \delta(k_1 + k_3 - k_2 - k_4) \left(g_s \vec{\sigma}_{\alpha\beta}^{(1/2)} \cdot \vec{\sigma}_{\mu\nu}^{(S)} + g_n \delta_{\alpha\beta} \delta_{\mu\nu} \right). \quad (\text{C.4})$$

The vertex denotes a scattering event between a fermion and a boson. The time at which this scattering event occurs is integrated over the path in Fig. C.1. All momenta and spin projections are summed/integrated over, with the constraint that momenta and spin are conserved at each vertex. The diagrams which contribute to Eq. (C.1) have four external propagators. There is an incoming and outgoing fermion propagator evaluated at time t , and carrying momentum $\hbar\vec{k}$ and spin projection α . There is also an incoming and outgoing boson propagator evaluated at time 0, and carrying momentum $M_b\vec{v}$ and spin projection m . All lines and vertices in a Feynman diagram can be labeled using the rules described above. Therefore we omit labels. Finally, each diagram carries a multiplicity, which is the number of times it appears in the expansion of Eq. (C.1) in powers of g_s and g_n .

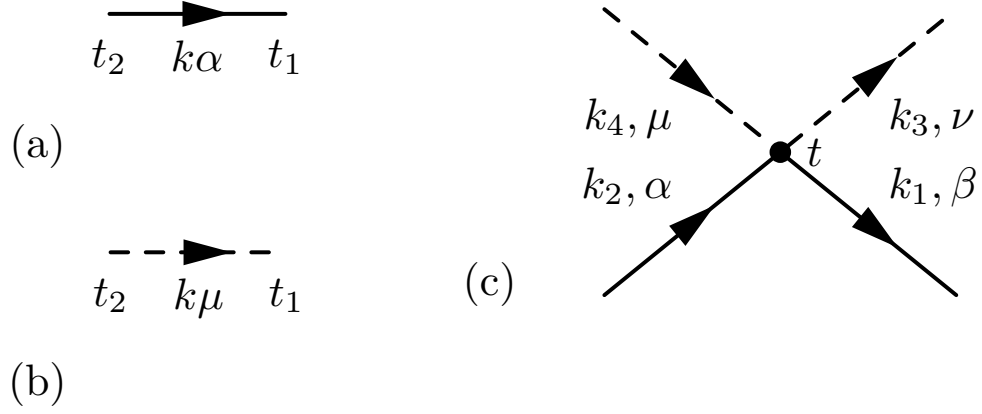


Figure C.2: Diagrammatic representation of vertex and propagators. (a) Solid line denotes a fermion propagator which propagates a fermion with momentum k and spin projection α from time t_2 to t_1 . (b) Dashed line denotes a boson propagator which propagates a boson with momentum k and spin projection μ from time t_2 to t_1 . (c) A vertex denotes the matrix element for a Bose-Fermi scattering event. Mathematical expressions are given in Eqs.(C.3) and (C.4).

C.1.2 Calculation of $n_{k\alpha m}(t)$

Terms of $O(g_{s,n}^n)$ in the perturbative expansion of $n_{k\alpha m}(t)$ contain $2n + 2$ pairs of operators leading to $(n + 1)!$ contractions. The resulting number of diagrams increases exponentially with n . We explicitly consider each order and evaluate the nonzero diagrams.

Zeroth order

The expression for the zeroth-order term in the expansion of $n_{k\alpha m}(t)$ is

$$n_{k\alpha m}^{(0)}(t) = \langle T \hat{b}_{M_b, v, m}(0) \hat{a}_{k\alpha}^\dagger(t) \hat{a}_{k\alpha}(t) \hat{b}_{M_b, v, m}^\dagger(0) \rangle_0. \quad (\text{C.5})$$

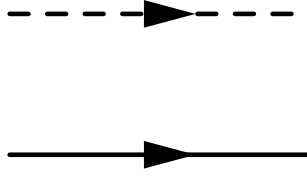


Figure C.3: Zeroth-order diagram in the expansion for $n_{k\alpha m}(t)$.

Using Wick's theorem,

$$\begin{aligned} n_{k\alpha m}^{(0)}(t) &= \langle \hat{b}_{Mbv,m}(0) \hat{b}_{Mbv,m}^\dagger(0) \rangle_0 \langle \hat{a}_{k\alpha}^\dagger(t) \hat{a}_{k\alpha}(t) \rangle_0 \\ &= f_k. \end{aligned} \quad (\text{C.6})$$

The corresponding Feynman diagram is shown in Fig. C.3. Since the bosons and fermions do not interact at this order, $n_{k\alpha m}^{(0)}$ does not contribute to any momentum transfer.

First order

The first order term in the expansion for $n_{k\alpha m}(t)$ is

$$n_{k\alpha m}^{(1)}(t) = -i \int d\tau_1 \langle T \hat{H}_{\text{int}}(\tau_1) \hat{b}_{Mbv,m}(0) \hat{a}_{k\alpha}^\dagger(t) \hat{a}_{k\alpha}(t) \hat{b}_{Mbv,m}^\dagger(0) \rangle_0. \quad (\text{C.7})$$

By Wick-contracting the above expression, we find that $n_{k\alpha m}^{(1)}(t)$ is the sum of the four diagrams shown in Fig. C.4, all of which evaluate to zero. For example,

$$\begin{aligned} \text{Diagram} &= \int d\tau \left(\frac{1}{2} g_s m + g_n \right) = 0. \end{aligned} \quad (\text{C.8})$$

Due to the same reason, Figs. C.4(b), C.4(c) and C.4(d) are also zero. Therefore,

$$\frac{1}{3} \sum_m n_{k\alpha m}^{(1)}(t) = 0. \quad (\text{C.9})$$

Moreover, the same reasoning implies that all higher-order diagrams in which a fermion or boson loop begins and ends at the same vertex are also zero.

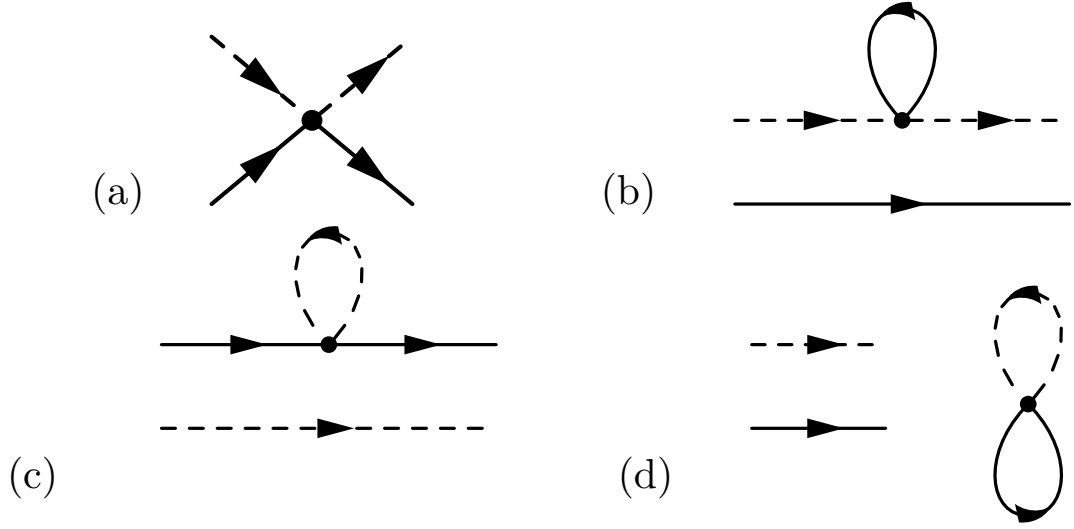


Figure C.4: First order diagrams in the expansion of $n_{kam}(t)$.

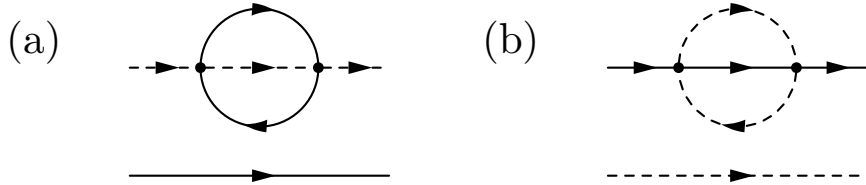


Figure C.5: Two of the diagrams that are zero at second order.

Second order

The second order term,

$$n_{kam}^{(2)}(t) = -\frac{1}{2} \int d\tau_1 d\tau_2 \langle T \hat{H}_{\text{int}}(\tau_1) \hat{H}_{\text{int}}(\tau_2) \hat{b}_{M_b, v, m}(0) \hat{a}_{k\alpha}^\dagger(t) \hat{a}_{k\alpha}(t) \hat{b}_{M_b, v, m}^\dagger(0) \rangle_0, \quad (\text{C.10})$$

can be contracted into Wick pairs in 36 ways, which give rise to 20 different diagrams. Most of these diagrams are zero because of reasons explained in the previous sections. In addition, the diagrams shown in Fig. C.5 also evaluate to zero. For example, since we work in the dilute boson limit, there can only be one boson line in any time slice, implying that Fig. C.5(a) is zero. The only two nonzero diagrams are shown in Fig. C.6.

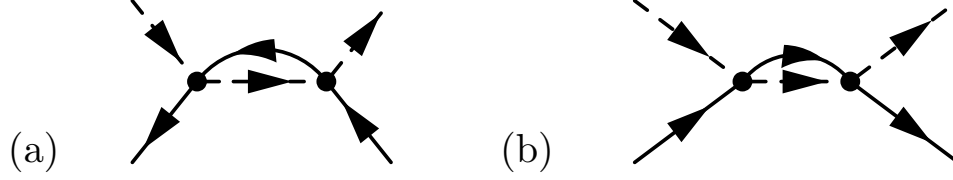


Figure C.6: Nonzero diagrams at $O(g^2)$ in the expansion for $n_{k\alpha m}(t)$.

Using our Feynman rules,

$$\frac{1}{3} \sum_m \text{Diagram (a)} = \frac{2}{V(2\pi)^3} \int d^3\vec{p} (1 - f_k) f_p \frac{\sin^2 \delta\epsilon t / \hbar}{\delta\epsilon^2} \left(g_s^2 \frac{S(S+1)}{2} + 2g_n^2 \right), \quad (\text{C.11})$$

and

$$\frac{1}{3} \sum_m \text{Diagram (b)} = -\frac{2}{V(2\pi)^3} \int d^3\vec{p} f_k (1 - f_p) \frac{\sin^2 \delta\epsilon' t / \hbar}{\delta\epsilon'^2} \left(g_s^2 \frac{S(S+1)}{2} + 2g_n^2 \right), \quad (\text{C.12})$$

where $\delta\epsilon = \frac{1}{2} \left(\epsilon_k - \epsilon_p - \frac{1}{2} M_b v^2 + \frac{(\hbar\vec{k} - \hbar\vec{p} - M_b \vec{v})^2}{2M_b} \right)$ and

$\delta\epsilon' = \frac{1}{2} \left(\epsilon_k - \epsilon_p + \frac{1}{2} M_b v^2 - \frac{(\hbar\vec{k} - \hbar\vec{p} + M_b \vec{v})^2}{2M_b} \right)$. Neglecting terms of order $1/M_b$, $\delta\epsilon =$

$\delta\epsilon' = \frac{1}{2} (\epsilon_{k-mav/\hbar} - \epsilon_{p-mav/\hbar})$. The resulting second order contribution is

$$\frac{1}{3} \sum_m n_{k\alpha m}^{(2)}(t) = -\frac{g_s^2 \frac{S(S+1)}{2} + 2g_n^2}{V(2\pi)^3} \int d^3\vec{p} (f_k - f_p) \frac{\sin^2 t \delta\epsilon / \hbar}{\delta\epsilon^2}. \quad (\text{C.13})$$

Since the bosons are much heavier than the fermions, they have nearly the same velocity \vec{v} before and after scattering. Therefore, it is easier to work in the bosons' rest frame. For small \vec{v} ,

$$\begin{aligned} \frac{1}{3} \sum_m n_{k+\frac{mav}{\hbar}, \alpha m}^{(2)}(t) &= -\frac{g_s^2 \frac{S(S+1)}{2} + 2g_n^2}{V(2\pi)^3} \int d^3\vec{p} \left(f_k - f_p + \hbar\vec{k} \cdot \vec{v} \frac{\partial f_k}{\partial \epsilon_k} - \hbar\vec{p} \cdot \vec{v} \frac{\partial f_p}{\partial \epsilon_p} \right) \\ &\quad \times \frac{\sin^2(t(\epsilon_k - \epsilon_p)/2\hbar)}{((\epsilon_k - \epsilon_p)/2)^2} + O(v^2, 1/M_b) \end{aligned} \quad (\text{C.14})$$

where $O(v^2, 1/M_b)$ refers to terms which scale as v^2 or $1/M_b$. The first two terms in Eq. (C.14) have negligible contribution near $\epsilon_k = \epsilon_p$. At long times, any significant

contribution comes from the tail of $\frac{\sin^2(t(\epsilon_k - \epsilon_p)/2\hbar)}{((\epsilon_k - \epsilon_p)/2)^2}$, where $\sin^2(t(\epsilon_k - \epsilon_p)/2\hbar)$ can be approximated by its average, $1/2$. Hence their contribution saturates to a constant at long times. For the last two terms in Eq. (C.14), which are significant near $\epsilon_k = \epsilon_p$, we approximate $\frac{\sin^2(t(\epsilon_k - \epsilon_p)/2\hbar)}{((\epsilon_k - \epsilon_p)/2)^2} \simeq \frac{2t\delta(\epsilon_k - \epsilon_p)}{\hbar}$. Hence at long times,

$$\begin{aligned} \frac{1}{3} \sum_m n_{k+\frac{m\mathbf{a}v}{\hbar}, \alpha m}^{(2)}(t) &= -\frac{2(g_s^2 \frac{S(S+1)}{2} + 2g_n^2)t}{V(2\pi)^3} \int d^3\vec{p} \left(\vec{k} \cdot \vec{v} \frac{\partial f_k}{\partial \epsilon_k} - \vec{p} \cdot \vec{v} \frac{\partial f_p}{\partial \epsilon_p} \right) \delta(\epsilon_k - \epsilon_p) \\ &\quad + O\left(t^0, v^2, \frac{1}{M_b}\right) \\ &= -4 \frac{g_s^2 \frac{S(S+1)}{4} + g_n^2}{V^2} t \vec{k} \cdot \vec{v} \frac{\partial f_k}{\partial \epsilon_k} \rho(\epsilon_k) + O\left(t^0, v^2, \frac{1}{M_b}\right), \end{aligned} \quad (\text{C.15})$$

where $\rho(\epsilon_k)$ is the three-dimensional density of states for a single spin projection.

In the laboratory frame,

$$\frac{1}{3} \sum_m n_{k\alpha m}^{(2)}(t) = -4 \frac{g_s^2 \frac{S(S+1)}{4} + g_n^2}{V^2} t \vec{k} \cdot \vec{v} \frac{\partial f_k}{\partial \epsilon_k} \rho(\epsilon_k) + O\left(t^0, v^2, \frac{1}{M_b}\right). \quad (\text{C.16})$$

Third order

The third order term

$$n_{k\alpha m}^{(3)}(t) = \frac{i}{6} \int d\tau_1 d\tau_2 d\tau_3 \langle T \hat{H}_{\text{int}}(\tau_1) \hat{H}_{\text{int}}(\tau_2) \hat{H}_{\text{int}}(\tau_3) \hat{b}_{M_b v, m}(0) \hat{a}_{k\alpha}^\dagger(t) \hat{a}_{k\alpha}(t) \hat{b}_{M_b v, m}^\dagger(0) \rangle_0 \quad (\text{C.17})$$

can be contracted into Wick pairs in 576 ways. However due to reasons explained in earlier sections, all diagrams except the ones shown in Fig. C.7 are zero. After a treatment similar to the one at second order, we calculate the third order contribution to be

$$\begin{aligned} \frac{1}{3} \sum_m n_{k\alpha m}^{(3)}(t) &= \frac{1}{V^2(2\pi)^3} \int d^3\vec{p} t \vec{v} \cdot \vec{k} \rho(\epsilon_k) \frac{\partial f_k}{\partial \epsilon_k} \frac{1}{\epsilon_k - \epsilon_p} \left(f_p g_s^3 S(S+1) - g_s^3 \frac{S(S+1)}{2} \right. \\ &\quad \left. - 3g_s^2 g_n S(S+1) - 4g_n^3 \right) + O\left(t^0, v^2, \frac{1}{M_b}\right). \end{aligned} \quad (\text{C.18})$$

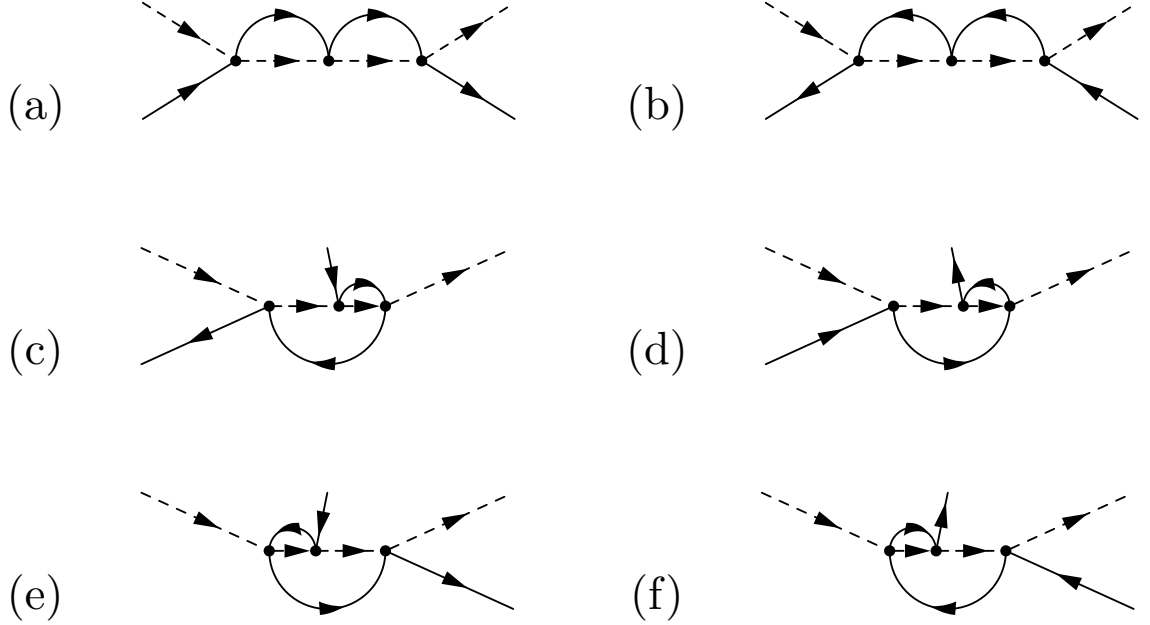


Figure C.7: Non-zero diagrams at $O(g^3)$ in the expansion for $n_{k\alpha m}(t)$.

The right hand side of Eq. (C.18) consists of an ultraviolet divergent term arising from $\int d^3\vec{p} \frac{1}{\epsilon_k - \epsilon_p}$, and a finite term $\int d^3\vec{p} \frac{f_p}{\epsilon_k - \epsilon_p}$ which will ultimately give rise to a logarithmic temperature dependence. The ultraviolet divergence is an artefact of choosing a contact potential between the fermions and bosons which is nonzero only when they are at the same location in space. In reality, the interaction between the fermions and bosons has a finite range, which removes the ultraviolet divergence by introducing an upper cutoff on the limits on the integral over momenta. The exact details are unimportant if we express our results in terms of physical quantities.

To this effect, we define effective coupling constants \tilde{g}_s and \tilde{g}_n where

$$\begin{aligned} \tilde{g}_s^2 &= g_s^2 \left(1 + \frac{g_s + 6g_n}{2(2\pi)^3} \int d^3\vec{p} \frac{1}{\epsilon_k - \epsilon_p} \right), \\ \tilde{g}_n^2 &= g_n^2 \left(1 + \frac{g_n}{(2\pi)^3} \int d^3\vec{p} \frac{1}{\epsilon_k - \epsilon_p} \right). \end{aligned} \quad (\text{C.19})$$

The result for $n_{k\alpha m}(t)$ has no ultraviolet divergences when expressed in terms of \tilde{g}_s and \tilde{g}_n .

The resulting $n_{k\alpha m}(t)$ at long times is

$$\begin{aligned} \frac{1}{3} \sum_m n_{k\alpha m}(t) = & f_k - \frac{4t\vec{k} \cdot \vec{v}\rho(\epsilon_k)}{V^2} \frac{\partial f_k}{\partial \epsilon_k} \\ & \times \left(\frac{S(S+1)}{4} \tilde{g}_s^2 + \tilde{g}_n^2 - \frac{\tilde{g}_s^3 S(S+1)}{4(2\pi)^3} \int d^3\vec{p} \frac{f_p}{\epsilon_k - \epsilon_p} \right). \end{aligned} \quad (\text{C.20})$$

C.1.3 Final momentum of the Fermi gas

The total momentum \vec{P} of the Fermi gas [defined in Eq. (4.12)] will be along the direction of \vec{v} . Its magnitude is

$$\begin{aligned} |\vec{P}| = \frac{\vec{v} \cdot \vec{P}}{v} = & -\frac{8t\hbar N_b}{vV(2\pi)^3} \int d^3\vec{k} (\vec{k} \cdot \vec{v})^2 \frac{\partial f_k}{\partial \epsilon_k} \rho(\epsilon_k) \\ & \times \left(\frac{S(S+1)}{4} \tilde{g}_s^2 + \tilde{g}_n^2 - \frac{\tilde{g}_s^3 S(S+1)}{4(2\pi)^3} \int d^3\vec{p} \frac{f_p}{\epsilon_k - \epsilon_p} \right). \end{aligned} \quad (\text{C.21})$$

After integrating out the angular co-ordinates of \vec{k} and \vec{p} and performing a change of variables,

$$\begin{aligned} |\vec{P}| = & -\frac{16m_a L N_b}{3\hbar V^2} \int d\epsilon \epsilon \frac{\partial f(\epsilon)}{\partial \epsilon} \rho^2(\epsilon) \\ & \times \left(\frac{S(S+1)}{4} \tilde{g}_s^2 + \tilde{g}_n^2 - \frac{\tilde{g}_s^3 S(S+1)}{4V} \int d\epsilon_p \frac{\rho(\epsilon_p) f(\epsilon_p)}{\epsilon - \epsilon_p} \right). \end{aligned} \quad (\text{C.22})$$

We evaluate the second order terms using a Sommerfeld expansion,

$$|\vec{P}_2| \simeq \frac{3m_a L N_b}{4\hbar \epsilon_F} J^2 S(S+1)(1 + \alpha^2) \left(1 + \frac{\pi^2}{6} \left(\frac{k_B T}{\epsilon_F} \right)^2 \right) + O \left(\frac{k_B T}{\epsilon_F} \right)^4. \quad (\text{C.23})$$

where $J = \tilde{g}_s \frac{N}{V}$ and $\alpha = \frac{\tilde{g}_n}{\tilde{g}_s} \frac{2}{\sqrt{S(S+1)}}$.

The third order terms are

$$\begin{aligned} |\vec{P}_3| = & \frac{4S(S+1)m_a L N_b}{3\hbar} \left(\frac{\tilde{g}_s}{V} \right)^3 \int d\epsilon \epsilon \frac{\partial f(\epsilon)}{\partial \epsilon} \rho^2(\epsilon) \times \int d\epsilon_p \frac{\rho(\epsilon_p) f(\epsilon_p)}{\epsilon - \epsilon_p} \\ = & -\frac{9S(S+1)m_a L N_b}{16\hbar \epsilon_F^{9/2}} J^3 \int_0^\infty d\epsilon \epsilon^2 \frac{\partial f(\epsilon)}{\partial \epsilon} \int_0^\infty d\epsilon_p \sqrt{\epsilon_p} \frac{f(\epsilon_p)}{\epsilon - \epsilon_p}. \end{aligned} \quad (\text{C.24})$$

We simplify the above expression by performing integration by parts,

$$\begin{aligned}
|\vec{P}_3| &= \frac{9S(S+1)m_aLN_b}{8\hbar\epsilon_F^{9/2}} J^3 \int_0^\infty d\epsilon \epsilon^2 \frac{\partial f(\epsilon)}{\partial \epsilon} \times \int_0^\infty d\epsilon_p f(\epsilon_p) \\
&\quad \times \frac{\partial}{\partial \epsilon_p} \left(\sqrt{\epsilon_p} + \frac{\sqrt{\epsilon}}{2} \log \left| \frac{\sqrt{\epsilon} - \sqrt{\epsilon_p}}{\sqrt{\epsilon} + \sqrt{\epsilon_p}} \right| \right) \\
&= - \frac{9S(S+1)m_aLN_b}{8\hbar\epsilon_F^{9/2}} J^3 \int_0^\infty d\epsilon \epsilon^2 \frac{\partial f(\epsilon)}{\partial \epsilon} \times \int_0^\infty d\epsilon_p \frac{\partial f(\epsilon_p)}{\partial \epsilon_p} \\
&\quad \times \left(\sqrt{\epsilon_p} + \frac{\sqrt{\epsilon}}{2} \log \left| \frac{\beta(\epsilon - \epsilon_p)}{\beta(\sqrt{\epsilon} + \sqrt{\epsilon_p})^2} \right| \right).
\end{aligned} \tag{C.25}$$

We split Eq. (C.25) into two terms. We evaluate one of these terms numerically,

$$\int_0^\infty d\epsilon \epsilon^{5/2} \frac{\partial f(\epsilon)}{\partial \epsilon} \int_0^\infty d\epsilon_p \frac{\partial f(\epsilon_p)}{\partial \epsilon_p} \log(\beta(\epsilon - \epsilon_p)) \simeq \epsilon_F^{5/2} \left(0.26 + 5.2 \left(\frac{k_B T}{\epsilon_F} \right)^2 \right) + O \left(\frac{k_B T}{\epsilon_F} \right)^4. \tag{C.26}$$

We use a Sommerfeld expansion for the remaining term. The result is

$$\begin{aligned}
|\vec{P}_3| &\simeq - \frac{9S(S+1)m_aLN_b}{8\hbar\epsilon_F^2} J^3 \left(1.13 + \left(2.6 - \frac{\pi^2}{48} \right) \left(\frac{k_B T}{\epsilon_F} \right)^2 \right. \\
&\quad \left. + \frac{1}{2} \log \frac{k_B T}{4\epsilon_F} \left(1 + \frac{5\pi^2}{12} \left(\frac{k_B T}{\epsilon_F} \right)^2 \right) \right) + O \left(\frac{k_B T}{\epsilon_F} \right)^4.
\end{aligned} \tag{C.27}$$

The final momentum of the Fermi gas is

$$\begin{aligned}
\vec{P} &= P_0 \hat{v} \left(1 + \frac{\pi^2}{6} \left(\frac{k_B T}{\epsilon_F} \right)^2 - \frac{3J}{2(1+\alpha^2)\epsilon_F} \left(1.13 + \left(2.6 - \frac{\pi^2}{48} \right) \left(\frac{k_B T}{\epsilon_F} \right)^2 \right. \right. \\
&\quad \left. \left. + \frac{1}{2} \log \frac{k_B T}{4\epsilon_F} \left(1 + \frac{5\pi^2}{12} \left(\frac{k_B T}{\epsilon_F} \right)^2 \right) \right) \right),
\end{aligned} \tag{C.28}$$

where $P_0 = \frac{3S(S+1)N_b}{8}(1+\alpha)^2 \left(\frac{J}{\epsilon_F} \right)^2 (k_F L) \hbar k_F$, and as before, we neglect terms of $O \left(t^0, v^2, \frac{1}{M_b}, T^4 \right)$.

APPENDIX D

DERIVING A QUANTUM DIMER MODEL FOR MOTT INSULATING BOSONIC ATOMS WITH A LARGE HYPERFINE SPIN

D.1 Construction of an orthogonal basis

Here we construct an orthogonal basis from the non-orthogonal singlet coverings, perturbatively in $(2f + 1)^{-1}$. The singlet coverings contain both short and long singlet bonds. We use the commutation relation

$$[\hat{A}_{ij}, \hat{A}_{i'j'}^\dagger] = \delta_{jj'} \left(1 + \frac{\hat{n}_i + \hat{n}_j}{2f + 1} \right) + \frac{1 - \delta_{jj'}}{2f + 1} \sum_m \hat{b}_{jm} \hat{b}_{j',-m}^\dagger,$$

to calculate the overlap between states. We find that the overlap $S_{ab} = \langle a|b\rangle$ between two singlet coverings $|a\rangle$ and $|b\rangle$ is

$$S_{ab} = (2f + 1)^{N_{\text{loops}}} \left(\frac{1}{\sqrt{2f + 1}} \right)^{L_{\text{loops}}}, \quad (\text{D.1})$$

where N_{loops} is the total number of loops which include dimers not in common between $|a\rangle$ and $|b\rangle$, and L_{loops} is the total number of sites in all loops. The overlap matrix element is pictorially represented by a transition graph, shown in Fig. D.1. For large f , we expand S_{ab} in powers of $(2f + 1)^{-1}$:

$$S_{ab} = \delta_{ab} + \frac{\square_{ab}}{2f + 1} + \frac{\square_{ab}^{(2)}}{(2f + 1)^2}. \quad (\text{D.2})$$

Here, $\square_{ab} = 1$ if $|a\rangle$ and $|b\rangle$ have different dimers in one loop with four sites, and 0 otherwise. The symbol $\square_{ab}^{(2)} = 1$ if the dimers in $|a\rangle$ and $|b\rangle$ differ in two loops of four sites each, or in one loop with six sites. The expression for the orthogonal dimer states [Eq. (5.5)] reduces to

$$|\bar{a}\rangle = |a\rangle - \sum_b \left(\frac{\square_{ab}}{2(2f + 1)} + \frac{\square_{ab}^{(2)}}{2(2f + 1)^2} - \frac{3}{8(2f + 1)^2} \sum_c \square_{ac} \square_{cb} \right) |b\rangle + \mathcal{O}(f^{-3}). \quad (\text{D.3})$$

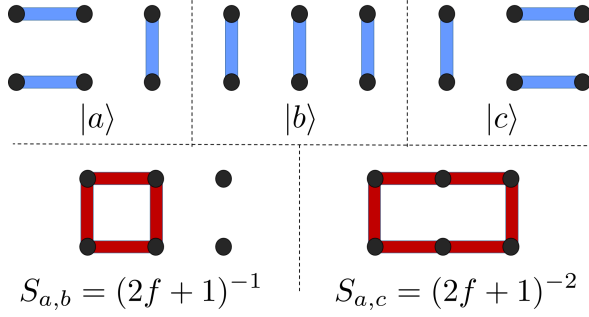


Figure D.1: (Color online) Examples of transition graphs between non-orthogonal singlet coverings. The magnitude of the overlap is given by Eq. (D.1). The overlap S_{ab} comes from 1 loop of length 4 (since it involves 4 sites), and represents the largest possible overlap. The overlap S_{ac} comes from 1 loop of length 6 (since it involves 6 sites). In the large- f limit all singlet coverings become orthogonal.

Figure D.2: (Color online) Pictorial representation of an orthogonal dimer state constructed from non-orthogonal singlet coverings, expressed in Eq. (5.5). A dimer state $|\bar{a}\rangle$ and its associated singlet covering $|a\rangle$ differ by $\mathcal{O}(f^{-1})$ contribution from all coverings $|b\rangle$ which differ from $|a\rangle$ by two bonds in a flippable plaquette.

One example of the calculation of a dimer state is pictorially represented in Fig. D.2.

D.2 Deriving an effective dimer model

The Hamiltonian [Eq. (5.3)] contains terms $\hat{A}_{ij}^\dagger \hat{A}_{ij}$ restricted to nearest neighbor pairs $\langle ij \rangle$ only. The action of one of these terms, $\hat{A}_{ij}^\dagger \hat{A}_{ij}$, on a singlet covering $|a\rangle$ is:

$$\hat{A}_{ij}^\dagger \hat{A}_{ij} |a\rangle = \begin{cases} |a\rangle, & \text{for } (i, j) \in a \\ (2f + 1)^{-1} |(i, j) : a\rangle, & \text{for } (i, j) \notin a \end{cases} \quad (\text{D.4})$$

where the notation $|(i, j) : a\rangle$ denotes a state where sites i and j are paired in a singlet, the original partners of i and j in $|a\rangle$ are paired in another singlet, and all the other bonds in $|a\rangle$ are left unchanged. An example of a singlet covering $|a\rangle$ and a few of the related states $|(i, j) : a\rangle$ are illustrated in Fig. 5.1 in the main text.

To derive an effective model in the Hilbert space spanned by dimer states, we first trivially rewrite the Hamiltonian in Eq. (5.3) as

$$\frac{\hat{H}}{2J^2/U_0} = -\hat{N}_{\text{nn}} - \left(\sum_{\langle ij \rangle} \hat{A}_{ij}^{00\dagger} \hat{A}_{ij}^{00} - \hat{N}_{\text{nn}} \right) \quad (\text{D.5})$$

where \hat{N}_{nn} counts the number of dimers which connect nearest neighbor sites. The first term, $-\hat{N}_{\text{nn}}$, is diagonal in the dimer basis. The low energy eigenspace of $-\hat{N}_{\text{nn}}$ is spanned by the set of all nearest neighbor-only singlet coverings, which have a degenerate eigenvalue $-N/2$, where N is the number of sites. The low energy eigenspace of $-\hat{N}_{\text{nn}}$ is separated from higher energy subspaces by at least $2J^2/U_0$. The second term in Eq. (D.5), $\hat{V}_I = - \left(\sum_{\langle ij \rangle} \hat{A}_{ij}^{00\dagger} \hat{A}_{ij}^{00} - \hat{N}_{\text{nn}} \right)$, is a perturbing term, with matrix elements of $\mathcal{O} \left(\frac{1}{2f+1} \right)$. We use degenerate second order perturbation theory in $(2f+1)^{-1}$ to expand \hat{V}_I in the subspace of nearest-neighbor only dimer coverings:

$$\hat{V}_{\text{eff}} = \sum_{ab} |\bar{a}\rangle \langle \bar{b}| \left(\langle \bar{a} | \hat{V}_I | \bar{b} \rangle + \sum_f \left\langle \bar{a} \left| \hat{V}_I \frac{1}{\hat{N}_{\text{nn}} - N/2} \right| \bar{f} \right\rangle \langle \bar{f} | \hat{V}_I | \bar{b} \rangle \right). \quad (\text{D.6})$$

Here, $|\bar{a}\rangle$ and $|\bar{b}\rangle$ lie in the nearest-neighbor only space, and $|\bar{f}\rangle$ lie in the higher energy subspace. The matrix element for \hat{V}_I between any two dimer states $|\bar{a}\rangle$ and $|\bar{b}\rangle$ is given by

$$\langle \bar{a} | \hat{V}_I | \bar{b} \rangle = N_b \delta_{ab} - \sum_{cd} \left(\sqrt{S^{-1}} \right)_{ac} \left(N_d S_{cd} + \frac{1}{2f+1} \sum_{\langle ij \rangle \notin d} S_{c,(ij):d} \right) \left(\sqrt{S^{-1}} \right)_{db}. \quad (\text{D.7})$$

Substituting Eqs. (D.2) and (D.7) in Eq. (D.6), we find that

$$\hat{V}_{\text{eff}} = \sum_{ab} |\bar{a}\rangle \langle \bar{b}| \left(\frac{-2}{2f+1} \square_{ab} - \sum_f \sum_{\langle ij \rangle \notin f} \sum_{\langle i'j' \rangle \notin b} \delta_{a,(ij):f} \delta_{f,(i'j'):b} \right). \quad (\text{D.8})$$

The result of this expression depends on the lattice geometry. Here we focus on a square lattice. The perturbing term \hat{V}_{eff} can be reduced to a simple form on other lattices as well. On a square lattice, we find that

$$\hat{V}_{\text{eff}} = \sum_{ab} |\bar{a}\rangle \langle \bar{b}| \left(\frac{-2}{2f+1} \square_{ab} - \frac{1}{(2f+1)^2} (4\square\square_{ab} + 2\delta_{ab} (N_{_ _} + N_{_ |} + N_{_ |})) \right). \quad (\text{D.9})$$

Here, $\square\square_{ab}$ is 1 if $|a\rangle$ and $|b\rangle$ differ by three bonds within one six-site plaquette. $N_{_ _}$ counts the number of parallel bonds lying side by side in $|a\rangle$. $N_{_ |}$ and $N_{_ |}$ have similar meanings. Observing that

$$N_{_ _} + N_{_ |} + N_{_ |} + 2N_{=} + 2N_{||} = 3N/2,$$

where N is the number of sites, we rewrite Eq. (D.9) as

$$\hat{V}_{\text{eff}} = \sum_{ab} |\bar{a}\rangle \langle \bar{b}| \left(-\frac{2}{2f+1} \square_{ab} - \frac{4}{(2f+1)^2} \square\square_{ab} + \frac{4\delta_{ab}}{(2f+1)^2} (N_{=} + N_{||}) - \frac{9N/2}{(2f+1)^2} \right). \quad (\text{D.10})$$

The first term—containing \square_{ab} —gives the two-bond resonance term with an amplitude $t = \frac{2}{2f+1} \frac{2J^2}{U_0}$ in \hat{H}_{QDM} [Eq. (5.6)]. The second term—containing $\square\square_{ab}$ —gives the three-bond resonance term with an amplitude $t' = \frac{4}{(2f+1)^2} \frac{2J^2}{U_0}$ in \hat{H}_{QDM} [Eq. (5.6)]. The third term—containing $N_{=} + N_{||}$ —gives an effective interaction $V = \frac{4}{(2f+1)^2} \frac{2J^2}{U_0}$ between two parallel bonds in a four-site plaquette in \hat{H}_{QDM} [Eq. (5.6)]. The last term is a constant energy shift, which is irrelevant.

In summary, the effective dimer model for our system on a square lattice is

$$\hat{H}_{\text{QDM}} = \sum \frac{-4J^2/U_0}{2f+1} (|=\rangle \langle ||| + \text{H.c.}) - \frac{8J^2/U_0}{(2f+1)^2} (|=\rangle \langle =| + ||\rangle \langle ||) - \frac{8J^2/U_0}{(2f+1)^2} (| |=\rangle \langle | |= + \text{H.c.}). \quad (\text{D.11})$$

A similar calculation on other lattice geometries yields a similar effective model, where the amplitudes of the various terms in the model are given in Table 5.1 in the main text.

BIBLIOGRAPHY

- [1] Ian Affleck. The kondo screening cloud. In *Strongly Correlated Fermions and Bosons in Low-Dimensional Disordered Systems*, pages 1–12. Springer, New York, 2002.
- [2] Ian Affleck. The kondo screening cloud: what it is and how to observe it. *arXiv:0911.2209*, 2009.
- [3] P W Anderson. The resonating valence bond state in La_2CuO_4 and superconductivity. *Science*, 235(4793):1196–1198, 1987.
- [4] PW Anderson. Antiferromagnetism. theory of superexchange interaction. *Phys. Rev.*, 79(2):350, 1950.
- [5] N Andrei. Diagonalization of the kondo hamiltonian. *Phys. Rev. Lett.*, 45(5):379, 1980.
- [6] N Andrei, K Furuya, and JH Lowenstein. Solution of the kondo problem. *Rev. Mod. Phys.*, 55(2):331, 1983.
- [7] E Arimondo, M Inguscio, and P Violino. Experimental determinations of the hyperfine structure in the alkali atoms. *Rev. Mod. Phys.*, 49(1):31, 1977.
- [8] Lauren M Aycock, HM Hurst, D Genkina, H-I Lu, V Galitski, and Ian B Spielman. Impurity driven brownian motion of solitons in elongated bose-einstein condensates. *arXiv:1608.03916*, 2016.
- [9] Waseem S Bakr, Jonathon I Gillen, Amy Peng, Simon Fölling, and Markus Greiner. A quantum gas microscope for detecting single atoms in a hubbard-regime optical lattice. *Nature*, 462(7269):74–77, 2009.

- [10] D Banerjee, M Bögli, CP Hofmann, F-J Jiang, P Widmer, and U-J Wiese. Interfaces, strings, and a soft mode in the square lattice quantum dimer model. *Phys. Rev. B*, 90(24):245143, 2014.
- [11] M. A. Baranov, M. Dalmonte, G. Pupillo, and Peter Zoller. Condensed matter theory of dipolar quantum gases. *Chem. Rev.*, 112(9):5012–5061, 2012.
- [12] Ryan Barnett, Anatoli Polkovnikov, and Mukund Vengalattore. Prethermalization in quenched spinor condensates. *Phys. Rev. A*, 84(2):023606, 2011.
- [13] Sourish Basu and Erich J Mueller. Final-state effects in the radio frequency spectrum of strongly interacting fermions. *Phys. Rev. Lett.*, 101(6):060405, 2008.
- [14] Johannes Bauer, Christophe Salomon, and Eugene Demler. Realizing a kondo-correlated state with ultracold atoms. *Phys. Rev. Lett.*, 111(21):215304, 2013.
- [15] James B Boyce and Charles P Slichter. Conduction-electron spin density around fe impurities in cu above and below t_k . *Phys. Rev. Lett.*, 32(2):61, 1974.
- [16] James B Boyce and Charles P Slichter. Conduction-electron spin density around fe impurities in cu above and below the kondo temperature. *Phys. Rev. B*, 13(1):379, 1976.
- [17] Yu A Bychkov and EI Rashba. Properties of a 2d electron gas with lifted spectral degeneracy. *JETP lett*, 39(2):78, 1984.
- [18] Y. H. Chan and L. M. Duan. Evidence of a spin liquid with hard-core bosons in a square lattice. *New J. Phys.*, 14, 2012.

- [19] Darrick E Chang, J Ignacio Cirac, and H Jeff Kimble. Self-organization of atoms along a nanophotonic waveguide. *Phys. Rev. Lett.*, 110(11):113606, 2013.
- [20] David Chen, Matthew White, Cecilia Borries, and Brian DeMarco. Quantum quench of an atomic mott insulator. *Phys. Rev. Lett.*, 106(23):235304, 2011.
- [21] Shu Chen, Congjun Wu, Shou Cheng Zhang, and Yupeng Wang. Exact spontaneous plaquette ground states for high-spin ladder models. *Phys. Rev. B.*, 72(21):3–6, 2005.
- [22] Yu Chen, Zhenhua Yu, and Hui Zhai. Quantum phase transitions of the bose-hubbard model inside a cavity. *Phys. Rev. A*, 93:041601, 2016.
- [23] Marc Cheneau, Peter Barmettler, Dario Poletti, Manuel Endres, Peter Schauß, Takeshi Fukuhara, Christian Gross, Immanuel Bloch, Corinna Kollath, and Stefan Kuhr. Light-cone-like spreading of correlations in a quantum many-body system. *Nature*, 481(7382):484–487, 2012.
- [24] Laurence W. Cheuk, A. T. Sommer, Zoran Hadzibabic, T. Yefsah, Waseem S. Bakr, and Martin W. Zwierlein. Spin-injection spectroscopy of a spin-orbit coupled fermi gas. *Phys. Rev. Lett.*, 109:095302, 2012.
- [25] Lawrence W Cheuk, Matthew A Nichols, Melih Okan, Thomas Gersdorf, Vinay V Ramasesh, Waseem S Bakr, Thomas Lompe, and Martin W Zwierlein. Quantum-gas microscope for fermionic atoms. *Phys. Rev. Lett.*, 114(19):193001, 2015.
- [26] Cheng Chin, Rudolf Grimm, Paul Julienne, and Eite Tiesinga. Feshbach resonances in ultracold gases. *Rev. Mod. Phys.*, 82(2):1225, 2010.

- [27] Sayan Choudhury and Erich J Mueller. Stability of a floquet bose-einstein condensate in a one-dimensional optical lattice. *Phys. Rev. A*, 90(1):013621, 2014.
- [28] Logan W Clark, Li-Chung Ha, Chen-Yu Xu, and Cheng Chin. Quantum dynamics with spatiotemporal control of interactions in a stable bose-einstein condensate. *Phys. Rev. Lett.*, 115(15):155301, 2015.
- [29] E. A. Cornell and C. E. Wieman. Nobel lecture: Bose-einstein condensation in a dilute gas, the first 70 years and some recent experiments. *Rev. Mod. Phys.*, 74:875–893, 2002.
- [30] Sara M Cronenwett, Tjerk H Oosterkamp, and Leo P Kouwenhoven. A tunable kondo effect in quantum dots. *Science*, 281(5376):540–544, 1998.
- [31] Pierre-Gilles De Gennes. *Superconductivity of metals and alloys (advanced book classics)*. Perseus Books Group, 1999.
- [32] Sangita De Sarkar, Rajdeep Sensarma, and K Sengupta. A perturbative renormalization group approach to driven quantum systems. *J. Phys: Cond. Mat*, 26(32):325602, 2014.
- [33] Eugene Demler and Fei Zhou. Spinor bosonic atoms in optical lattices: symmetry breaking and fractionalization. *Phys. Rev. Lett.*, 88(16):163001, 2002.
- [34] JM Deutsch. Quantum statistical mechanics in a closed system. *Phys. Rev. A*, 43(4):2046, 1991.
- [35] Sebastian Diehl, Andrea Tomadin, Andrea Micheli, Rosario Fazio, and Peter Zoller. Dynamical phase transitions and instabilities in open atomic many-body systems. *Phys. Rev. Lett.*, 105(1):015702, 2010.

- [36] Nishant Dogra, Ferdinand Brennecke, Sebastian D Huber, and Tobias Donner. Phase transitions in a bose-hubbard model with cavity-mediated global-range interactions. *Phys. Rev. A*, 94:023632, 2016.
- [37] G Dresselhaus. Spin-orbit coupling effects in zinc blende structures. *Phys. Rev.*, 100(2):580, 1955.
- [38] Sourav Dutta, Daniel S. Elliott, and Yong P. Chen. Formation of ultracold lrb molecules by photoassociation near the li (2s 2s $_{1/2}$) + rb (5p 2p $_{1/2}$) asymptote. *Europhys. Lett.*, 104(6):63001, 2013.
- [39] Sourav Dutta, John Lorenz, Adeel Altaf, Daniel S. Elliott, and Yong P. Chen. Photoassociation of ultracold lrb* molecules: Observation of high efficiency and unitarity-limited rate saturation. *Phys. Rev. A*, 89(2):020702, 2014.
- [40] Luca DAlessio and Anatoli Polkovnikov. Many-body energy localization transition in periodically driven systems. *Ann. Phys.*, 333:19–33, 2013.
- [41] Luca DAlessio and Marcos Rigol. Long-time behavior of isolated periodically driven interacting lattice systems. *Phys. Rev. X*, 4(4):041048, 2014.
- [42] K. Eckert, Zawitkowski, M. J. Leskinen, A. Sanpera, and M. Lewenstein. Ultracold atomic Bose and Fermi spinor gases in optical lattices. *New J. Phys.*, 9, 2007.
- [43] Jens Eisert, Mathis Friesdorf, and Christian Gogolin. Quantum many-body systems out of equilibrium. *Nat. Phys.*, 11(2):124–130, 2015.
- [44] P O Fedichev, Yu Kagan, G V Shlyapnikov, and J T M Walraven. Influence of nearly resonant light on the scattering length in low-temperature atomic gases. *Phys. Rev. Lett.*, 77(14):2913, 1996.

- [45] Hong-Bing Fei, Bradley M Jost, Sandu Popescu, Bahaa EA Saleh, and Malvin C Teich. Entanglement-induced two-photon transparency. *Phys. Rev. Lett.*, 78(9):1679, 1997.
- [46] Alexander L Fetter. Vortices in an imperfect bose gas. i. the condensate. *Phys. Rev.*, 138(2A):A429, 1965.
- [47] Matthew PA Fisher, Peter B Weichman, G Grinstein, and Daniel S Fisher. Boson localization and the superfluid-insulator transition. *Phys. Rev. B*, 40(1):546, 1989.
- [48] Z Fisk, HR Ott, and G Aeppli. Experimental perspectives on heavy-electron metals. *Jap. J. Appl. Phys.*, 26(S3-3):1882, 1987.
- [49] Z Fisk, J. L. Sarrao, J. L. Smith, and J. D. Thompson. The physics and chemistry of heavy fermions. *Proc. Natl. Acad. Sci.*, 92(15):6663–6667, 1995.
- [50] Michael Foss-Feig, Michael Hermele, and Ana Maria Rey. Probing the kondo lattice model with alkaline-earth-metal atoms. *Phys. Rev. A*, 81:051603, 2010.
- [51] Eduardo Fradkin, David A. Huse, R. Moessner, V. Oganesyan, and S. L. Sondhi. Bipartite RokhsarKivelson points and Cantor deconfinement. *Phys. Rev. B*, 69(22):224415, 2004.
- [52] Zhengkun Fu, Lianghai Huang, Zengming Meng, Pengjun Wang, Xia-Ji Liu, Han Pu, Hui Hu, and Jing Zhang. Radio-frequency spectroscopy of a strongly interacting spin-orbit-coupled fermi gas. *Phys. Rev. A*, 87(5):053619, 2013.
- [53] Zhengkun Fu, Pengjun Wang, Lianghai Huang, Zengming Meng, Hui Hu, and Jing Zhang. Optical control of a magnetic feshbach resonance in an ultracold fermi gas. *Phys. Rev. A*, 88(4):041601, 2013.

- [54] Peter Fulde and Richard A Ferrell. Superconductivity in a strong spin-exchange field. *Phys. Rev.*, 135(3A):A550, 1964.
- [55] Alexander L Gaunt, Tobias F Schmidutz, Igor Gotlibovych, Robert P Smith, and Zoran Hadzibabic. Bose-einstein condensation of atoms in a uniform potential. *Phys. Rev. Lett.*, 110(20):200406, 2013.
- [56] Julio Gea-Banacloche. Two-photon absorption of nonclassical light. *Phys. Rev. Lett.*, 62(14):1603, 1989.
- [57] Stephen D Gensemer, Ross B Martin-Wells, Aaron W Bennett, and Kurt Gibble. Direct observation of resonant scattering phase shifts and their energy dependence. *Phys. Rev. Lett.*, 109(26):263201, 2012.
- [58] David Goldhaber-Gordon, Hadas Shtrikman, D Mahalu, David Abusch-Magder, U Meirav, and MA Kastner. Kondo effect in a single-electron transistor. *Nature*, 391(6663):156–159, 1998.
- [59] Sarang Gopalakrishnan, Benjamin L Lev, and Paul M Goldbart. Atom-light crystallization of bose-einstein condensates in multimode cavities: Nonequilibrium classical and quantum phase transitions, emergent lattices, supersolidity, and frustration. *Phys. Rev. A*, 82(4):043612, 2010.
- [60] Michael Gring, Maximilian Kuhnert, Tim Langen, Takuya Kitagawa, Bernhard Rauer, Matthias Schreitl, Igor Mazets, D Adu Smith, Eugene Demler, and Jörg Schmiedmayer. Relaxation and prethermalization in an isolated quantum system. *Science*, 337(6100):1318–1322, 2012.
- [61] Eugene P Gross. Structure of a quantized vortex in boson systems. *Il Nuovo Cimento (1955-1965)*, 20(3):454–477, 1961.

- [62] Michael Hermele, Victor Gurarie, and Ana Maria Rey. Mott insulators of ultracold fermionic alkaline earth atoms: Underconstrained magnetism and chiral spin liquid. *Phys. Rev. Lett.*, 103(13):4–7, 2009.
- [63] Alexander Cyril Hewson. *The Kondo problem to heavy fermions*. Number Vol. 2. Cambridge university press, 1997.
- [64] Lianghai Huang, Zengming Meng, Pengjun Wang, Peng Peng, Shao-Liang Zhang, Liangchao Chen, Donghao Li, Qi Zhou, and Jing Zhang. Experimental realization of two-dimensional synthetic spin-orbit coupling in ultracold fermi gases. *Nat. Phys.*, 12(6):540–544, 2016.
- [65] Robin L Hudson. When is the wigner quasi-probability density non-negative? *Rep. Math. Phys.*, 6(2):249–252, 1974.
- [66] Chen-Lung Hung, Victor Gurarie, and Cheng Chin. From cosmology to cold atoms: observation of sakharov oscillations in a quenched atomic superfluid. *Science*, 341(6151):1213–1215, 2013.
- [67] Adilet Imambekov, Mikhail Lukin, and Eugene Demler. Spin-exchange interactions of spin-one bosons in optical lattices: Singlet, nematic, and dimerized phases. *Phys. Rev. A*, 68(6):063602, 2003.
- [68] L. B. Ioffe, M. V. Feigel'man, A. Ioselevich, D. Ivanov, M. Troyer, and G Blatter. Topologically protected quantum bits using josephson junction arrays. *Nature*, 415(6871):503–506, 2002.
- [69] Dieter Jaksch, Ch Bruder, Juan Ignacio Cirac, Crispin W Gardiner, and Peter Zoller. Cold bosonic atoms in optical lattices. *Phys. Rev. Lett.*, 81(15):3108, 1998.

- [70] Dieter Jaksch and P. Zoller. The cold atom Hubbard toolbox. *Ann. Phys. (N. Y.)*, 315(1):52–79, 2005.
- [71] Juha Javanainen and Phillip L Gould. Linear intensity dependence of a two-photon transition rate. *Phys. Rev. A*, 41(9):5088, 1990.
- [72] L. Jiang, T. Kitagawa, Jason Alicea, A. R. Akhmerov, David Pekker, G. Refael, J. I. Cirac, Eugene Demler, Mikhail D. Lukin, and Peter Zoller. Majorana fermions in equilibrium and in driven cold-atom quantum wires. *Phys. Rev. Lett.*, 106:220402, 2011.
- [73] Gyu-Boong Jo, Jennie Guzman, Claire K Thomas, Pavan Hosur, Ashvin Vishwanath, and Dan M Stamper-Kurn. Ultracold atoms in a tunable optical kagome lattice. *Phys. Rev. Lett.*, 108(4):045305, 2012.
- [74] Kevin M Jones, Eite Tiesinga, Paul D Lett, and Paul S Julienne. Ultracold photoassociation spectroscopy: Long-range molecules and atomic scattering. *Rev. Mod. Phys.*, 78(2):483, 2006.
- [75] Kevin M Jones, Eite Tiesinga, Paul D Lett, and Paul S Julienne. Ultracold photoassociation spectroscopy: Long-range molecules and atomic scattering. *Rev. Mod. Phys.*, 78(2):483, 2006.
- [76] Adam M Kaufman, M Eric Tai, Alexander Lukin, Matthew Rispoli, Robert Schittko, Philipp M Preiss, and Markus Greiner. Quantum thermalization through entanglement in an isolated many-body system. *Science*, 353(6301):794–800, 2016.
- [77] A. Yu Kitaev. Fault-tolerant quantum computation by anyons. *Ann. Phys.*, 303(1):2–30, 2003.

- [78] Alexei Yu Kitaev. Unpaired majorana fermions in quantum wires. *Phys.-Usp.*, 44:131, 2001.
- [79] Steven A. Kivelson, Daniel S. Rokhsar, and James P. Sethna. Topology of the resonating valence-bond state: Solitons and high- T_c superconductivity. *Phys. Rev. B*, 35(16):8865–8868, 1987.
- [80] Jens Klinder, H Keßler, M Reza Bakhtiari, M Thorwart, and A Hemmerich. Observation of a superradiant mott insulator in the dicke-hubbard model. *Phys. Rev. Lett.*, 115(23):230403, 2015.
- [81] Alicia J Kollár, Alexander T Papageorge, Kristian Baumann, Michael A Armen, and Benjamin L Lev. An adjustable-length cavity and bose–einstein condensate apparatus for multimode cavity qed. *New J. Phys.*, 17(4):043012, 2015.
- [82] Alicia J Kollár, Alexander T Papageorge, Varun D Vaidya, Yudan Guo, Jonathan Keeling, and Benjamin L Lev. Supermode-density-wave-polariton condensation. *arXiv:1606.04127*, 2016.
- [83] Jun Kondo. Resistance minimum in dilute magnetic alloys. *Prog. Theor. Phys.*, 32(1):37–49, 1964.
- [84] Christina V. Kraus, S. Diehl, Peter Zoller, and Mikhail A. Baranov. Probing atomic majorana fermions in optical lattices. *New J. Phys.*, 14:113036, 2012.
- [85] Sebastian Krinner, Martin Lebrat, Dominik Husmann, Charles Grenier, Jean-Philippe Brantut, and Tilman Esslinger. Mapping out spin and particle conductances in a quantum point contact. *Proc. Natl. Acad. Sci.*, 113(29):8144–8149, 2016.

- [86] Renate Landig, Lorenz Hruby, Nishant Dogra, Manuele Landini, Rafael Mottl, Tobias Donner, and Tilman Esslinger. Quantum phases from competing short-and long-range interactions in an optical lattice. *Nature (London)*, 532(7600):476–479, 2016.
- [87] AI Larkin and Yu N Ovchinnikov. Nonuniform state of superconductors. *Zh. Eksperim. i Teor. Fiz.*, 47, 1964.
- [88] Achilleas Lazarides, Arnab Das, and Roderich Moessner. Equilibrium states of generic quantum systems subject to periodic driving. *Phys. Rev. E*, 90(1):012110, 2014.
- [89] Achilleas Lazarides, Arnab Das, and Roderich Moessner. Periodic thermodynamics of isolated quantum systems. *Phys. Rev. Lett.*, 112(15):150401, 2014.
- [90] Patrick a. Lee, Naoto Nagaosa, and Xiao Gang Wen. Doping a Mott insulator: Physics of high-temperature superconductivity. *Rev. Mod. Phys.*, 78(January), 2006.
- [91] Julian Léonard, Andrea Morales, Philip Zupancic, Tilman Esslinger, and Tobias Donner. Supersolid formation in a quantum gas breaking continuous translational symmetry. *arXiv:1609.09053*, 2016.
- [92] P. W. Leung, K. C. Chiu, and Karl J. Runge. Columnar dimer and plaquette resonating-valence-bond orders in the quantum dimer model. *Phys. Rev. B*, 54(18):12938–12945, 1996.
- [93] Junru Li, Wujie Huang, Boris Shteynas, Sean Burchesky, Furkan Çağrı Top, Edward Su, Jeongwon Lee, Alan O Jamison, and Wolfgang Ketterle. Spin-

- orbit coupling and spin textures in optical superlattices. *Phys. Rev. Lett.*, 117(18):185301, 2016.
- [94] Yongqiang Li, Liang He, and Walter Hofstetter. Lattice-supersolid phase of strongly correlated bosons in an optical cavity. *Phys. Rev. A*, 87(5):051604, 2013.
- [95] Y. Liao, A. S. C. Rittner, T. Paprotta, W. Li, G. B. Partridge, Randall G. Hulet, Stephan K. Baur, and Erich J. Mueller. Spin-imbalance in a one-dimensional fermi gas. *Nature*, 467:567, 2010.
- [96] Hong Lu, LO Baksmaty, CJ Bolech, and Han Pu. Expansion of 1d polarized superfluids: The fulde-ferrell-larkin-ovchinnikov state reveals itself. *Phys. Rev. Lett.*, 108(22):225302, 2012.
- [97] Dirk-Sören Lühmann, Ole Jürgensen, Malte Weinberg, Juliette Simonet, Parvis Soltan-Panahi, and Klaus Sengstock. Quantum phases in tunable state-dependent hexagonal optical lattices. *Phys. Rev. A*, 90(1):013614, 2014.
- [98] Gerald D Mahan. *Many-particle Physics*. Springer, New York, 2000.
- [99] Christoph Maschler and Helmut Ritsch. Cold atom dynamics in a quantum optical lattice potential. *Phys. Rev. Lett.*, 95:260401, 2005.
- [100] R Mathew, A Kumar, S Eckel, F Jendrzejewski, GK Campbell, Mark Edwards, and E Tiesinga. Self-heterodyne detection of the in situ phase of an atomic superconducting quantum interference device. *Phys. Rev. A*, 92(3):033602, 2015.
- [101] D McKay and B DeMarco. Thermometry with spin-dependent lattices. *New J. Phys.*, 12(5):055013, 2010.

- [102] F Mei, C. J. Shan, X. L. Feng, S. L. Zhu, Z. M. Zhang, L. C. Kwek, D. Wilkowski, and C. H. Oh. Creation, manipulation and detection of majorana fermions with cold atoms in optical lattices. *arXiv:1204.3974*, 2012.
- [103] Florian Meinert, Manfred J Mark, Emil Kirilov, Katharina Lauber, Philipp Weinmann, Andrew J Daley, and H-C Nägerl. Quantum quench in an atomic one-dimensional ising chain. *Phys. Rev. Lett.*, 111(5):053003, 2013.
- [104] Albert Messiah. *Quantum Mechanics Vol. 2*. Dover Books on Physics, 1958.
- [105] Martin Miranda, Ryotaro Inoue, Yuki Okuyama, Akimasa Nakamoto, and Mikio Kozuma. Site-resolved imaging of ytterbium atoms in a two-dimensional optical lattice. *Phys. Rev. A*, 91:063414, 2015.
- [106] G Misguich, D Serban, and V Pasquier. Quantum dimer model on the kagome lattice: Solvable dimer-liquid and ising gauge theory. *Phys. Rev. Lett.*, 89(13):137202, 2002.
- [107] R Moessner and K. S. Raman. Quantum dimer models. *arXiv: 0809.3051*, 2008.
- [108] R. Moessner and S. L. Sondhi. Resonating valence bond phase in the triangular lattice quantum dimer model. *Phys. Rev. Lett.*, 86(9):1881–1884, 2001.
- [109] R Moessner and S L Sondhi. Resonating valence bond liquid physics on the triangular lattice. *Prog. Theor. Phys. Suppl.*, 145(145):37–42, 2002.
- [110] R Moessner, S. L. Sondhi, and P Chandra. Two-dimensional periodic frustrated ising models in a transverse field. *Phys. Rev. Lett.*, 84(19):4457–4460, 2000.

- [111] R Moessner, S L Sondhi, and P Chandra. Phase diagram of the hexagonal lattice quantum dimer model. *Phys. Rev. B*, 64(14):144416, 2001.
- [112] R Moessner, S L Sondhi, and Eduardo Fradkin. Short-ranged resonating valence bond physics, quantum dimer models, and ising gauge theories. *Phys. Rev. B*, 65(2):024504, 2001.
- [113] Henning Moritz, Thilo Stöferle, Michael Köhl, and Tilman Esslinger. Exciting collective oscillations in a trapped 1d gas. *Phys. Rev. Lett.*, 91:250402, 2003.
- [114] V. Mourik, K. Zou, S. M. Frolov, S. R. Plissard, E. P. A. M. Bakers, and Leo P. Kouwenhoven. Signatures of majorana fermions in hybrid superconductor-semiconductor nanowire devices. *Science*, 336:1003, 2012.
- [115] Ashok Muthukrishnan, Girish S Agarwal, and Marlan O Scully. Inducing disallowed two-atom transitions with temporally entangled photons. *Phys. Rev. Lett.*, 93(9):093002, 2004.
- [116] Masaya Nakagawa and Norio Kawakami. Laser-induced kondo effect in ultracold alkaline-earth fermions. *Phys. Rev. Lett.*, 115:165303, 2015.
- [117] Kouki Nakata and Keisuke Totsuka. Extended quantum dimer model and novel valence-bond phases. *J. Stat. Mech.*, 2011(01):01033, 2011.
- [118] Stefan S Natu and Erich J Mueller. Pairing, ferromagnetism, and condensation of a normal spin-1 bose gas. *Phys. Rev. A*, 84(5):053625, 2011.
- [119] Chetan Nayak, Steven H. Simon, Ady Stern, Michael Freedman, and Sankar DasSarma. Non-abelian anyons and topological quantum computation. *Rev. Mod. Phys.*, 80:1083, 2007.

- [120] Jason HV Nguyen, Paul Dyke, De Luo, Boris A Malomed, and Randall G Hulet. Collisions of matter-wave solitons. *Nat. Phys.*, 10(12):918–922, 2014.
- [121] Yusuke Nishida. $Su(3)$ orbital kondo effect with ultracold atoms. *Phys. Rev. Lett.*, 111:135301, 2013.
- [122] Ph Nozières and A Blandin. Kondo effect in real metals. *J. de Phys.*, 41(3):193–211, 1980.
- [123] H Ott, J Fortagh, G Schlotterbeck, A Grossmann, and C Zimmermann. Bose-einstein condensation in a surface microtrap. *Phys. Rev. Lett.*, 87(23):230401, 2001.
- [124] Jaromir Panas, Anna Kauch, and Krzysztof Byczuk. Spectral properties and phase diagram of correlated lattice bosons in an optical cavity within the b-dmft. *arXiv:1607.00671*, 2016.
- [125] Colin V Parker, Li-Chung Ha, and Cheng Chin. Direct observation of effective ferromagnetic domains of cold atoms in a shaken optical lattice. *Nat. Phys.*, 9(12):769–774, 2013.
- [126] Maxwell F Parsons, Florian Huber, Anton Mazurenko, Christie S Chiu, Widagdo Setiawan, Katherine Wooley-Brown, Sebastian Blatt, and Markus Greiner. Site-resolved imaging of fermionic $Li\ 6$ in an optical lattice. *Phys. Rev. Lett.*, 114(21):213002, 2015.
- [127] Maxwell F Parsons, Anton Mazurenko, Christie S Chiu, Geoffrey Ji, Daniel Greif, and Markus Greiner. Site-resolved observations of antiferromagnetic correlations in the hubbard model. *arXiv:1605.02704*, 2016.
- [128] A Polkovnikov, K Sengupta, A Silva, and M Vengalattore. Nonequilibrium

- dynamics of closed interacting quantum systems. *Rev. Mod. Phys.*, 83:863, 2011.
- [129] Anatoli Polkovnikov. Phase space representation of quantum dynamics. *Ann. Phys.*, 325(8):1790–1852, 2010.
- [130] Pedro Ponte, Anushya Chandran, Z Papić, and Dmitry A Abanin. Periodically driven ergodic and many-body localized quantum systems. *Ann. Phys.*, 353:196–204, 2015.
- [131] A. Ralko, D. Poilblanc, and R. Moessner. Generic mixed columnar-plaquette phases in Rokhsar-Kivelson models. *Phys. Rev. Lett.*, 100(3):2–5, 2008.
- [132] Arnaud Ralko, Michel Ferrero, Federico Becca, Dmitri Ivanov, and Frédéric Mila. Zero-temperature properties of the quantum dimer model on the triangular lattice. *Phys. Rev. B.*, 71(22):1–9, 2005.
- [133] Adam Rançon, Chen-Lung Hung, Cheng Chin, and K Levin. Quench dynamics in bose-einstein condensates in the presence of a bath: Theory and experiment. *Phys. Rev. A*, 88(3):031601, 2013.
- [134] Marten Richter and Shaul Mukamel. Collective two-particle resonances induced by photon entanglement. *Phys. Rev. A*, 83(6):063805, 2011.
- [135] NP Robins, C Figl, JD Close, et al. Probing a bose-einstein condensate with an atom laser. *Opt. Exp.*, 16(18):13893–13900, 2008.
- [136] Leonid P. Rokhinson, Z.Liu, and J. K. Furdyna. The fractional ac josephson effect in a semiconductor-superconductor nanowire as a signature of majorana particles. *Nat. Phys.*, 8:795–799, 2012.

- [137] Daniel S. Rokhsar and Steven A. Kivelson. Superconductivity and the quantum hard-core dimer gas. *Phys. Rev. Lett.*, 61(20):2376–2379, 1988.
- [138] Todd C. Rutkowski and Michael J. Lawler. Spin liquid phases of large-spin Mott insulating ultracold bosons. *Phys. Rev. B*, 93(9):094405, 2016.
- [139] Subir Sachdev. Spin-peierls ground states of the quantum dimer model: A finite-size study. *Phys. Rev. B*, 40(7):5204–5207, 1989.
- [140] T. L. Schmidt, L. Nuppenkamp, and Christoph Bruder. Microwave controlled coupling of majorana bound states. *New J. Phys.*, 15:025043, 2012.
- [141] Thomas L Schmidt, Andreas Nuppenkamp, and Christoph Bruder. Majorana qubit rotations in microwave cavities. *Phys. Rev. Lett.*, 110(10):107006, 2013.
- [142] T. Senthil and M. P A Fisher. Fractionalization in the cuprates: detecting the topological order. *Phys. Rev. Lett.*, 86(2):292–295, 2001.
- [143] T. Senthil, Ashvin Vishwanath, Leon Balents, Subir Sachdev, and Matthew P. A. Fisher. Deconfined quantum critical points. *Science*, 303(5663):1490–1494, 2004.
- [144] P. Sinkovicz, A. Zamora, E. Szirmai, M. Lewenstein, and G. Szirmai. Spin liquid phases of alkaline-earth-metal atoms at finite temperature. *Phys. Rev. A*, 88(6):1–14, 2013.
- [145] S.Nascimbène. Realizing one-dimensional topological superfluids with ultracold atomic gases. *J. Phys. B*, 46:134005, 2012.
- [146] Hao Song and Michael Hermele. Mott insulators of ultracold fermionic alkaline earth atoms in three dimensions. *Phys. Rev. B.*, 87(14):1–9, 2013.

- [147] Mark Srednicki. Chaos and quantum thermalization. *Phys. Rev. E*, 50(2):888, 1994.
- [148] Dan M Stamper-Kurn and Masahito Ueda. Spinor bose gases: Symmetries, magnetism, and quantum dynamics. *Rev. Mod. Phys.*, 85(3):1191, 2013.
- [149] Bhuvanesh Sundar and Erich J. Mueller. Proposal to directly observe the kondo effect through enhanced photoinduced scattering of cold fermionic and bosonic atoms. *Phys. Rev. A*, 93:023635, 2016.
- [150] Olav F. Syljuåsen. Plaquette phase of the square-lattice quantum dimer model: Quantum Monte Carlo calculations. *Phys. Rev. B*, 73(24):245105, 2006.
- [151] E Szirmai and M Lewenstein. Exotic magnetic orders for high-spin ultracold fermions. *Europhys. Lett.*, 93(6):66005, 2011.
- [152] Sumanta Tewari, Sankar DasSarma, Chetan Nayak, Chuanwei Zhang, and Peter Zoller. Quantum computation using vortices and majorana zero modes of a $p_x + ip_y$ superfluid of fermionic cold atoms. *Phys. Rev. Lett.*, 98:010506, 2007.
- [153] M Theis, G Thalhammer, K Winkler, M Hellwig, G Ruff, R Grimm, and J Hecker Denschlag. Tuning the scattering length with an optically induced feshbach resonance. *Phys. Rev. Lett.*, 93(12):123001, 2004.
- [154] Nicholas R Thomas, Niels Kjærgaard, Paul S Julienne, and Andrew C Wilson. Imaging of s and d partial-wave interference in quantum scattering of identical bosonic atoms. *Phys. Rev. Lett.*, 93(17):173201, 2004.
- [155] Hirokazu Tsunetsugu, Manfred Sigrist, and Kazuo Ueda. The ground-state

- phase diagram of the one-dimensional kondo lattice model. *Rev. Mod. Phys.*, 69(3):809, 1997.
- [156] Ashvin Vishwanath, L. Balents, and T. Senthil. Quantum criticality and deconfinement in phase transitions between valence bond solids. *Phys. Rev. B.*, 69(22):1–13, 2004.
- [157] Daniel Vorberg, Waltraut Wustmann, Roland Ketzmerick, and André Eckardt. Generalized bose-einstein condensation into multiple states in driven-dissipative systems. *Phys. Rev. Lett.*, 111(24):240405, 2013.
- [158] P. Wang, Z. Q. Yu, Z.Fu, J.Miao, L.Huang, S.Chai, Hui Zhai, and Jing Zhang. Spin-orbit coupled degenerate fermi gases. *Phys. Rev. Lett.*, 109:095301, 2012.
- [159] Ran Wei and Erich J. Mueller. Majorana fermions in one-dimensional spin-orbit coupled fermi gases. *Phys. Rev. A*, 86:063604, 2012.
- [160] X. G. Wen. Mean-field theory of spin-liquid states with finite energy gap and topological orders. *Phys. Rev. B*, 44(6):2664–2672, 1991.
- [161] PB Wiegmann. Exact solution of the sd exchange model (kondo problem). *J. Phys. C*, 14(10):1463, 1981.
- [162] Ross A Williams, Lindsay J LeBlanc, Karina Jimenez-Garcia, Matthew C Beeler, Abigail R Perry, William D Phillips, and Ian B Spielman. Synthetic partial waves in ultracold atomic collisions. *Science*, 335(6066):314–317, 2012.
- [163] Kenneth G Wilson. The renormalization group: Critical phenomena and the kondo problem. *Rev. Mod. Phys.*, 47(4):773, 1975.

- [164] Patrick Windpassinger and Klaus Sengstock. Engineering novel optical lattices. *Rep. Prog. Phys.*, 76(8):086401, 2013.
- [165] Cenke Xu and Congjun Wu. Resonating plaquette phases in SU(4) Heisenberg antiferromagnet. *Phys. Rev. B.*, 77(4):1–7, 2008.
- [166] I Yavin, M Weel, A Andreyuk, and A Kumarakrishnan. A calculation of the time-of-flight distribution of trapped atoms. *Amer. J. Phys.*, 70(2):149–152, 2002.
- [167] Tarik Yefsah, Ariel T Sommer, Mark JH Ku, Lawrence W Cheuk, Wenjie Ji, Waseem S Bakr, and Martin W Zwierlein. Heavy solitons in a fermionic superfluid. *Nature*, 499(7459):426–430, 2013.
- [168] S K Yip. Dimer state of spin-1 bosons in an optical lattice. *Phys. Rev. Lett.*, 90(June):250402, 2003.
- [169] Chen Zeng and Veit Elser. Quantum dimer calculations on the spin-1/2 kagome heisenberg antiferromagnet. *Phys. Rev. B*, 51(13):8318–8324, 1995.
- [170] Chuanwei Zhang, Sumanta Tewari, Roman M Lutchyn, and S Das Sarma. p x+ i p y superfluid from s-wave interactions of fermionic cold atoms. *Phys. Rev. Lett.*, 101(16):160401, 2008.
- [171] Zhan Zheng, Pablo L Saldanha, José R Rios Leite, and Claude Fabre. Two-photon–two-atom excitation by correlated light states. *Phys. Rev. A*, 88(3):033822, 2013.
- [172] Fei Zhou and Gordon W Semenoff. Quantum insulating states of f= 2 cold atoms in optical lattices. *Phys. Rev. Lett.*, 97(18):180411, 2006.

- [173] T. Zhou and Z. D. Wang. Revealing majorana fermion states in a superfluid of cold atoms subject to a harmonic potential. *Phys. Rev. B*, 88(15):155114, 2013.